

High-Pressure Crystallography

Habilitation Thesis

Presented by
Artem R. Oganov

Submitted to the
Department of Materials, ETH Zurich
March 2007

Acknowledgements

This Habilitation thesis presents my work of the last 5 years, mostly done at ETH Zurich and partly at University College London. This was a really exciting time, and I owe a great deal of gratitude to my numerous colleagues and friends.

Prof. G. David Price: For his friendship and inspiring discussions, both scientific and personal. David's style (best described as "light-hearted wisdom") and his incredible speed of thought have greatly affected me.

Prof. Walter Steurer: For supporting and encouraging my (successful) efforts to build a strong independent research group.

Dr. Shigeaki Ono: For being an ideal collaborator – talented, open, hard-working, friendly and extremely interesting person. I remember with pleasure our walks in Meiji-jingu (Tokyo) and Kensington (London).

Profs. Michele Parrinello, Roman Martoňák, Alessandro Laio: For our friendship and a stimulating collaboration on metadynamics. For hospitality during my stays in Lugano.

Prof. Dmitry Y. Pushcharovsky: For our friendship and collaboration.

My dear collaborators Peter I. Dorogokupets, Jiuhua Chen, Yanzhang Ma: For expanding the field of my research interests and attracting me to new challenges.

Colleagues from my research group: Prof. Yanming Ma, Colin W. Glass, Daniel Y. Jung, Donat Adams, Feiwu Zhang, Kai H. Hassdenteufel: For the exciting "electrified" scientific spirit of our group (the spirit of perpetuum mobile), for their friendship and collaboration. I am infinitely grateful to all of them.

Other colleagues: **Prof. Roald Hoffmann**, for exciting discussions on science and other things. **Mario Valle**, for his excellent work in visualisation, and for the personal friendship we have developed over years. I appreciated Mario's visits to Zurich, our lunches and dinners with an enjoyable mixture of personal and professional conversation. **Prof. Rene Monnier and Dr. Penelope Schobinger**, for their friendship. Nelly Schobinger has been my guarding angel in Zurich. **Dr. Agnès Dewaele**, for her friendship and love, as well as exciting scientific discussions.

My family: my mother Galia, my uncle Felix, my brother Arthur. I owe them everything.

Content

Acknowledgements	2
Content	3
Outline of the thesis	6
PART I. INTRODUCTION: New phenomena and open problems in high-pressure crystallography.	9
1. Importance of studies of matter at extreme conditions	9
2. Pressure as a thermodynamic variable	10
3. Experimental methods for research at extreme conditions	13
4. Computational methods for high-pressure research	18
4.1. Modern electronic structure calculations	19
4.2. <i>Ab initio</i> molecular dynamics and quasiharmonic approximation	29
4.3. Crystal structure prediction: evolutionary algorithms and metadynamics	36
5. New phenomena at high pressure	48
5.1. Quantum melting and pressure-induced amorphisation	48
5.2. Breakdown of close packing under pressure	50
5.3. Metallisation and demetallisation	53
5.4. Unusual structures of the elements under pressure	57
5.5. New mineral phases in planetary interiors	61
6. Concluding remarks	69
7. References	71
Appendix I. Curriculum Vitae	82
Appendix II. List of patents and publications	86

PART II. REPRINTS.

- Paper 1.** Oganov A.R., Ono S. (2004). Theoretical and experimental evidence for a post-perovskite phase of MgSiO₃ in Earth's D'' layer. *Nature* **430**, 445-448.
- Paper 2.** Oganov A.R., Martoňák R., Laio A., Raiteri P., Parrinello M. (2005). Anisotropy of Earth's D'' layer and stacking faults in the MgSiO₃ post-perovskite phase. *Nature* **438**, 1142-1144.
- Paper 3.** Oganov A.R., S. Ono (2005). The high-pressure phase of alumina and implications for Earth's D'' layer. *Proc. Natl. Acad. Sci.* **102**, 10828-10831.

- Paper 4.** Ono S., Oganov A.R. (2005). *In situ* observations of phase transition between perovskite and CaIrO₃-type phase in MgSiO₃ and pyrolytic mantle composition. *Earth Planet. Sci. Lett.* **236**, 914-932.
- Paper 5.** Zhang F., Oganov A.R. (2006). Valence and spin states of iron impurities in mantle-forming silicates. *Earth Planet. Sci. Lett.* **249**, 436-443.
- Paper 6.** Jung D.Y., Oganov A.R. (2005). *Ab initio* study of the high-pressure behaviour of CaSiO₃ perovskite. *Phys. Chem. Minerals* **32**, 146-153.
- Paper 7.** Adams D.J., Oganov A.R. (2006). *Ab initio* molecular dynamics study of CaSiO₃ perovskite at P-T conditions of Earth's lower mantle. *Phys. Rev. B* **73**, 184106.
- Paper 8.** Martoňák R., Donadio D., Oganov A.R., Parrinello M. (2006). Crystal structure transformations in SiO₂ from classical and *ab initio* metadynamics. *Nature Materials* **5**, 623-626.
- Paper 9.** Oganov A.R., Gillan M.J., Price G.D. (2003). Ab initio lattice dynamics and structural stability of MgO. *J. Chem. Phys.* **118**, 10174-10182.
- Paper 10.** Oganov A.R., Gillan M.J., Price G.D. (2005). Structural stability of silica at high pressures and temperatures. *Phys. Rev. B* **71**, art. 064104.
- Paper 11.** Oganov A.R., Price G.D. (2005). *Ab initio* thermodynamics of MgSiO₃ perovskite at high pressures and temperatures. *J. Chem. Phys.* **122**, art. 124501.
- Paper 12.** Ghose S., Krisch M., Oganov A.R., Beraud A., Bossak A., Gulve R., Seelaboyina R., Yang H., Saxena S.K. (2006). Lattice dynamics of MgO at high pressure: theory and experiment. *Phys. Rev. Lett.* **96**, art. 035507.
- Paper 13.** Oganov A.R. & Dorogokupets P.I. (2003). All-electron and pseudopotential study of MgO: Equation of state, anharmonicity, and stability. *Phys. Rev. B* **67**, art. 224110.
- Paper 14.** Dorogokupets P.I. & Oganov A.R. (2003). Equations of state of Cu and Ag and the revised ruby pressure scale. *Doklady Earth Sciences* **391A**, 854-857.
- Paper 15.** Oganov A.R. & Dorogokupets P.I. (2004). Intrinsic anharmonicity in thermodynamics and equations of state of solids. *J. Phys.: Cond. Matter.* **16**, 1351-1360.
- Paper 16.** Dorogokupets P.I., Oganov A.R. (2007). Ruby, metals, and MgO as alternative pressure scales: A semiempirical description of shock-wave, ultrasonic, x-ray, and thermochemical data at high temperatures and pressures. *Phys. Rev. B* **75**, art. 024115.
- Paper 17.** Oganov A.R., Glass C.W., Ono S. (2006). High-pressure phases of CaCO₃: crystal structure prediction and experiment. *Earth Planet. Sci. Lett.* **241**, 95-103.
- Paper 18.** Oganov A.R., Glass C.W. (2006). Crystal structure prediction using evolutionary techniques: principles and applications. *J. Chem. Phys.* **124**, art. 244704.
- Paper 19.** Glass C.W., Oganov A.R., Hansen N. (2006). USPEX – evolutionary crystal structure prediction. *Comp. Phys. Comm.* **175**, 713-720.

Paper 20. Martoňák R., Oganov A.R., Glass C.W. (2007). Crystal structure prediction and simulations of structural transformations: metadynamics and evolutionary algorithms. *Phase Transitions*, in press.

Paper 21. Ma Y.-M., Oganov A.R., Glass C.W. (2007). Structure of metallic ζ -phase of oxygen and isosymmetric nature of ϵ - ζ transition. *Phys. Rev. Lett.*, under review.

Paper 22. Oganov A.R., Glass C.W., Ma Y.-Z., Ma Y.-M., Chen J. (2007). Ionic high-pressure form of elemental boron. *Nature*, under review.

Outline of the thesis.

This thesis consists of two main parts. The first gives a brief overview of phenomena, ideas and problems of high-pressure crystallography. It does not attempt to be complete, but serves to provide a framework for the works collected in the second part. To enable coherence, I allowed myself to duplicate material in the first and second parts, but only to a certain necessary extent. Many data presented here are unpublished (in press, submitted, or even in preparation) or even prepared specifically for this thesis. The second part contains reprints of my recent papers, both published and unpublished. In total, there are 22 papers presented in this thesis – which are roughly grouped below by subject area. The main contributions are:

Studies of Earth-forming materials [1-12].

These works have elucidated the nature of the Earth's D'' layer (~2700-2890 km depths) through the joint theoretical/experimental discovery of the post-perovskite phase of MgSiO₃ [1] and prediction of the mechanism of its plastic deformation as well as a series of new possible minerals [2]. A new high-pressure phase of Al₂O₃ was discovered jointly by theory and experiment [3]. The effect of impurities on the stability of post-perovskite has been examined in detail, both by experiment and theory [4,5]. The presence of native Fe in the Earth's lower mantle (670-2890 km depths) has been theoretically justified, confirming previous experimental evidence. Using a novel computational methodology, metadynamics, structural transition mechanisms have been explored in MgSiO₃ [2] and SiO₂ [8] under pressure. Phase diagrams of several important mineral systems have been calculated [1,8-11] using density-functional perturbation theory, establishing this technique as a powerful tool to study *P,T*-phase diagrams. The reliability of this approach has been tested against experimental data on phonon dispersion and thermodynamics functions of MgO under pressure [12].

(Contribution of the author: several projects [2,3,5-7,9-11] were conceived exclusively by the author, who performed all calculations in [1-4, 9-12], student supervision in [5-7] and crystallographic consultation and part of paper writing in [8]. Papers [1-3,9-11] were written almost completely by the author).

Equations of state of simple substances and accurate pressure scales [13-16].

Analysis of intrinsic anharmonic effects in thermodynamics and equations of state of solids, using *ab initio* molecular dynamics simulations [13] and thermodynamic perturbation theory [16]. Experiment-based determination of accurate equations of state of reference substances, used for calibration of pressure scales valid at any temperature and in the pressure range 0-300 GPa [14,16].

(Contribution of the author: papers [13,16] were conceived, carried out and written up mainly by the author. The author significantly contributed to the model formalism exposed in papers [14,17] and significantly contributed to writing these papers, especially [17]).

Development and applications of an evolutionary methodology for crystal structure prediction [17-22].

Crystal structure prediction problem is addressed using the new methodology, merging *ab initio* simulations and a specific evolutionary algorithm developed by A.R. Oganov and C.W. Glass [17-19]. The method has enabled prediction of two new high-pressure phases of CaCO₃ (a likely major host of carbon inside the Earth) [17], new phases of sulphur, oxygen and nitrogen [18,21]. A new phase of elemental boron with ionic bonding was discovered jointly by theory and experiment [22].

(Contribution of the author: conception of the project on method development, and invention of many ingredients of the method, developed jointly with Colin W. Glass (and programmed exclusively by Colin W. Glass). All applications of the method were also proposed (and most also performed) by the author. Papers [17,18,22] were written to the largest extent by the author, who also wrote parts of [19,21] and especially [20]).

Papers on Earth's mantle minerals – especially in the D” layer:

1. Oganov A.R., Ono S. (2004). Theoretical and experimental evidence for a post-perovskite phase of MgSiO₃ in Earth's D” layer. *Nature* **430**, 445-448.
2. Oganov A.R., Martoňák R., Laio A., Raiteri P., Parrinello M. (2005). Anisotropy of Earth's D” layer and stacking faults in the MgSiO₃ post-perovskite phase. *Nature* **438**, 1142-1144.
3. Oganov A.R., S. Ono (2005). The high-pressure phase of alumina and implications for Earth's D” layer. *Proc. Natl. Acad. Sci.* **102**, 10828-10831.
4. Ono S., Oganov A.R. (2005). *In situ* observations of phase transition between perovskite and CaIrO₃-type phase in MgSiO₃ and pyrolytic mantle composition. *Earth Planet. Sci. Lett.* **236**, 914-932.
5. Zhang F., Oganov A.R. (2006). Valence and spin states of iron impurities in mantle-forming silicates. *Earth Planet. Sci. Lett.* **249**, 436-443.
6. Jung D.Y., Oganov A.R. (2005). *Ab initio* study of the high-pressure behaviour of CaSiO₃ perovskite. *Phys. Chem. Minerals* **32**, 146-153.
7. Adams D.J., Oganov A.R. (2006). *Ab initio* molecular dynamics study of CaSiO₃ perovskite at P-T conditions of Earth's lower mantle. *Phys. Rev.* **B73**, 184106.
8. Martoňák R., Donadio D., Oganov A.R., Parrinello M. (2006). Crystal structure transformations in SiO₂ from classical and *ab initio* metadynamics. *Nature Materials* **5**, 623-626.
9. Oganov A.R., Gillan M.J., Price G.D. (2003). Ab initio lattice dynamics and structural stability of MgO. *J. Chem. Phys.* **118**, 10174-10182.

10. Oganov A.R., Gillan M.J., Price G.D. (2005). Structural stability of silica at high pressures and temperatures. *Phys. Rev.* **B71**, art. 064104.
11. Oganov A.R., Price G.D. (2005). *Ab initio* thermodynamics of MgSiO₃ perovskite at high pressures and temperatures. *J. Chem. Phys.* **122**, art. 124501.
12. Ghose S., Krisch M., Oganov A.R., Beraud A., Bossak A., Gulve R., Seelaboyina R., Yang H., Saxena S.K. (2006). Lattice dynamics of MgO at high pressure: theory and experiment. *Phys. Rev. Lett.* **96**, art. 035507.

Papers on equations of state and pressure scales:

13. Oganov A.R. & Dorogokupets P.I. (2003). All-electron and pseudopotential study of MgO: Equation of state, anharmonicity, and stability. *Phys. Rev.* **B67**, art. 224110.
14. Dorogokupets P.I. & Oganov A.R. (2003). Equations of state of Cu and Ag and the revised ruby pressure scale. *Doklady Earth Sciences* **391A**, 854-857.
15. Oganov A.R. & Dorogokupets P.I. (2004). Intrinsic anharmonicity in thermodynamics and equations of state of solids. *J. Phys.: Cond. Matter.* **16**, 1351-1360.
16. Dorogokupets P.I., Oganov A.R. (2007). Ruby, metals, and MgO as alternative pressure scales: A semiempirical description of shock-wave, ultrasonic, x-ray, and thermochemical data at high temperatures and pressures. *Phys. Rev.* **B75**, art. 024115.

Papers on evolutionary crystal structure prediction:

17. Oganov A.R., Glass C.W., Ono S. (2006). High-pressure phases of CaCO₃: crystal structure prediction and experiment. *Earth Planet. Sci. Lett.* **241**, 95-103.
18. Oganov A.R., Glass C.W. (2006). Crystal structure prediction using evolutionary techniques: principles and applications. *J. Chem. Phys.* **124**, art. 244704.
19. Glass C.W., Oganov A.R., Hansen N. (2006). USPEX – evolutionary crystal structure prediction. *Comp. Phys. Comm.* **175**, 713-720.
20. Martoňák R., Oganov A.R., Glass C.W. (2007). Crystal structure prediction and simulations of structural transformations: metadynamics and evolutionary algorithms. *Phase Transitions*, in press.
21. Ma Y.-M., Oganov A.R., Glass C.W. (2007). Structure of metallic ζ -phase of oxygen and isosymmetric nature of ϵ - ζ transition. *Phys. Rev. Lett.*, under review.
22. Oganov A.R., Glass C.W., Ma Y.-Z., Ma Y.-M., Chen J. (2007). Ionic high-pressure form of elemental boron. *Nature*, under review.

PART I. INTRODUCTION: New phenomena and open problems in high-pressure crystallography.

1. Importance of studies of matter at extreme conditions.

Studies of matter at high pressures and temperatures are important for three reasons:

- interiors of the Earth, planets and stars are characterised by very high pressures and temperatures (3.65 Mbar at the centre of the Earth – Fig. 1a). At such conditions the structure and properties of materials differ drastically from what can be observed at atmospheric pressure (as can be seen from discontinuities in Fig. 1b) and no reliable extrapolations can be made. Therefore, compressed planetary matter has to be studied *in situ*, i.e. at planetary P - T conditions.
- to achieve true understanding of chemical bonding, it is necessary to study the response of structure and bonding to external conditions – pressure and temperature. Many unusual phenomena have been discovered at high pressure, and some of these are still to be explained.
- since pressure alters chemical bonding and structure, often creating unusual materials with unusual properties, it can be exploited for synthesis of new materials.

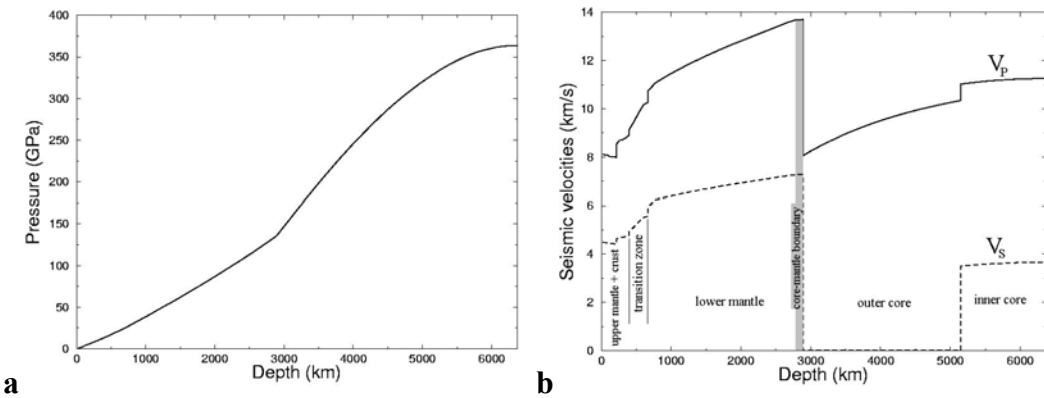


Fig. 1. Distributions of pressure (a) and seismic wave velocities (shear, V_s , and compressional, V_p) in the Earth's interior [1].

2. Pressure and temperature as thermodynamic variables.

In a close system at given P - T conditions the stable state has the lowest possible Gibbs free energy G :

$$G = E + PV - TS , \quad (1)$$

where E is the internal energy, V the volume, and T the entropy. On increasing pressure, the volume must decrease; likewise, the entropy must increase on increasing temperature. Any pressure-induced phase transition leads to a denser phase. This can occur via one of several possibilities, all of which occur experimentally in different cases:

-More efficient packing and, ultimately, tendency towards close-packed structures on increasing pressure. Classical examples would be the bcc-hcp transition in Fe at 13 GPa [2] or the coesite-stishovite-CaCl₂ transitions in SiO₂ [3]. However, this trend is violated in many cases including even seemingly simple elements. For instance, Mg transforms from a hexagonal close-packed structure into a non-close-packed body-centred cubic phase at \sim 50 GPa [2]. After a series of close-packed structures, upon increasing pressure beyond 200 GPa SiO₂ also adopts non-close-packed pyrite and cotunnite structures [3].

-Decrease of atomic sizes due to electronic transitions. The classical examples are electronic transitions in SmS (Fig. 2) and Ce, where the structure type remains the same across the transition (NaCl-type and Cu-type, respectively), but the density discontinuously increases by \sim 15% [2]. Electronic transitions provide a very plausible explanation of many structural complexities that have been discovered under pressure. For instance, electronic s \rightarrow d transition occurs in many metals under pressure (e.g., Cs, Ba, Rb, Ca, K) and creates partly covalent directional bonds [4]. Thus, these normal metals become transition metals under pressure, with entirely different (complex low-symmetry) structures and properties (typically, superconductors at low temperatures and poor metals at room temperature). This also creates interesting geochemical consequences. For instance, it may result in a large miscibility of K in liquid Fe under pressure, and since ⁴⁰K is major source of radiogenic heat in the Earth, create an energy production mechanism within the Earth's iron-rich core (the other major radiogenic elements, U and Th, almost certainly cannot enter the core in any sizable quantities) [5].

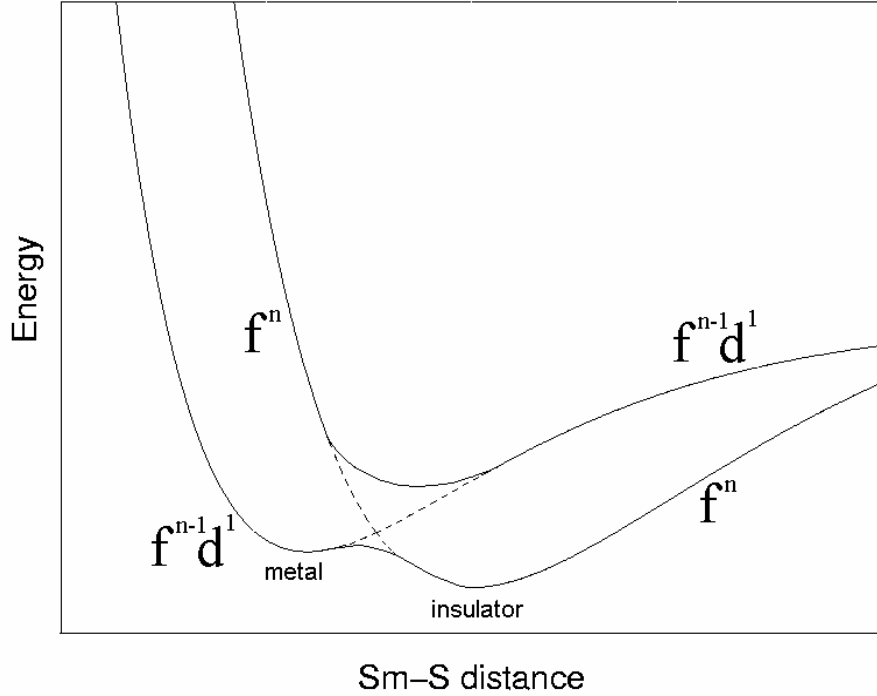


Fig. 2. Illustration of the isosymmetric metal-insulator transition in SmS. After [6], with modifications. Mixing of two configurations (metallic $f^{n-1}d$ and insulating f^n) produces a double-well energy curve for the ground state, where the minimum with a smaller interatomic distance corresponds to a metal. Compression triggers the insulator-metal transition.

Under sufficiently high pressure, the PV -term in (1) becomes dominant and traditional concepts of chemical bonding (based on the E -term) become invalid. Many chemical compounds stable at low pressures, decompose at high pressures (e.g., Al_2SiO_5 decomposes into $\text{Al}_2\text{O}_3 + \text{SiO}_2$, [7,8]), or, vice versa, new exotic compounds can be formed under pressure. A good example is the chemical reaction between inert gas Xe and SiO_2 , which under pressure produces some xenon compound and free Xe [8]. Another example is the rich chemistry of platinoids under pressure: e.g., Pt reacts with diamond at >80 GPa forming PtC [10,11].

Upon compression, the fastest-growing energy term is the electronic kinetic energy:

$$E_{kin,e} = \langle \Psi | -\frac{\hbar^2}{2m_e} \nabla^2 | \Psi \rangle , \quad (2)$$

where Ψ is the wavefunction, \hbar is the Planck constant, and m_e the mass of the electron. Since kinetic energy (2) dominates at ultrahigh pressures, energy minimisation is reduced to the minimisation of (2) – which is achieved in the free-electron gas. Thus, one concludes that the ultimate state of matter under compression is a free-electron

gas: a normal metal (without superconductivity) with maximally delocalised electrons. Energy contributions for the free-electron gas are shown in Fig. 3. However, this limit is reached only at extraordinarily high pressures ($>>1$ a.u.=29.4 TPa), and at all practically interesting compressions there is a competition between kinetic and potential energy terms (which favour electron delocalisation and localisation, respectively). Due to the increasing tendency towards electron delocalisation, strongly localised and directional covalent bonds (especially multiple bonds – e.g. in N_2) become unfavourable. In molecular crystals, pressure triggers an instability of the molecular state. In ionic crystals, strong localisation of valence electrons on the anions becomes gradually less favourable. It is expected that under pressure bands broaden until the band gap disappears. However, this rule also has exceptions and opposite phenomena (opening of the band gap in metals under pressure) have been predicted for Li [12] and Ca [13].

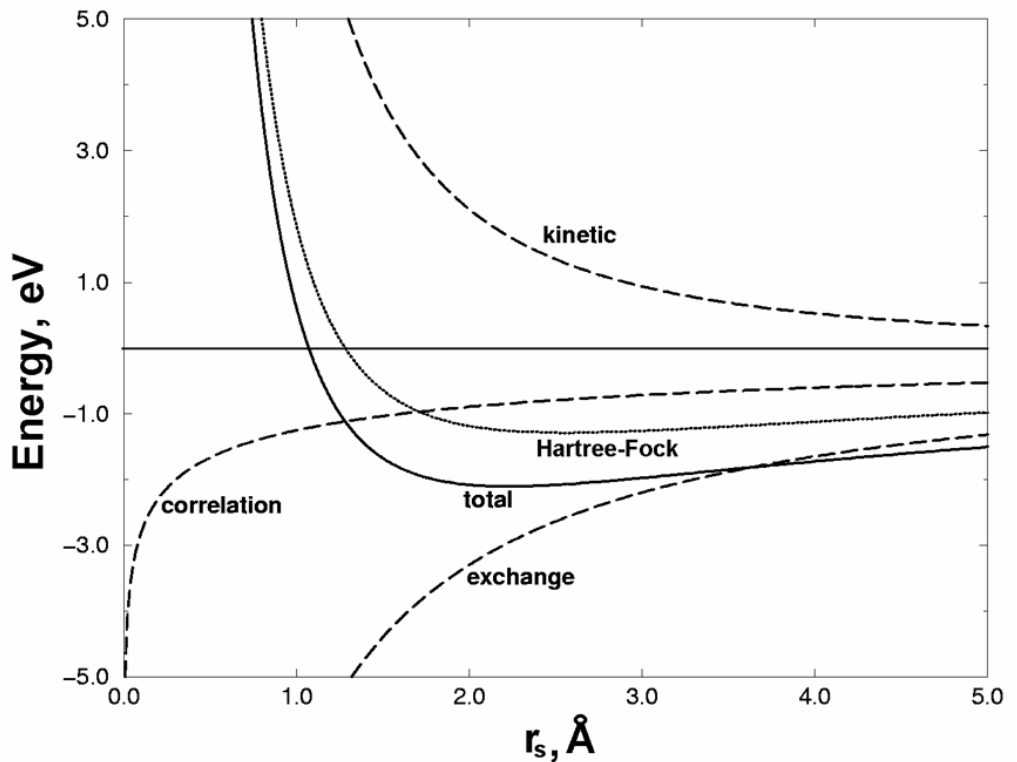


Fig. 3. Energy contributions for the homogeneous electron gas (per 1 electron). r_s is the Wigner-Seitz radius. Average r_s values of the valence electrons of several metals are shown. Redrawn with modifications from [14]. Hartree-Fock curve includes all the contributions except correlation. It is clear that correlation is non-negligible.

3. Experimental methods for research at extreme conditions.

The notion of “high pressure” is relative: pressure is “high” if it causes a large (and, especially, unexpected) response of the object. Thus, what we call “high pressure” depends on the discipline: for biologists pressures in the range 1-10 atm are high. For us (material scientists, Earth scientists) such pressures are extremely low, and usually only pressures $> 3\text{-}5 \text{ GPa}$ are considered as sufficiently high.

To generate such conditions, three main types of devices are used:

1. Large-volume presses, especially multianvil and toroidal presses (often incorrectly called Paris-Edinburgh cells).
2. Diamond anvil cells.
3. Shock guns for dynamic compression.

Diamond anvil cell is the most versatile tool for high-pressure research: pressures up to $\sim 300\text{-}400 \text{ GPa}$ and temperatures up to $\sim 4000 \text{ K}$ can be reached in a controllable way, and numerous measurements can be made in such experiments (e.g., X-ray diffraction, to study structure and mechanical properties; inelastic X-ray scattering, IR- and Raman spectroscopy to study lattice dynamics; optical, X-ray emission, and Mössbauer spectroscopy to explore the electronic structure). A typical setup of the laser-heated diamond anvil cell is shown in Fig. 4. The main disadvantages are that often it is difficult to achieve thermal and chemical equilibrium. The problem of thermal equilibrium is quite serious, since diamond anvils have a very high thermal conductivity; however, a technical solution has been found (and involves a thermally insulating material and a large heating spot with double-sided heating) – the resulting thermal profiles show only moderate temperature gradients in the sample (Fig. 5). Another problem is that the pressure is typically non-hydrostatic and non-uniform, and that at ultrahigh pressures there are large uncertainties in pressure calibration (reaching more than $\pm 50 \text{ GPa}$ at pressures of $\sim 200\text{-}300 \text{ GPa}$).

The main advantages of large-volume presses (with which pressures up to $\sim 25 \text{ GPa}$ are routinely achieved) is that chemical and thermal equilibrium is quite easy to attain. For shock-wave experiments, the main advantages are the unique range of pressures and temperatures that can be achieved (to $\sim 100 \text{ TPa}$ and $10^{4\text{-}5} \text{ K}$) and the possibility of absolute pressure measurement. Among main disadvantages are the short duration of shock ($10^{-6}\text{-}10^{-9} \text{ s.}$) during which most measurements cannot be done and equilibrium often cannot be established, and that essentially a single $P\text{-}T$ trajectory can only be sampled.

In shock-wave experiments, temperature is generated by fast compression (e.g., as in adiabatic compression). Pressure is easily calculated from experimental parameters through the Rankine-Hugoniot equation (see [15,16]), whereas the temperature can be either modelled, or measured by pyrometry. Since in shock-wave experiments the absolute values of pressure are directly accessible, these experiments play a unique role in the development of pressure standards for static compression experiments.

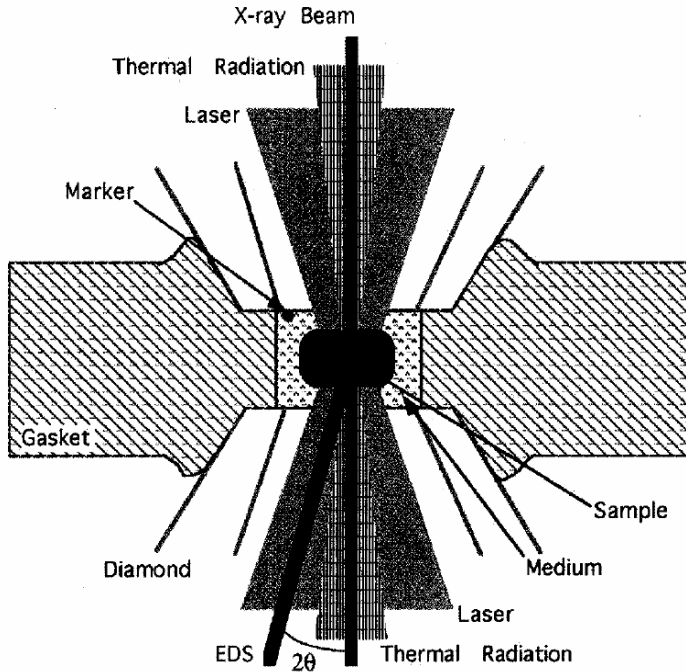


Fig. 4. Schematics of a laser-heated diamond anvil cell (after [17]).

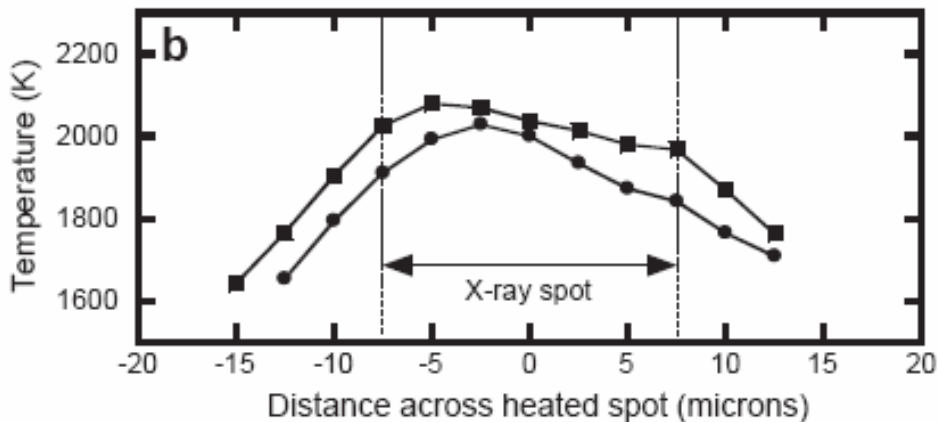


Fig. 5. Temperature distribution across a sample of KLB-1 pyrolite in a laser-heated diamond anvil cell [18]. Two lines indicate temperatures measured pyrometrically from both sides of the sample.

In static experiments (with diamond anvil cells or large-volume presses), temperature is generated either by resistive heating or by absorption of infrared laser radiation.

Temperatures can be measured either by thermocoupler, or pyrometrically. In pyrometry, the temperature is fitted to the thermal radiation of the sample, assuming the black body radiation model [19]:

$$dN_\omega \sim \frac{\omega^2 d\omega}{e^{\hbar\omega/k_B T} - 1} , \quad (3)$$

where dN_ω is the number of photons with the frequency ω , \hbar is the Planck constant, k_B the Boltzmann constant, and T is the temperature. Pressure is inferred indirectly, using phase transitions as pressure markers, or (much more commonly) equations of state or other properties (e.g., luminescence or Raman line shifts) of precalibrated pressure markers mixed in with the sample.

Let us consider the essence of the problem of pressure calibration in static experiments. We will not discuss in detail the numerous efforts to create reliable pressure scales, the main trends are illustrated in Fig. 6 for the ruby pressure scale. One can see that pressure scales have considerably evolved (the true pressures are believed to be between scales [22] and [23]) and that the use of older scales [20,21] results in very large errors. In this case, to measure pressure (only at room temperature) one needs to know the dependence of the measured R_1 luminescence lineshift $\Delta\lambda$ on pressure. To find this dependence, experiments are done where the compressed sample contains both a ruby chip and a material with known $P(V)$ equation of state. The most accurate experiments of this kind (using helium as pressure-transmitting medium) were recently done by Dewaele *et al.* [24]. The equation of state of reference materials is usually found from shock-wave measurements; the main problem is that shock measurements are done at very high temperatures (and temperature along the shock Hugoniot $P_H(V)$ increases with pressure), whereas it is the isothermal room-temperature $P(V)$ dependence that is needed. The two are related [15]:

$$P(V) = P_H \left[1 - \gamma \frac{1-x}{2x} \right] + \frac{\gamma}{V} [E(V) - E_0] , \quad (4)$$

where γ is the Grüneisen parameter and $x = (V/V_0)^{1/3}$, V_0 and E_0 are the volume and internal energy in the reference state (at 1 atm and 298.15 K). Clearly, to reduce Hugoniots to room-temperature isotherms $P(V)$ one has to know the Grüneisen parameter $\gamma(V)$. There is a “vicious circle” problem here: to calibrate pressure at room temperature, we use absolute pressure measurements at high temperatures and, to reduce these data to room temperature one needs to have the unknown Grüneisen parameter $\gamma(V)$. This parameter could be found if we knew simultaneously the shock

Hugoniot and a static compression curve – which brings us back to the initial problem. Usually, a number of crude assumptions are made in the functional dependence and values of $\gamma(V)$. This parameter can be found theoretically, from first principles, and with excellent accuracy [25]. However, an experimental determination is necessary to establish a purely experimental high-pressure metrology. Besides, some effects (thermal defects at very high and quantum nuclear motion at low temperatures) might be difficult to simulate consistently.

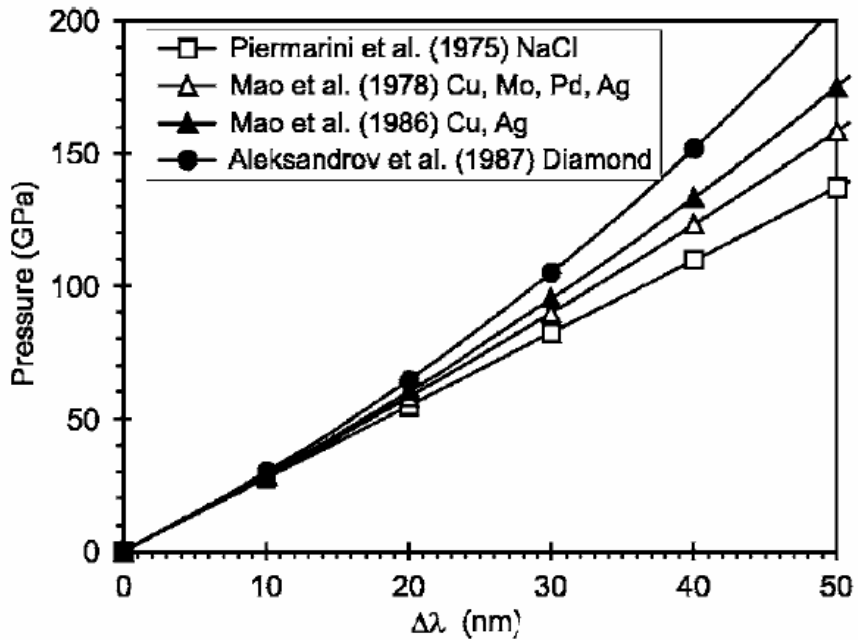


Fig. 6. Evolution of the ruby pressure scale: from the linear relation of Piermarini [20] to the non-hydrostatic non-linear scale of Mao *et al.* [21], to the quasihydrostatic scale of Mao [22] and a revised scale of Aleksandrov *et al.* [23]. In each case, materials used for primary calibration are indicated.

A solution to the “vicious circle” problem was found recently [26,27]. In this approach, we start with an analytical expression for the Helmholtz free energy $F(V,T)$ – parameters of this expression are initially unknown, and are found using experimental data. The expression we developed includes a static compression term (in the Vinet or Birch-Murnaghan forms), quasiharmonic and intrinsic anharmonic terms (for the latter, a special quantum treatment was developed [28], enabling a physically meaningful description of both low- and high-temperature regimes), and terms describing the contributions of thermal defects and conduction electrons. At the first stage, we use only data unbiased by pressure calibration – i.e. shock-wave data and measurements at 1 atm (calorimetric determinations of thermodynamic functions (C_P, S, H), X-ray and dilatometric data on thermal expansion, ultrasonic and Brillouin

spectroscopic determinations of the isothermal and adiabatic bulk moduli (K_T , K_S) as a function of temperature). All these experimental measurements can be easily calculated from $F(V,T)$ and, thus, be used for its parameterisation. The $F(V,T)$ function contains also the room-temperature isotherm $P(V)$, as well as any other isotherm and the $\gamma(V)$ function. Once we have found $F(V,T)$, we can calibrate the ruby scale $\Delta\lambda(P)$ using the measurements of Dewaele et al. [24]. Using the newly found pressure scale, we recalibrate experimental static compression data and, including them in the second state of our procedure, refine parameters of $F(V,T)$ again. Typically, the number of observables is $\sim 10^2$ times larger than the number of parameters. With this approach one obtains not only versatile and accurate pressure scales, but also the most reliable $P-V-T$ equations of state of reference solids [27]. Other recent pressure scales, utilising certain assumptions or results of *ab initio* calculations, are quite similar to our scale (Fig. 7). The problem of pressure calibration can now be considered a solved problem – both in principle and, within small uncertainties, also in practice.

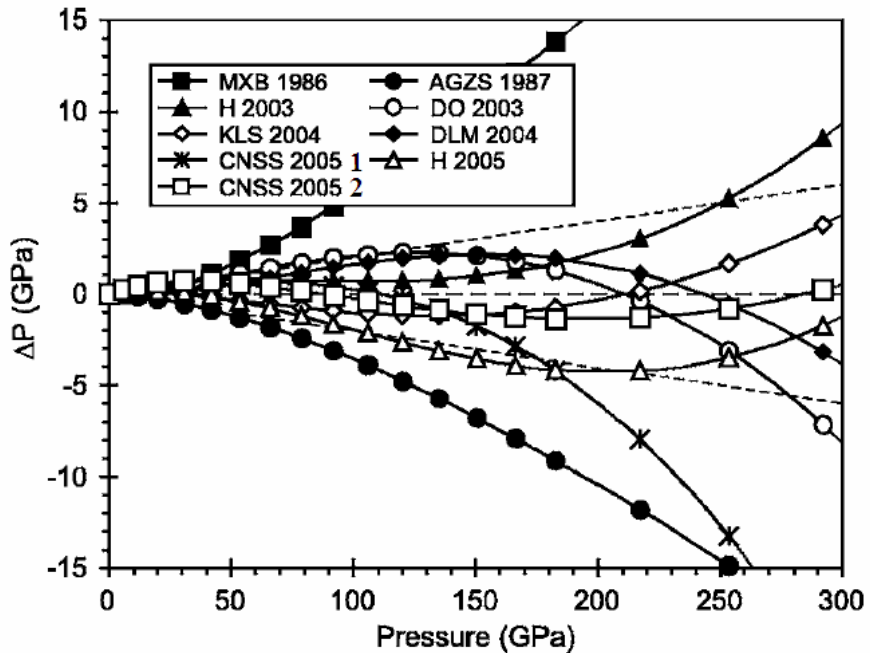


Fig. 7. Different calibrations of the ruby pressure scale. ΔP is the difference between scale [27] and a preceding scale: MXB 1986 [22], AGZS [23], H 2003 [29], DO 2003 [26], KLS 2004 [30], DLM [24], CNSS 2005 [31], H 20005 [32]. P is the pressure according to the scale [27].

4. Computational methods for high-pressure research.

Keeping in mind the three main goals of high-pressure research, outlined in Section 1, we can formulate the main tasks that theory has to solve with reasonable accuracy:

1. Prediction of the stable crystal structure at given P - T conditions, given only the chemical formula (and, perhaps, some partial experimental information).
2. Prediction of the response of crystal structure to pressure and temperature, as well as to chemical substitutions and disorder.
3. Calculation of the electronic structure of pure and defective crystals, to enable understanding of chemical bonding and electronic properties of materials – electron density $\rho(\mathbf{r})$, electronic band structure $\varepsilon(\mathbf{k})$ and density of states $n(\varepsilon)$, impurity energy levels.
4. Calculation of lattice dynamics – phonon dispersion curves $\omega(\mathbf{k})$ and densities of states $n(\omega)$, electron-phonon coupling coefficients λ , Grüneisen parameters γ (mode-specific γ_{ik} and thermodynamic γ) and intrinsic anharmonicity parameters a (also mode-specific and thermodynamic average values), IR- and Raman spectra (including linewidths and intensities).
5. Calculation of the elastic, dielectric and piezoelectric constants.
6. Calculation of thermodynamic properties as a function of pressure and temperature, prediction of phase diagrams.
7. Prediction of transport properties – thermal and electrical conductivities, viscosities.

While modern computational methods should be considered as an extremely powerful tool, most of these tasks are associated with “hot” problems. Even the basic electronic structure calculations and structure optimisations are a challenging task for whole classes of compounds – Mott insulators and molecular crystals. However, this is a rapidly developing field and major breakthroughs in many of these areas are likely to be made in the near future. For tasks 2-6 there is a well-established theoretical and methodological framework. Task 1 was considered to be impossible to solve [32] until very recently [34-37], and for task 6 there are still major methodological problems related to problematic time- and length-scales involved in transport processes.

Computer simulation is one of the fastest-growing areas of science, and new methods and significant developments appear continually. Our introduction here is, by necessity, brief – more details can be found in original papers and in a number of reviews [5,38-48].

The most basic approximation used in most simulation methods is the Born-Oppenheimer approximation, which (due to the large difference of masses of the nuclei and electrons) decouples electronic and nuclear motion and allows one to find the electronic ground state at fixed nuclear positions. There is a whole hierarchy of methods for treating electronic and nuclear degrees of freedom.

In atomistic methods, the subtleties of the electronic structure are ignored and all relevant physics is condensed into a parameterised expression of the total energy as a function structure (interatomic distances, angles, etc.). Such methods enable fast large-scale simulations, but depend on the quality of the interatomic potential – both the analytical form and parameters. Outside the range of parameterisation, the applicability of such methods can be questionable. Electronic and magnetic structure and all related effects cannot be addressed at this level of theory.

4.1. Modern electronic structure calculations.

In the so-called “first-principles” (or, *ab initio*) methods, an attempt is made at solving the Schrödinger equation (or its analogues) without any empirical system-specific parameters. Such simulations give, in principle, all relevant information on the atomic, electronic and magnetic structure of materials. However, they are computationally very demanding ($\sim 10^3$ times more expensive than atomistic simulations) and cannot be done without approximations. For solids, 3 *ab initio* methodologies are most popular – Hartree-Fock (see, e.g., [14]), density functional theory (DFT) (see, e.g., [47]), quantum Monte Carlo [49] approaches. We should also mention hybrid density-functional approaches [50], which have become very popular in molecular chemistry. Due to their computational efficiency and comparatively good accuracy, density-functional methods are the mainstream in condensed matter research and are the main workhorse in my group’s research.

The total energy of a non-relativistic electron-nuclear system and all its energy levels can be calculated by solving the Schrödinger equation, which can be written (in the atomic units) as:

$$\left[\sum_{i=1}^N \left(-\frac{\nabla_i^2}{2} \right) + \frac{1}{2} \sum_A \sum_{i=1}^N \frac{Z_A}{|\mathbf{R}_A - \mathbf{r}_i|} + \frac{1}{2} \sum_{i=1}^N \sum_{j=1}^N \frac{1}{|\mathbf{r}_i - \mathbf{r}_j|} \right] \psi = E \psi , \quad (5)$$

where \mathbf{r}_i are electronic and \mathbf{R}_A are nuclear coordinates, Z_A is the nuclear charge, N is the number of electrons and the term in brackets is the electronic Hamiltonian. The first term in the Hamiltonian is the kinetic energy operator and the following terms

are the electron-nuclear and electron-electron potential energy operators, respectively; E is the electronic energy (to find the total energy, one needs to add to it the nuclear-nuclear interaction energy).

The major problem in solving (5) is that the wavefunction is a function of $3N$ electronic coordinates (where N is the number of electrons) – which for condensed systems is of the order of 10^{23} . The most common computational methods are based on approximate one-electron theories, reducing (5) to a set of coupled equations for separate one-electron orbitals, e.g. the Hartree-Fock equations:

$$\varepsilon_i \phi_i(\mathbf{r}) = \left\{ -\frac{\nabla_i^2}{2} + \frac{1}{2} \sum_A \sum_{i=1}^N \frac{Z_A}{|\mathbf{R}_A - \mathbf{r}_i|} + \int \frac{\rho(\mathbf{r}')}{|\mathbf{r} - \mathbf{r}'|} d\mathbf{r}' + \sum_j \delta_{oi, oj} \int d\mathbf{r}' \frac{\phi_j^*(\mathbf{r}') \phi_j(\mathbf{r}')}{|\mathbf{r} - \mathbf{r}'|} \right\} \phi_i(\mathbf{r}), \quad (6)$$

where ϕ_i are one-electron wavefunctions, and ε_i are the orbital energies, and the last term in the Hamiltonian is the Hartree-Fock exchange operator.

DFT is a revolutionary theory in quantum mechanics: it formulates quantum mechanics in terms of the observable and tractable electron density instead of the extremely complicated and unobservable wavefunction. Its rigorous foundation was laid in the works Kohn and his colleagues and followers [51-53]. The two fundamental Hohenberg-Kohn theorems imply that the total energy of a system is uniquely determined by the electron density distribution $\rho(\mathbf{r})$ through a universal functional $F[\rho(\mathbf{r})]$, and that the ground-state $\rho(\mathbf{r})$ minimises $F[\rho(\mathbf{r})]$ [51]. Extension of Hohenberg-Kohn theorems to finite temperatures was done by Mermin [53]. To avoid problems with calculating electronic kinetic energy as a functional of the electron density (although such functional does exist, it is unknown and likely to be exceedingly complicated), Kohn and Sham [52] devised a method, which enables accurate practical calculations. This is a formally exact one-electron theory. We introduce a wavefunction¹ and calculate the kinetic energy T_S of this fictitious non-interacting system as a sum over all occupied orbitals:

$$T_S = \sum_i^{\text{occup}} \left\langle \phi_i \mid -\frac{1}{2} \nabla^2 \mid \phi_i \right\rangle \quad (7)$$

The total electron density is found, as in any one-electron theory, as a sum over orbitals:

$$\rho(\mathbf{r}) = \sum_i^{\text{occup}} |\phi_i|^2(\mathbf{r}) \quad (8)$$

¹ Which in Kohn-Sham theory is but an auxiliary construction with no real physical meaning other than a tool to calculate the electronic kinetic energy.

The total electronic energy is:

$$E[\rho] = T_S[\Psi \rightarrow \rho] + \int d\mathbf{r} \rho(\mathbf{r}) \left(\sum_A \frac{Z_A}{|\mathbf{R}_A - \mathbf{r}|} \right) + \frac{1}{2} \int d\mathbf{r} \rho(\mathbf{r}) \int d\mathbf{r}' \frac{\rho(\mathbf{r}')}{|\mathbf{r}' - \mathbf{r}|} + E_{xc}[\rho], \quad (9)$$

where the second term in the electron-nuclear potential energy, the second term is the so-called Hartree energy (Coulombic self-interaction energy of the electron density distribution), and the fourth term is the exchange-correlation energy. By definition [52], E_{xc} includes the term compensating for the errors of eq. (7) – therefore this term includes complicated effects of various nature and its presence makes theory formally exact. Since kinetic energy terms are subsumed in E_{xc} , virial theorem does not hold in the Kohn-Sham DFT – even if the exact functional were known [54].

We will not dwell on the theory of exchange-correlation effects, - this topic, central to DFT, has been addressed in numerous works (see an overview in [54-56]). Perhaps the most surprising finding is that already the simplest approximation, the local density approximation (LDA), where the exchange-correlation energy at each point is approximated by that of a homogeneous electron gas with the corresponding density $\rho(\mathbf{r})$, is remarkably successful. No doubt, this is due to the important property of ‘short-sightedness’ of the electrons – which is present in all but exotic chemical systems (such as stretched covalent bonds).

In LDA, the exchange-correlation energy is calculated as:

$$E_{xc}[\rho] = \int d\mathbf{r} \rho(\mathbf{r}) e_{xc}(\rho(\mathbf{r})) , \quad (10)$$

where the exchange energy density of a homogeneous electron gas is known exactly:

$$e_x(\rho) = -\frac{3}{4\pi} (3\pi^2)^{1/3} \rho^{1/3} = -\frac{3}{4\pi} (9\pi/4)^{1/3} r_s^{-1} , \quad (11)$$

where r_s is the Wigner-Seitz radius (radius of a sphere containing 1 electron). The correlation energy density is known very accurately from quantum Monte Carlo simulations [57,58] and can be represented analytically as follows [59]:

$$e_c(\rho) = -2c_0(1+\alpha_1 r_s) \ln \left[1 + \frac{1}{2c_0(\beta_1 r_s^{1/2} + \beta_2 r_s + \beta_3 r_s^{3/2} + \beta_4 r_s^2)} \right] , \quad (12)$$

where $c_0=0.031091$ and $c_1=0.046644$, $\beta_1=\frac{1}{2c_0} \exp(-\frac{c_1}{2c_0})=7.5957$, $\alpha_1=0.21370$,

$\beta_2=2c_0\beta_1^2=3.5876$, $\beta_3=1.6382$, and $\beta_4=0.49294$ for the spin-unpolarised ($\xi=0$) electron gas. For a fully spin-polarised case $c_0=0.015545$ and $c_1=0.025599$, $\alpha_1=0.20548$, $\beta_3=3.3662$, and $\beta_4=0.62517$. The interpolation for intermediate values of spin polarisation has been derived in [60]. Functions (11) and (12) have been

plotted in Fig. 3. For almost all materials, LDA shows the following errors: it underestimates the energies of free atoms, band gaps (by a factor of $\sim 2\text{-}3$), bond lengths and cell parameters (by $\sim 1\text{-}3\%$), and overestimates (by $\sim 20\%$) atomisation energies of molecules and solids. The most severe problems are encountered for Mott insulators and for the description of van der Waals bonding.

The next level of approximation, the generalised gradient approximation (GGA), also calculates exchange-correlation energy locally, but taking into account also the density gradient at the given point:

$$E_{xc}[\rho, \nabla \rho] = \int d\mathbf{r} F_{xc}(\rho, \nabla \rho) \rho(\mathbf{r}) e_x(\rho(\mathbf{r})) , \quad (13)$$

where the enhancement factor $F_{xc}(\rho, \nabla \rho)$ now depends on both the density and its gradient. The most popular and physically meaningful GGA functional was derived in [61]. This GGA is not constructed as a Taylor expansion adding a gradient term to the LDA; this approach is known to fail. Instead, it is a carefully constrained gradient expansion made to fulfil all the properties of the exact functional satisfied by the LDA, and a number of additional properties, including the following:

- It reduces to the LDA for homogeneous densities, and to the Taylor-expansion of the LDA for slowly varying densities.
- It obeys the Lieb-Oxford bound, which can be written as follows:

$$F_{xc}(\rho, \nabla \rho) \leq 2.273 \quad (14)$$

GGA significantly improves the description of atomic core electrons and to some extent the valence electrons as well. Total energies are much better than in the LDA and even better than in the Hartree-Fock approximation. LDA overbinding is corrected by the GGA. Energy differences and especially reaction barriers are often significantly improved, as well as the description of magnetic systems. However, bond lengths are usually overestimated (by $\sim 1\%$), and problems in the description of band gaps, Mott insulators and van der Waals bonding remain. Table 1 compares the performance of different approximations for three archetypal solids (covalent, ionic, metallic). One can observe reasonable accuracy, especially at the GGA level of theory. Table 2 shows that even for a relatively complicated low-symmetry structure of kyanite the accuracy of theory at the GGA level is rather good. Even more impressive is the accuracy of the predicted phase transition pressures: as we showed on a number of cases, at the GGA level of theory they are often within 0-3 GPa of the experimental value [3,8,11,18,63].

Very recently, a promising non-empirical meta-GGA functional was derived [64]. At the meta-GGA level of theory, the exchange-correlation energy is expressed as a function of local electron density $\rho(\mathbf{r})$, its gradient $\nabla\rho(\mathbf{r})$, and kinetic energy density $\tau(\mathbf{r})$:

$$E_{xc}[\rho, \nabla\rho, \tau] = \int d\mathbf{r} e_{xc}(\rho, \nabla\rho, \tau) \rho(\mathbf{r}) \mathbf{r} \quad , \quad (15)$$

where, as before, e_{xc} is the exchange-correlation energy density. The kinetic energy density τ is expressed via the wavefunction:

$$\tau(\mathbf{r}) = \sum_i^{\text{occup}} \frac{1}{2} |\nabla\phi_i(\mathbf{r})|^2 \quad (16)$$

TABLE 1. Performance of theoretical approximations for selected crystals. V_0 , K_0 , K_0' , E_{at} are the zero-pressure unit cell volume, bulk modulus (incompressibility) and its pressure derivative, and atomisation energy. Compiled from several sources in [44].

Property	Hartree-Fock	LDA	GGA	Experiment
Diamond (C)				
V_0 , Å ³	45.88	43.99	45.50	45.38
K_0 , GPa	471	455	438	442
E_{at} , eV	-5.2	-8.87	-7.72	-7.55
Periclase (MgO)				
V , Å ³	73.61	71.99	76.44	74.09
K_0 , GPa	186	198	157	167
E_{at} , eV	-7.32	-	-	-10.28
Ferromagnetic bcc Fe				
V , Å ³	-	10.44	11.34	11.77
K_0 , GPa	-	260	200	172
K_0'	-	4.6	4.5	5.0

Becke [65] showed that $\tau(\mathbf{r})$ is a useful indicator of delocalisation of the exchange hole. Conventional functionals fail for systems with significantly delocalised exchange holes (such as stretched H₂⁺) because of large self-interaction error. Including $\tau(\mathbf{r})$ it is possible to accurately model the exchange energy of systems with highly delocalised exchange holes [65]. This meta-GGA has been extensively tested for atoms and molecules, but very few results exist for solids [66]. From the existing data, this functional appears to be clearly superior to the LDA and GGA in practically all respects. Results of some molecular tests [67] are given in Table 3. The band gap problem is likely to be nearly as severe in the meta-GGA as it is in the GGA and LDA. However, the two other problems (in modelling van der Waals interactions and Mott insulators) appear to be significantly reduced.

TABLE 2. Crystal structure of kyanite Al_2SiO_5 : comparison of the GGA calculation [8] with experiment [62].

	GGA calculation	Experiment
Kyanite (space group $P\bar{1}$; $Z=4$).		
Unit cell parameters and volume		
$A_0, \text{\AA}$	7.185	7.1262
$B_0, \text{\AA}$	7.916	7.8520
$C_0, \text{\AA}$	5.613	5.5724
$\alpha, {}^\circ$	89.9	89.99
$\beta, {}^\circ$	101.1	101.11
$\gamma, {}^\circ$	106.0	106.03
$V_0, \text{\AA}^3$	300.6	293.60
Atomic coordinates		
Al1	(0.3247, 0.7039, 0.4581)	(0.3254, 0.7040, 0.4582)
Al2	(0.2966, 0.6986, 0.9502)	(0.2974, 0.6989, 0.9505)
Al3	(0.0994, 0.3864, 0.6407)	(0.0998, 0.3862, 0.6403)
Al4	(0.1116, 0.9170, 0.1645)	(0.1120, 0.9175, 0.1649)
Si1	(0.2961, 0.0650, 0.7066)	(0.2962, 0.0649, 0.7066)
Si2	(0.2909, 0.3315, 0.1896)	(0.2910, 0.3317, 0.1892)
O_a	(0.1105, 0.1461, 0.1284)	(0.1095, 0.1468, 0.1288)
O_b	(0.1230, 0.6858, 0.1816)	(0.1230, 0.6856, 0.1812)
O_c	(0.2735, 0.4550, 0.9556)	(0.2747, 0.4545, 0.9547)
O_d	(0.2816, 0.9341, 0.9338)	(0.2831, 0.9354, 0.9353)
O_e	(0.1218, 0.6300, 0.6389)	(0.1219, 0.6307, 0.6389)
O_f	(0.2810, 0.4447, 0.4289)	(0.2822, 0.4453, 0.4288)
O_g	(0.2901, 0.9465, 0.4658)	(0.2915, 0.9467, 0.4659)
O_h	(0.5018, 0.2770, 0.2449)	(0.5008, 0.2749, 0.2440)
O_k	(0.1091, 0.1532, 0.6682)	(0.1084, 0.1520, 0.6669)
O_m	(0.5024, 0.2298, 0.7560)	(0.5015, 0.2312, 0.7553)

TABLE 3. Performance of the LDA, GGA and meta-GGA for selected diatomic molecules [66].

Molecule	Bond lengths, \AA				Atomisation energies, kcal/mol			
	LDA	GGA	Meta-GGA	Expt.	LDA	GGA	Meta-GGA	Expt.
H ₂	0.765	0.750	0.743	0.741	113.2	104.6	112.9	109.5
Li ₂	2.708	2.729	2.749	2.673	23.9	19.9	22.5	24.4
LiF	1.543	1.568	1.566	1.564	156.1	138.6	135.7	138.9
N ₂	1.096	1.103	1.101	1.098	267.4	243.2	227.7	228.5
O ₂	1.206	1.220	1.222	1.208	175.0	143.7	126.9	120.5
F ₂	1.385	1.414	1.415	1.412	78.4	53.4	46.4	38.5

It is likely that very complicated functionals are needed to describe van der Waals interactions adequately; nevertheless, there are already some promising approaches [68,69]. Band structure (including band gaps) can be accurately (with errors of ± 0.1 eV) simulated, e.g. using many-body perturbation theory (GW method [70]). Strongly correlated systems (e.g., Mott insulators) can be treated with such methods as DFT+U [71], DFT-SIC [72], or dynamical mean field theory [73]. All of these

problems can be solved using the nearly exact quantum Monte Carlo calculations [49]. As Table 3 shows, such calculations (at the diffusion Monte Carlo level) account for ~95% of the electron correlation energy.

TABLE 4. Performance of the Hartree-Fock (HF) and diffusion Monte Carlo (DMC) methods for total energies of atoms and molecules. E_0 is the exact non-relativistic energy (in atomic units), E_{HF} is the Hartree-Fock energy. Percentage of the correlation energy recovered in DMC is also given. From [74].

	E_0	E_{HF}	E_{DMC}	E_c^{DMC} (%)
Li	-7.478	-7.433	-7.478	99.7
Be	-14.667	-14.573	-14.667	99.7
C	-37.845	-37.689	-37.835	93.6
O	-75.067	-74.804	-75.052	94.1
O ₂	-150.327	-149.666	-150.272	91.7
H ₂ O	-76.438	-76.068	-76.418	94.5
CH ₄	-40.515	-40.219	-40.504	96.3
C ₆ H ₆	-232.247	-230.82	-232.156	93.6

Once the Hamiltonian (at a certain level of approximation) is set up, the numerical solution of the Schrödinger equation (or its analogues – Hartree-Fock or Kohn-Sham equations) has to be obtained. Numerous approximate methods exist, differing in:

-The basis set: wavefunctions are usually either expanded in plane waves, or obtained as a linear combination of local atoms-centred orbitals. Hybrid basis functions (such as LAPW functions, which become plane waves outside of atomic spheres, and localized functions inside the spheres) are also often used.

-The number of electrons explicitly treated: all-electron or pseudopotential methods. In the latter, only valence electrons are explicitly considered, the effect of core electrons on the valence electrons being represented by an effective potential called pseudopotential.

-In many methods, the space is separated into “atomic spheres” and “interstitials”. The wavefunction may be either represented in the same manner throughout the crystal or is considered separately inside spheres and in the interstitials and then matching conditions are applied at the sphere boundaries.

-The presence or absence of approximations in the crystal potential – full-potential vs “atomic sphere” approximations (in the latter, the potential is usually spherically averaged within atomic spheres).

In solid-state simulations, the most mature methods use plane-wave basis sets and pseudopotential (see [40,75-79]) or projector-augmented wave (PAW) [80-82] methodologies, and these are used here. The popularity of plane-wave methods is due to the fact that the plane-wave basis set is complete, can be automatically made to converge to any needed precision, and is mathematically extremely convenient. The main drawback is that an extremely large number of plane waves are needed to describe localized wavefunctions. This is particularly severe for core electrons and for oscillations of the valence wavefunctions close to the nucleus – these difficulties are removed in the pseudopotential approximation, which replaces the core electrons by their effective potential, and the true valence wavefunctions by smooth and nodeless pseudo-wavefunctions, which match the true wavefunction everywhere outside a sphere of radius r_c . At r_c and beyond, not only the wavefunction, but also the potential and their first derivatives are exact. Pseudopotentials should closely reproduce the all-electron eigenvalues in as many different electronic configurations as possible, for transferability to chemically different systems. r_c needs to be small enough (less than half of the nearest-neighbour distance) to enable accurate calculations. Figs. 8,9 give examples of the “pseudisation” of the valence wavefunctions. To reduce the number of plane waves per atom needed for a given level of precision, ultrasoft pseudopotentials have been devised [77] – there, the rapidly varying part of valence wavefunctions are described by auxiliary localized functions. Comparison of the performance of pseudopotential and all-electron methods (e.g. [82]) shows that pseudopotential calculations are accurate, except where core polarisation effects are significant (e.g., Ca atom in CaF₂). Another source of errors is the overlap of the valence and core orbitals for some elements (e.g., Na). In such cases, non-linear core corrections [78] improve pseudopotentials. The PAW method [80,81] is a further development of the pseudopotential methodology, close to the spirit of ultrasoft pseudopotentials and enabling all-electron calculations at the price of a pseudopotential calculation. It operates with the full valence wavefunction, which is represented as plane waves throughout the space, plus the rapidly varying part (including oscillations and nodal behaviour) within atom-centred spheres. Core electrons are usually assumed to be frozen and taken from an atomic calculation; therefore PAW is a frozen-core all-electron method (however, in principle it is also possible to make core electrons variational). Table 5 compares pseudopotential and PAW results with the results of the all-electron LAPW (Linearised Augmented Plane Wave) method, which is today’s standard of

highest accuracy in density functional calculations (all results in Table 5 were obtained within the LDA). Excellent consistency between PAW and LAPW (and, to a large extent, pseudopotential) results is obvious.

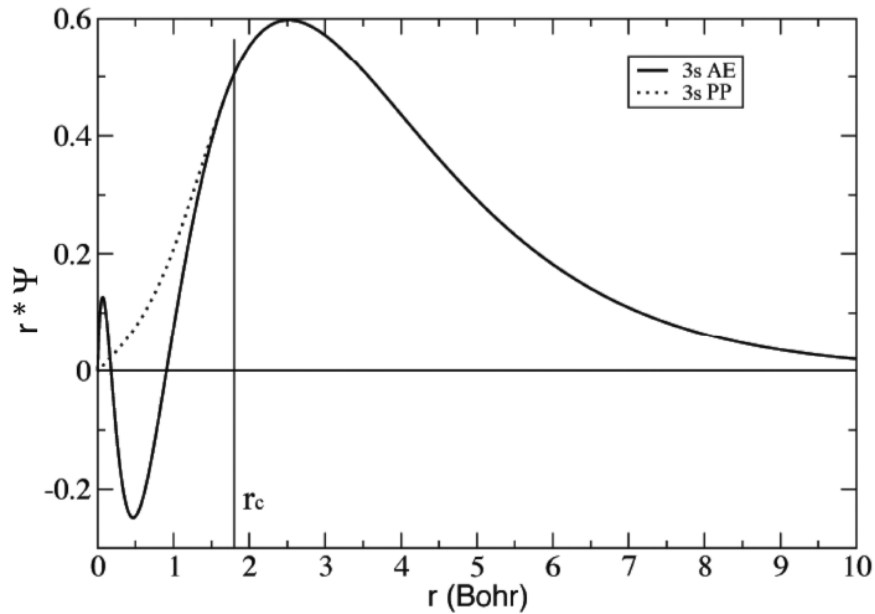


Fig. 8. Construction of a pseudopotential for Mg. Beyond r_c the pseudowavefunction (PP) and pseudopotential match the true all-electron (AE) ones. From [45].

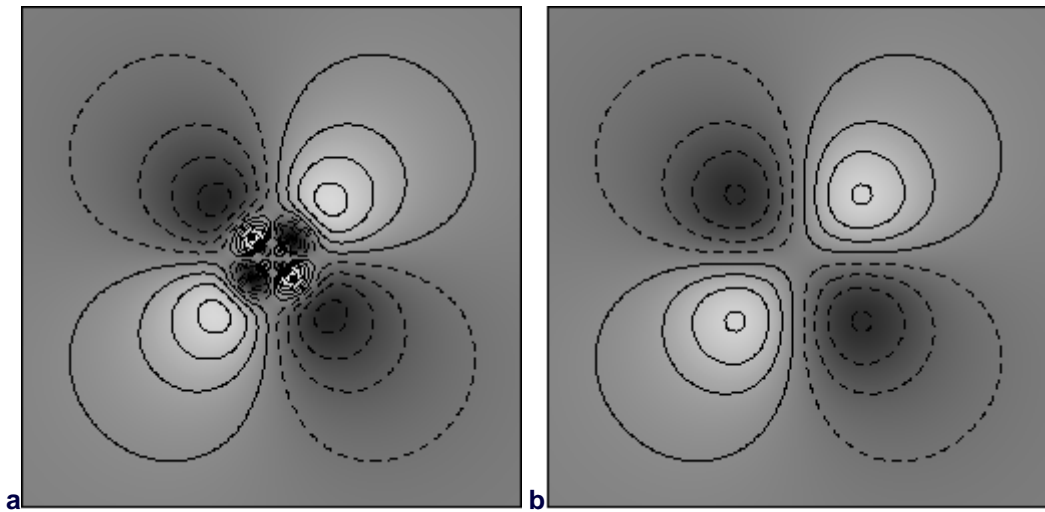


Fig. 9. All-electron (a) and pseudowavefunction (b) of a 5d-orbital in Au. Solid contours – positive, dashed contours – negative wavefunction. Courtesy of A.M. Rappe.

Fig. 10 shows the GGA equation of state of MgO calculated using ultrasoft pseudopotentials (in both cases, O atoms had a He-like $1s^2$ core, while for Mg two cases were considered - with small Be-like $1s^22s^2$ core and large Ne-like $1s^22s^22p^6$

core), and using the PAW method (with the same choice of atomic cores). One can see that for pseudopotential calculations the choice of the core configuration is more important than for PAW, and that the quality of large-core pseudopotential calculations degrades at very high pressures. A small systematic difference (approximately constant, several GPa shift in pressure) between theory and experiment is seen in Fig. 10. Insightful discussions of other technical issues of *ab initio* calculations (e.g., basis set choice and convergence, Brillouin zone sampling) can be found in [14,48,83]. Numerous *ab initio* codes exist; we use state-of-the-art packages VASP [84] and ABINIT [85,85], in most cases using the GGA-PAW level of theory (except phonon calculations, all of which have been performed with the LDA and pseudopotentials). Both codes can be used to perform standard static density-functional calculations and *ab initio* molecular dynamics calculations with high accuracy and speed, using plane-wave basis sets and pseudopotentials (norm-conserving and ultrasoft), or the PAW method. With ABINIT one can also study lattice dynamics of solids using density-functional perturbation theory, and perform GW calculations [70].

TABLE 5. Comparison of cohesive energies E_{coh} [eV/atom], equilibrium lattice constants a_0 [\AA] and bulk moduli K_0 [GPa] calculated using the PAW, LAPW and pseudopotential methods. Data a are from [82], b from [81], and c are experimental results quoted in [82].

	Method	E_{coh}	a_0	K_0		Method	E_{coh}	a_0	K_0
Diamond	a PAW	10.16	3.54	460	CaF ₂	a PAW	6.36	5.34	100
	a LAPW	10.13	3.54	470		a LAPW	6.30	5.33	110
	b PAW	10.11	3.54	460		b PAW	6.35	5.34	101
	b pseudopotential	10.12	3.54	461		b Pseudopotential	6.35	5.34	101
	a pseudopotential	10.13	3.54	460		a Pseudopotential	6.42	5.21	90
	c experiment	7.37	3.56	443		c Experiment	5.36	5.45	85-90
Silicon	a PAW	6.03	5.38	98	fcc Ca	a PAW	2.24	5.32	19
	a LAPW	5.92	5.41	98		a LAPW	2.20	5.33	19
	b PAW	5.96	5.40	95		b PAW	2.19	5.34	18.5
	b pseudopotential	5.96	5.40	95		b Pseudopotential	2.18	5.34	18.3
	a pseudopotential	5.99	5.39	98		a Pseudopotential	2.14	5.37	20
	c experiment	4.63	5.43	99		c Experiment	1.84	5.58	15
SiC	a PAW	8.39	4.32	220	bcc V	a PAW	9.39	2.94	200
	a LAPW	8.29	4.33	230		a LAPW	9.27	2.94	200
	a pseudopotential	8.35	4.33	230		b PAW	9.39	2.93	210
	c experiment	6.34	4.36	224		b Pseudopotential	9.42	2.93	206
						a Pseudopotential	9.46	2.94	210
						c Experiment	5.31	3.03	162

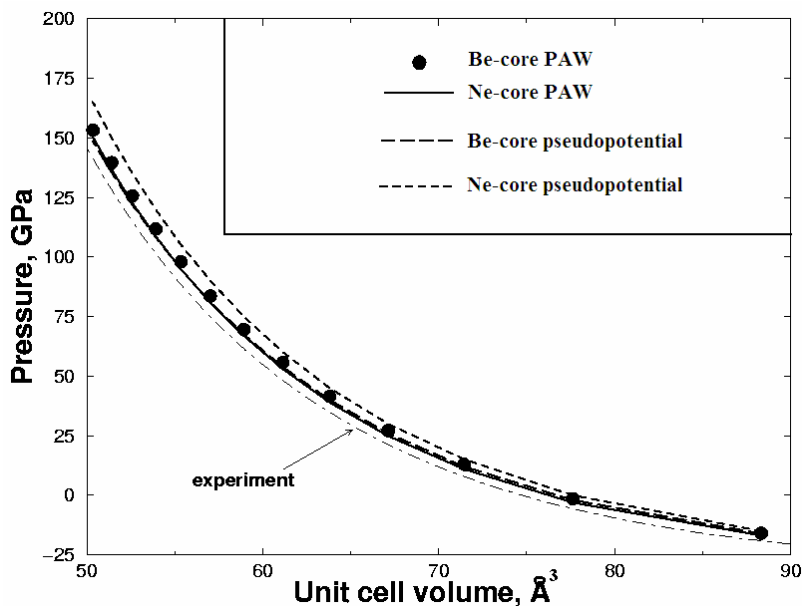


Fig. 10. Equation of state of MgO: comparison of pseudopotential and PAW methods. From [25], modified.

Being able to calculate the total energies of solids with reasonable accuracy, we are in a position to explore (at least, in principle) their thermodynamic behaviour and physical properties. Recall that the partition function:

$$Z = \sum_i e^{-E_i/k_B T} , \quad (17)$$

where the summation is carried out over all discrete energy levels of the system, is directly related to all thermodynamic properties, e.g. the Helmholtz free energy:

$$F = E_0 - k_B T \ln Z , \quad (18)$$

where E_0 is the ground-state energy (at 0 K). Derivatives of thermodynamic potentials determine a host of physical properties (one example, phonon frequencies, will be discussed in the next section). Usually, Z is calculated either approximately (within the quasiharmonic approximation), or by numerical sampling of the phase space (for reasons of numerical stability, it is usually not the absolute value of Z that is calculated, but its ratio to a partition function of a well-known model system). Two major *ab initio* methodologies for treating thermal effects in solids, quasiharmonic lattice dynamics and molecular dynamics, are briefly discussed in the following section.

4.2. *Ab initio* molecular dynamics and quasiharmonic approximation.

These two methodologies are largely complementary [87]: molecular dynamics (MD) considers atoms as classical particles exploring the true anharmonic energy surface,

whereas in the quasiharmonic approximation (QHA) nuclear motion is quantum, but in the harmonically truncated potential. Therefore, MD is ideally suited for strongly anharmonic systems above the Debye temperature (where nuclear quantum effects are negligible). The QHA should be applied at temperatures below 0.5-0.7 T_m (T_m is the melting temperature), because at higher temperatures anharmonic effects become essential. These approaches, and their *ab initio* implementations, are covered in [38,39, 88-93].

In MD, we describe a classical system by the set of positions and velocities ($\mathbf{r}_i(t)$, $\mathbf{v}_i(t)$) of all particles. For a system of N atoms there are $(3N-3)$ degrees of freedom, and the kinetic energy is:

$$E_{\text{kin}} = \sum_{i=1}^N \frac{m_i |\mathbf{v}_i|^2}{2} = \frac{(3N-3)k_B T}{2} \quad (19)$$

The initial kinetic energy (or temperature) is specified as an input, and the initial velocities are assigned to the atoms randomly, according to the Maxwell distribution. During thermal motion, the system gradually equilibrates and reaches the steady state. Having initial velocities thus specified and starting from the input configuration, the system evolves with the atoms exploring trajectories, which are constructed by solving classical equations of motion, with a finite timestep Δt (rather than infinitesimal dt). The standard algorithm for integrating the equations of motion is the Verlet leapfrog algorithm:

$$\mathbf{r}_i(t+\Delta t) = 2\mathbf{r}_i(t) - \mathbf{r}_i(t-\Delta t) \frac{\mathbf{F}_i(t)}{m_i} (\Delta t)^2 , \quad (20)$$

where $\mathbf{F}_i(t)$ is the force acting on the i -th atom. The error in the positions is of the order $(\Delta t)^4$. Δt must be sufficiently small (typically ~ 1 fs). At each step the positions and velocities change, the forces have to be recalculated and the new positions predicted according to (20).

For condensed-phase simulations, it is imperative to use large supercells and impose periodic boundary conditions, in order to include a sufficient number of phonon wavevectors and avoid surface effects. To gather sufficient statistics, the simulation has to be run long enough after equilibration. Most properties can be obtained from MD in one of the three ways: 1) time-averaging of the instantaneous values, 2) analysis of fluctuations of the instantaneous values, 3) via correlation functions. The free energy, unlike many of its derivatives, is not an ensemble average and cannot be determined from MD directly; instead the free energy relative to a

well-known reference state can be calculated using thermodynamic integration [88,89].

Newtonian equations of motion are conservative, and without additional ingredients the method implies conservation of the total energy, volume, and the number of particles – or, the *NVE*-ensemble. It is possible to extend MD to other ensembles (e.g., *NVT*, *NPT*), using extended Lagrangian formulations. In the constant-temperature (*NVT*-) method of Nosé (1984), the extended Lagrangian is:

$$L = \sum_i \frac{m_i |\dot{\mathbf{v}}_i|^2}{2} - E_{\text{pot}}(\mathbf{r}) + \frac{1}{2} Q \dot{s}^2 - (f+1)k_B T_0 \ln s, \quad (21)$$

where s is the new dynamical variable, and Q is the associated mass parameter. T_0 is the externally set temperature, and f is the number of degrees of freedom in the system. This Lagrangian leads to conservation of the temperature, which fluctuates around T_0 . The most important constant of motion is the Hamiltonian - the sum of the real energy and the fictitious Nosé terms. Recalling that classical equations of motion can be represented in the Lagrangian form as:

$$\frac{d}{dt} \left(\frac{\partial L}{\partial \dot{r}_i} \right) = \left(\frac{\partial L}{\partial r_i} \right), \quad (22)$$

we obtain the equations of motion for the *NVT*-ensemble, with modified forces:

$$m_i \ddot{\mathbf{r}}_i = \frac{1}{s^2} \mathbf{F}_i - \frac{2}{s} \dot{s} \dot{\mathbf{p}}_i \quad (23)$$

$$Q \ddot{s} = \sum_i m_i s |\dot{\mathbf{r}}_i|^2 - \frac{(f+1)k_B T_0}{s} \quad (24)$$

The choice of the mass parameter Q does not affect the canonical averages in principle, but in order to approach these averages in reasonably short time, it is better to choose Q so that the period of oscillation of the temperature (or s) is similar to the average period of atomic vibrations.

In a similar way, Parrinello and Rahman [95] devised a constant-pressure version of MD. They added into the Lagrangian an extra potential term (PV) and kinetic term

$(\frac{1}{2} Q \sum_{\alpha} \sum_{\beta} \dot{\mathbf{H}}_{\alpha\beta}^2)$, where $\mathbf{H}_{\alpha\beta}$ is the matrix of lattice vectors). Car and Parrinello [96]

applied the same trick to construct the first scheme of *ab initio* MD simulations, where both atomic coordinates and electronic coordinates (plane wave coefficients $C_{\mathbf{k}+\mathbf{K}}$) evolve simultaneously with time. The forces on atoms are computed, at each step, using the Hellmann-Feynman theorem:

$$\mathbf{F}_i = -\frac{\partial E}{\partial \mathbf{r}_i} = -\langle \psi | \frac{\partial \hat{H}}{\partial \mathbf{r}_i} | \psi \rangle - \frac{\partial E_{n-n}}{\partial \mathbf{r}_i}, \quad (25)$$

where the first term is the expectation value of the position derivative of the electronic Hamiltonian (with the minus sign), and the second term is the electrostatic nuclear-nuclear force.

The Car-Parrinello method is discussed in detail in [90]. More modern versions of *ab initio* MD are based on the determination of the ground state at each atomic configuration ('Born-Oppenheimer dynamics'); this method is more stable and more suitable for metals. Some of the significant advances in Earth and planetary sciences [97-103] have been obtained with *ab initio* MD simulations. This is the method of choice for accurate simulations of significantly anharmonic phenomena, such as melting, ionic conductivity, displacive phase transitions, high-temperature thermal expansion and elastic properties. Fig. 11 illustrates thermal motion of the oxygen atoms in the high-pressure phase of Al₂O₃.

MD approaches described above use classical dynamics of the atoms (even if the electrons are explicitly treated as quantum particles, as in *ab initio* MD) and therefore are inadequate at low temperatures, where quantum effects are essential. Quantum nuclear effects can be incorporated either through path integral MD [88], or by applying quantum corrections [104]. The quantum correction for the Helmholtz free energy per atom in the lowest order is [19]:

$$\Delta F = F(\text{quantum}) - F(\text{classical}) = \frac{\hbar^2}{24k_B T} \left\langle \sum_i \frac{\nabla_i^2 E_{\text{pot}}}{m_i} \right\rangle, \quad (26)$$

where ∇_i^2 is the Laplacian with respect to the coordinates of the i-th atom. Quantum corrections to other properties can be worked out by differentiating (26) – see [104].

We have used *ab initio* MD to study thermoelasticity of MgSiO₃ perovskite [99,105], the mineral which makes ~75 vol.% of the Earth's lower mantle. The results refuted the previous pure-perovskite model of the composition of the lower mantle [106], and, coupled with seismic tomography images, provided a new insight into the thermal structure of the Earth's mantle. In another work [107] *ab initio* MD was used to investigate phase transitions of CaSiO₃ perovskite at high pressures and temperatures; this material was confirmed to be cubic at all conditions of the lower mantle.

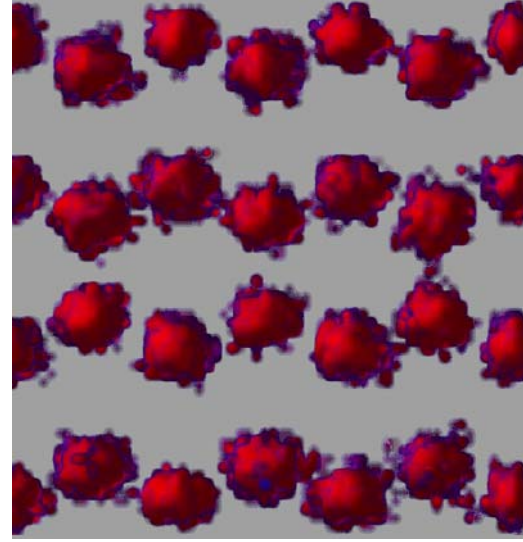


Fig. 11. Cumulative trajectory of oxygen atoms in the CaIrO₃-type phase of Al₂O₃ at 100 GPa and 3000 K (result of an *ab initio* molecular dynamics simulation).

Theory of quasiharmonic lattice dynamics has been discussed in great detail in [38,39,48,91-93], here we give only a brief summary. In the quasiharmonic approximation, at each volume we expand the potential energy to second order in displacements from equilibrium:

$$E = E_0 + \frac{1}{2} \sum_{i\alpha l} \sum_{i\beta l'} \left(\frac{\partial^2 E}{\partial u_\alpha^i(l) \partial u_\beta^{i'}(l')} \right) u_\alpha^i(l) u_\beta^{i'}(l') , \quad (27)$$

where E_0 is the energy corresponding to equilibrium, and $u_\alpha^i(l)$ is a displacement of an i -th atom in the l -th unit cell along the α -coordinate axis. Expression (27) is valid only when atomic displacements are small (i.e. at low temperatures). It contains the interatomic force constants matrix $\Phi_{\alpha\beta}^{ij}(l, l')$:

$$\Phi_{\alpha\beta}^{ij}(l, l') = \frac{\partial^2 E}{\partial u_\alpha^i(l) \partial u_\beta^{i'}(l')} , \quad (28)$$

which relates forces to the displacements:

$$\mathbf{F}_\alpha^i(l) = - \sum_{j\beta l'} \Phi_{\alpha\beta}^{ij}(l', l) u_\beta^{i'}(l') \quad (29)$$

The elements of the dynamical matrix \mathbf{D} are defined as:

$$D_{\alpha\beta}^{ik}(\mathbf{k}) = \frac{1}{(m_i m_j)^{1/2}} \sum_l \Phi_{\alpha\beta}^{ij}(0, l) \exp[i\mathbf{k}(\mathbf{r}_j(l) - \mathbf{r}_i(0))] , \quad (30)$$

where m_i and m_j are masses of the i -th and j -th atoms, summation is over all unit cells, and $\Phi_{\alpha\beta}^{ij}(0, l)$ are force constants between the atom i in the reference cell ($l=0$)

and atom j in the l -th cell, whose positions are described by vectors $\mathbf{r}_i(l)$ and $\mathbf{r}_j(0)$. To obtain phonon frequencies ω at given \mathbf{k} -vector, one should solve the following secular equation:

$$\det[\mathbf{D}(\mathbf{k}) - \omega^2(\mathbf{k}, \nu) \delta_{\alpha\beta} \delta_{ij}] = 0 , \quad (31)$$

where \mathbf{D} is the dynamical matrix, and ω^2 are its eigenvalues. Solving the eigenvalue problem (41) is equivalent to the diagonalisation of the dynamical matrix, whose dimensions are $3N \times 3N$. This leads to $3N$ solutions. Negative ω^2 (i.e., imaginary ω) indicate dynamical instability of the structure with respect to the corresponding displacement.

To solve the lattice dynamics problem from first principles, two approaches are commonly used: 1) finite displacement method (where the force constants are determined from the forces, appearing after imposing small displacements in a large supercell), 2) density-functional perturbation theory [48, 92, 93, 108, 109]. The first approach is rather obvious, so we briefly comment on the second method. One starts with the Hellmann-Feynman theorem (25), which in certain cases can be rewritten as follows:

$$\mathbf{F}_\alpha^i(l) = -\frac{\partial E_{n-n}}{\partial u_\alpha^i(l)} - \int \frac{\partial E_{n-e}(\mathbf{r})}{\partial u_\alpha^i(l)} \rho(\mathbf{r}) d^3 r , \quad (32)$$

where E_{n-n} and E_{n-e} are the nucleus-nucleus and electron-nucleus Coulomb energies, respectively. This expression involves only the classical effects, but the expression for second derivatives is more complicated:

$$\Phi_{\alpha\beta}^{ij}(l, l') = \frac{\partial^2 E_{n-n}}{\partial u_\alpha^i(l) \partial u_\beta^j(l')} + \int \frac{\partial^2 E_{n-e}(\mathbf{r})}{\partial u_\alpha^i(l) \partial u_\beta^j(l')} \rho(\mathbf{r}) d^3 r + \int \frac{\partial \rho(\mathbf{r})}{\partial u_\alpha^i(l)} \frac{\partial E_{n-e}(\mathbf{r})}{\partial u_\beta^j(l')} d^3 r , \quad (33)$$

the last term of which is non-trivial and involves the response of the electron density to an atomic displacement, to find which perturbation theory is used (see [48, 92, 93, 108] for details). The high accuracy of phonon calculations based on density-functional perturbation theory is illustrated in Fig. 12; we have demonstrated [110] that this accuracy is retained also at high pressure. Quasiharmonic lattice dynamics has been used to study high-temperature elasticity in the pioneering work of Karki *et al.* [112].

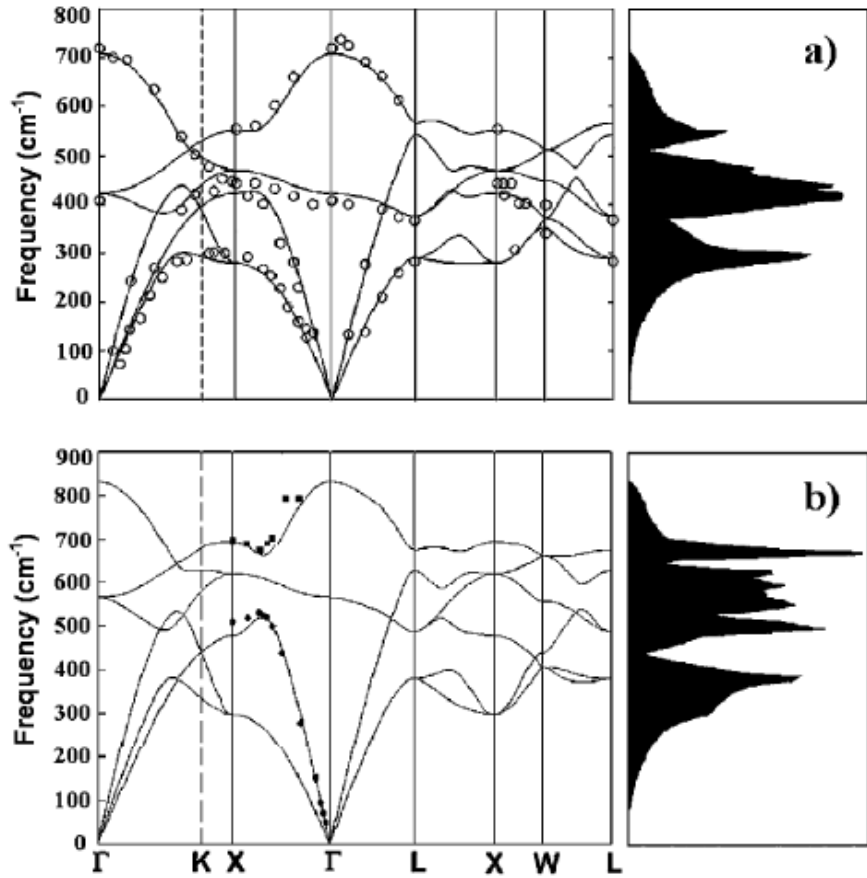


Fig. 12. Phonon dispersion curves and densities of states of MgO 1) at 1 atm, b) at 35 GPa. Lines – LDA results obtained using density-functional perturbation theory, symbols – experiments. From [110].

From phonon frequencies, it is straightforward to calculate thermodynamic properties within the QHA; for instance, the Helmholtz free energy is:

$$F(V, T) = E_0(V) + \int_0^{\omega_{\max}} \frac{1}{2} \hbar \omega g(\omega) d\omega + k_B T \int_0^{\omega_{\max}} \ln[1 - \exp(-\frac{\hbar\omega}{k_B T})] g(\omega) d\omega, \quad (34)$$

where E_0 is the energy of the static lattice. The Gibbs free energy is then:

$$G(P, T) = F(V, T) - V \left(\frac{\partial F(V, T)}{\partial V} \right)_T \quad (35)$$

Comparing the Gibbs free energies of different phases, one can compute P - T phase diagrams (only solid-solid transitions can be studied using the QHA), see Fig. 13. Such studies became feasible only recently [3,11,113-116], and we have done some of the first of these works. In particular, we have established the stability field of the newly discovered post-perovskite phases of MgSiO₃ [11] and Al₂O₃ [115], clarified the phase diagram of SiO₂ and showed that phase transitions of silica cannot cause mid-mantle discontinuity at 1200 km depth [3]. We also showed [114] that MgSiO₃

perovskite and post-perovskite are stable against decomposition into $\text{MgO} + \text{SiO}_2$ at all lower mantle conditions. This agrees with most experimental STUDIES (see references in [114]) and refutes previous suggestions of decomposition [117,118]. We have used methods of density-functional perturbation theory to calculate infrared absorption and LO-TO splitting in the newly discovered ionic form of boron [119], to calculate Raman frequencies of the newly predicted structure of metallic oxygen [120], and to explore instabilities of alkali metals under pressure [121].

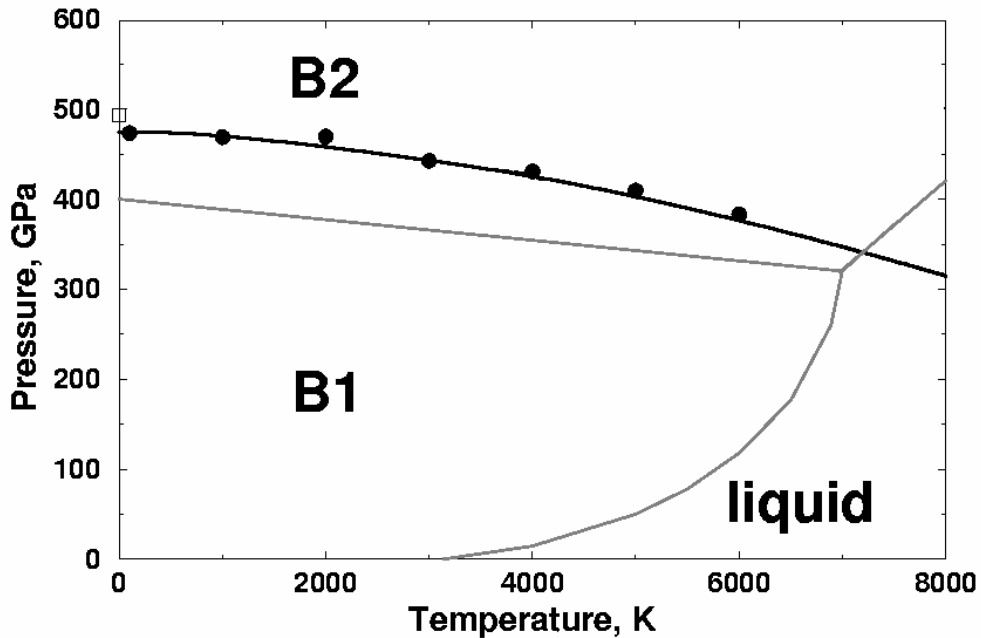


Fig. 13. Predicted phase diagram of MgO. Black – from density-functional perturbation theory [113], gray – classical MD result of [111]. Square – static transition pressure. From [113].

4.3. Crystal structure prediction: evolutionary algorithms and metadynamics.

Structure is the most important characteristic of a material, defining many of its properties. Yet, prediction of likely structural topologies (structure types) on fully theoretical grounds remains a major unsolved problem. Standard simulation methods require a trial model of the structure and are only able to optimise it locally (i.e. by modifying the atomic positions and lattice parameters to reduce forces and stresses) or in a very small neighbourhood on the energy landscape (using MD).

In the standard approach, one explores a list of likely structures (e.g., known from other compounds) and, comparing their free energies, determines which phases are stable at which conditions. This approach is often successful in predicting new phases : e.g., the prediction [122] that at high pressures Al_2O_3 will be more stable in

the $\text{Rh}_2\text{O}_3(\text{II})$ structure than in the corundum structure was subsequently verified experimentally [123]. Motivated by the finding of a CaIrO_3 -type post-perovskite phase of Fe_2O_3 [124], *ab initio* simulations suggested high-pressure stability of CaIrO_3 -type phases in MgSiO_3 [11] and Al_2O_3 [115] (see also [125]) above 1 Mbar. Both predictions are consistent with experiment [11,115,126]. However, this approach will fail if an unexpected structure is stable, and high-pressure crystallography abounds with cases of unexpected structures. E.g., early simulations of Al_2O_3 under pressure [127] did not consider the CaIrO_3 -type structure and incorrectly predicted stability of the perovskite structure above 2 Mbar. In reality, this structure is never stable, because of the greater stability of the CaIrO_3 structure. It is necessary to be able to predict structures “blindly”, i.e. not relying on experimental information of any kind.

It was believed to be impossible to find the stable structure at give P - T conditions, knowing just the chemical composition [128-130]. In the words of John Maddox:

“One of the continuing scandals in the physical sciences is that it remains in general impossible to predict the structure of even the simplest crystalline solids from a knowledge of their chemical composition... Solids such as crystalline water (ice) are still thought to lie beyond mortals’ ken”.

These words still remain largely true, as evidenced by poor results of the latest blind test for crystal structure prediction [131]. Solving this problem would be invaluable for discovering new minerals of planetary interiors, and for computational materials design.

The problem of crystal structure prediction can be reformulated as a global optimisation problem – to find the stable structure, one needs to locate the global minimum of the free energy (or another relevant thermodynamic potential) in space of all structural variables (atomic coordinates, lattice vectors). However, this global optimisation is made difficult by the high dimensionality of the problem (the dimensionality is $3N+3$, where N is the number of atoms in the unit cell), the astronomically large number of possible structures for a given chemical composition, and the rugged energy landscape. We [35] estimated that for an element A (compound AB) with 10 atoms in the unit cell there are $\sim 10^{11}$ (10^{14}) physically distinct structures for a system, and this number increases factorially to 10^{25} (10^{30}) for a system with 20 atoms/cell, and 10^{39} (10^{47}) for the case of 30 atoms/cell. One faces an NP-hard problem here, and this problem cannot be solved by exhaustive search methods - except for the simplest systems with ~ 1 -10 atoms in the unit cell. To solve this problem, one can either start already in a good region of configuration

space (so that no effort is wasted on sampling poor regions), or use a “self-improving” method, which “zooms in” on the most promising regions.

The first group of methods includes metadynamics [34,132,133], simulated annealing [134,135], basin hopping [136] and minima hopping [137] approaches. Metadynamics is clearly the most efficient of these methods (the only one enabling *ab initio* structure prediction), but the price to pay is the dramatic reduction of the search space (from $3N+3$ to just 6) and frequent failures of this method. Simulated annealing is extremely inefficient (a typical run requires millions of energy evaluations, and hundreds of such runs are needed - [135]) and cannot be used for large systems. Minima hopping method is promising, but is very expensive and so far used almost exclusively for aperiodic systems (clusters). The advantage of such methods is that they provide important information on possible mechanisms of structural transformations, and often result in long lists of low-energy metastable structures (which are also of much interest).

The second group essentially includes only evolutionary algorithms [35-37,138-141]. The main idea is to mimic Darwinian evolution and employ natural selection to find the optimal solution. Evolutionary algorithms usually are population based, and new structures are produced by applying variation operators on structures of the current population. However, the construction of the algorithm (e.g., representation, fitness function, variation operators, constraint techniques and halting criteria) will depend on the nature of the problem at hand and will affect the performance of the algorithm tremendously [142]. A major strength of evolutionary algorithms is their learning power, the ability to find promising parts of the solution. Evolutionary algorithms have been applied to crystal structure prediction for the case of fixed lattice parameters [138-140]. That algorithm employed a cheap heuristic fitness function (instead of the physical free energy), a discrete grid for atomic positions, and encoded structural information in binary “0/1” strings. In spite of many simplifications, this approach turned out to be computationally expensive; thorough tests [139,140] showed that it often fails even for simple structures –e.g. TiO₂ anatase. The problem was that this algorithm involved very little learning, and did not address the problem of noisy landscapes. Another evolutionary algorithm is more intuitively correct [141], but was developed and tested only for clusters and was never extended to periodic structures (where variation operators would have to be different). We have developed a very efficient evolutionary algorithm USPEX (Universal Structure Predictor: Evolutionary Xtallography), which requires no

experimental information (except the chemical formula) and is very efficient and reliable (no failures found in several dozen tests on different compounds, and fully *ab initio* structure predictions are routinely possible). This algorithm is discussed later in this section, for more details see [36,37]. Flexible nature of the variation operators allows one to incorporate features of other methods into an evolutionary algorithm. However, the focus is entirely on finding the global minimum – no information is yielded on structural transformation mechanisms. Therefore, our philosophy is to use metadynamics for studies of transformation pathways, and USPEX for predicting new structures.

The original ideas of metadynamics were formulated in [143] and adapted to studies of crystals by Martoňák *et al.* [34,132,133]. The idea is to start with some reasonable structure and, gradually filling the corresponding free energy minimum, induce a transformation into another structure through the lowest energy barrier and, step by step, explore the energy landscape. In this method, one introduces an order parameter – usually, the lattice vectors matrix $\mathbf{h} = (h_{11}, h_{22}, h_{33}, h_{12}, h_{13}, h_{23})$ chosen in the upper triangular form. This order parameter follows discrete evolution:

$$\mathbf{h}^{t+1} = \mathbf{h}^t + \delta h \frac{\phi^t}{|\phi^t|} , \quad (36)$$

where δh is a stepping parameter, and the driving force $\phi^t = -\frac{\partial G^t}{\partial \mathbf{h}}$ is calculated from the history-dependent Gibbs potential $G^t(\mathbf{h})$ containing Gaussians added on top of the real free energy surface $G(\mathbf{h})$:

$$G^t(\mathbf{h}) = G(\mathbf{h}) + \sum_{t' < t} W e^{-\frac{|h-h^{t'}|^2}{2\delta h^2}} , \quad (37)$$

where W is the height of the Gaussians. The derivative of the first term on the right-hand side of (37) is:

$$-\frac{\partial G}{\partial h_{ij}} = V[\mathbf{h}^{-1}(p - P)]_{ji} , \quad (38)$$

where p and P are the calculated and target pressure tensors, respectively. Pressure tensors are calculated from *NVT*-molecular dynamics simulations. To make the exploration of the free energy surface as complete as possible, it is useful to repeat simulations starting from each found structure. A scheme of metadynamics-based exploration of the energy landscape is given in Fig. 14.

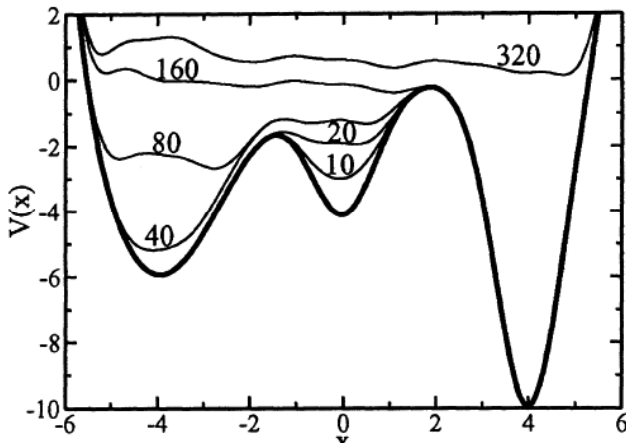


Fig. 14. Time evolution of the sum of a one-dimensional model potential $V(x)$ (thick line) and the accumulating Gaussian. The dynamics starts in the minimum in the middle, after 20 steps it goes to the left minimum and finally after 160 to the right minimum. After [143].

The method described above encounters interesting problems:

1. The reduction of all $3N+3$ degrees of freedom to just 6 is certainly a simplification, which only works because often atomic positions are strongly coupled to lattice vectors. Whenever this is not the case, this method will not be effective. This coupling becomes weak in large unit cells, and experience shows that for systems with more than 500-800 atoms (which is usually more than sufficient) in the unit cell the method produces only glassy or granular structures.
2. The free energy surface is very anisotropic in \mathbf{h} -space: in shear coordinates it has a much smaller curvature than in coordinates corresponding to volume changes. In cases of extreme anisotropy, the use of spherical Gaussians (37) causes problems, to solve which a renormalization of the order parameter components has been proposed [133]. This modified method uncovered phase transformation mechanisms in SiO_2 polymorphs under pressure (Fig. 15). By contrast, in the original formulation, starting from SiO_2 quartz only amorphisation was observed.

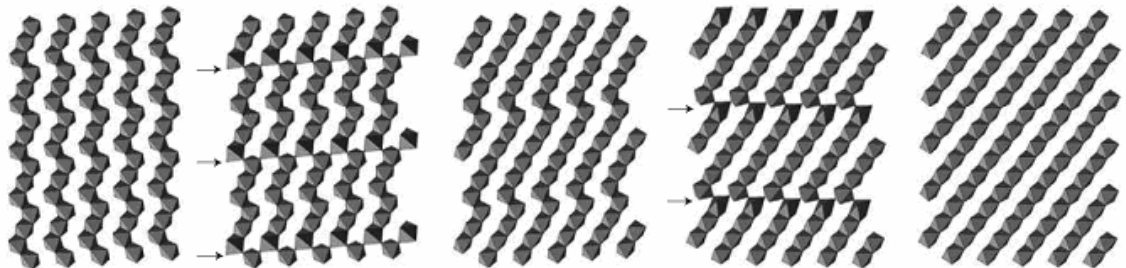


Fig. 15. Shear mechanism of structural transformations in SiO_2 under pressure. From [133].

We have also used metadynamics to uncover the mechanism of the perovskite – post-perovskite transformation mechanism in MgSiO_3 [144]. Simulations suggested the possibility of an unusual plastic deformation mechanism (Fig. 16), which we confirmed using a more direct approach based on the generalised Legrand criterion [145,144]. This mechanism, in turn, provided a new interpretation of seismic anisotropy of the D'' layer [144] and could explain its large magnitude and inclined character [146-148]. The predicted mechanism of plasticity has been subsequently confirmed experimentally [149].

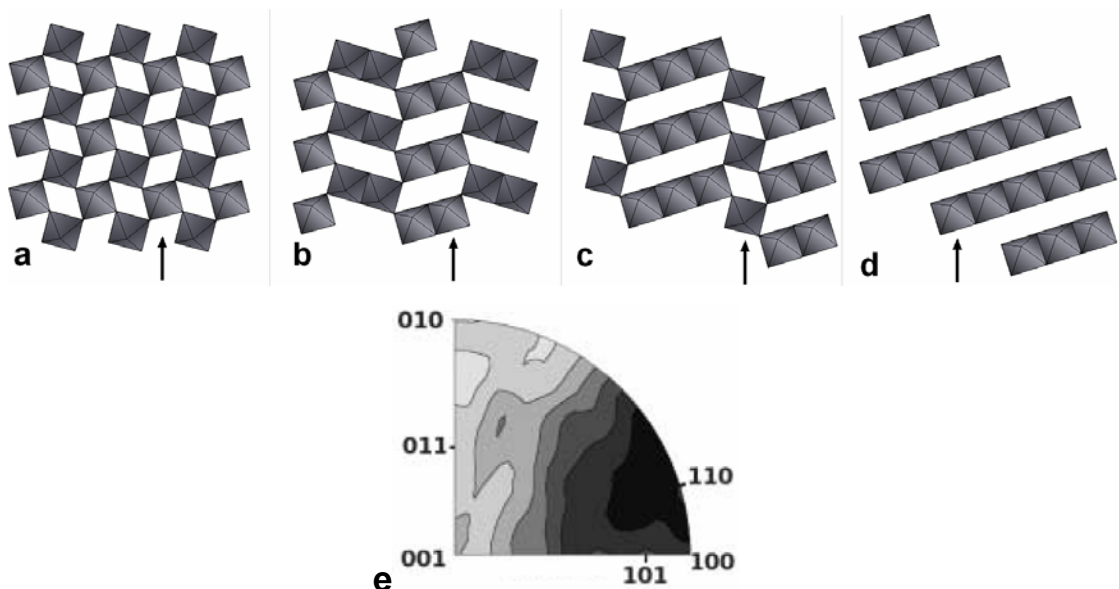


Fig. 16. Polytypism and plastic deformation of MgSiO_3 at conditions of the Earth's lower mantle. (a-d) Polytypic structures [144] (a - perovskite, b - 2x2 structure, c - 3x1 structure, d - post-perovskite), arrows show the plastic slip planes, {110} in the post-perovskite structure. **(e)** Experimental inverse pole figure showing the preferred orientation pattern in MgGeO_3 post-perovskite at 104 GPa and indicating {110} slip [149].

Let us briefly discuss the USPEX method. For our method we chose the negative of the free energy as fitness; this is usually calculated *ab initio* (we can also use parameterised interatomic potentials). This is computationally expensive but provides us with the most reliable quantification of the quality of a structure. The minimal input, besides parameters of evolution, is a guess at the unit cell volume (to which we scale new structures and which evolves over the run), pressure and number of atoms/cell. Therefore, and since we usually start from random structures, structure search is independent from experimental data. When the number of formula units

(Z) in the cell is unknown, simulations should be done for different Z (up to a reasonable maximum number).

We use the standard representation of structures – by six lattice parameters and $3N$ fractional atomic coordinates of all atoms in the unit cell. In view of the fact that small distortions of a structure often have a greater influence on the free energy than profound structural differences do (e.g., bond stretching can involve greater energy changes than a polymorphic transformation), we have decided to locally optimise every candidate structure prior to evaluating it by means of its free energy. This increases the cost of each calculated structure, but we find that this is essential for a feasible comparison of competing structures and thus for the method to work at all.

There are three variation operators within USPEX: heredity, mutation and permutation. The probability of choosing a structure to act as parent for a new structure is positively correlated to its fitness.

In heredity two individuals (i.e. structures) are selected and used to produce one new candidate. This is achieved by taking a fraction of each individual and combining these. However, the fraction of each individual should contain as much information about the individual as possible. The main information within crystal structures is the relative position of the nearby atoms. Thus, to conserve information, the fraction of an individual is selected by taking a spatially coherent slab. A slab is produced by cutting a structure at the position X (random number) of a randomly chosen lattice vector, in parallel to the plane spanned by the other two lattice vectors. One parent provides $[0+\delta, X+\delta]$, the other the slab $[X+\delta, 1+\delta]$, where δ is a random number. The two slabs are fitted together and the result thereafter made feasible by adjusting the number of atoms of each type to the requirements.

When no space group information is used, the origin of the unit cell is unimportant - only the shape of the unit cell and the relative position of atoms are of importance. Thus, to avoid biasing the position of substructures within the unit cell, we usually shift the position of the atoms with respect to the unit cell before choosing a slab. The original and the shifted structure are physically identical. Taking the weighted average of the two parent lattices, where the weight is chosen randomly, produces the new lattice.

Mutation involves random changes in the lattice and in the atomic positions. We have found, however, that mutation of atomic positions is not necessary, since local optimization takes care of exact atomic positions. Mutation of the lattice is achieved by applying a strain matrix to the lattice; the strain matrix has to be symmetric to

avoid whole-cell rotations. The strains are zero mean random Gaussian variables. Mutation of the lattice should be present for optimal performance, both to prevent a possibly premature convergence towards a certain lattice and for efficient exploration of the immediate neighbourhood of promising structures.

In permutation two atoms of different types are exchanged (as done in [140]) a variable number of times. Permutation facilitates finding the correct atomic ordering. Obviously, permutation is possible only for systems with ≥ 2 types of atoms.

The computationally expensive part of the algorithm is local optimisation. Local optimization of different candidates within one generation is independent and can thus be processed in parallel (but only within the same generation). This makes USPEX a very easily parallelisable code.

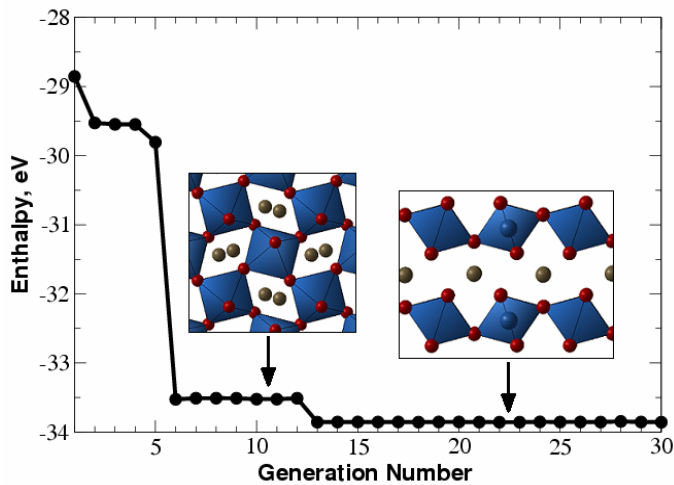


Fig. 17. Search for the stable structure of MgSiO_3 at 120 GPa using USPEX. Shown is the lowest enthalpy (per 20 atoms) in each generation (30 structures/generation). Insets show the perovskite and post-perovskite structures. From [36].

The method has been extensively tested and showed an unprecedented $\sim 100\%$ success rate for a very diverse set of test cases (for more details see [36,37]). Fig. 17,18 illustrate two of such tests. In particular, Fig. 18 shows that USPEX is vastly superior to random sampling methods. With USPEX, we have found two new stable high-pressure forms of CaCO_3 [35], as well as sulphur [36], oxygen [120], boron [119], as well as a number of interesting metastable structures [36]. Many of these structures have been confirmed experimentally and will be discussed in sections 5.4 and 5.5. An interesting metastable structure of carbon is shown in Fig. 19. This structure is ~ 0.5 eV/atom higher in energy than graphite, contains sp^2 -hybridised

carbon atoms, but has a full three-dimensional connectivity. It can in principle be synthesized and is likely to be possess high hardness (C-C bonds in this structure are much shorter than in diamond).

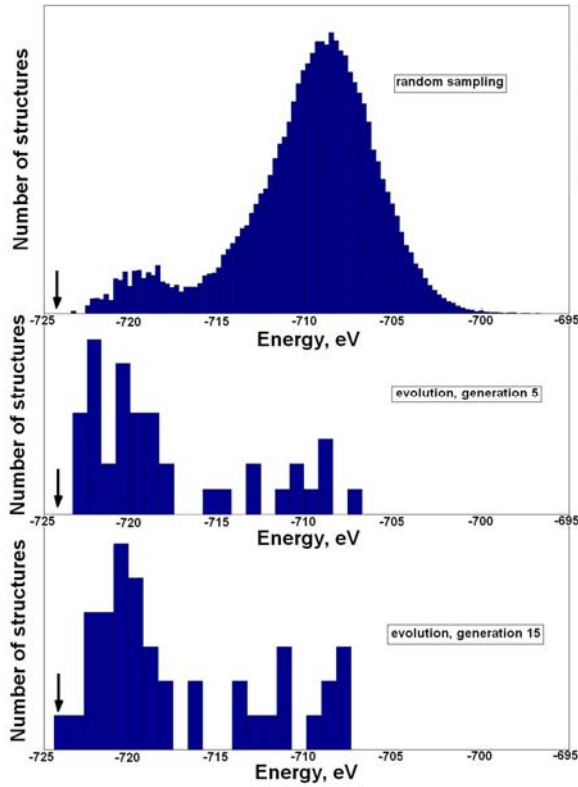


Fig. 18. Comparison of random search and USPEX. The test case is 40-atom supercell of MgSiO_3 with fixed cell parameters of post-perovskite. The distribution of energies of locally optimized structures is shown. For random sampling, 1.2×10^5 structures were generated and optimized without finding the post-perovskite structure. With USPEX this structure was found within 15 generations (with 40 structures/generation, i.e. only 600 local optimizations were needed). Arrows show the energy of the post-perovskite structure. From [150]. Movies can be seen at <http://olivine.ethz.ch/~artem/USPEX.html>.

USPEX can be used also for studying multicomponent stoichiometric systems and solid-state reactions. An interesting problem was recently posed to us by R. Hoffmann: will xenon form carbides under pressure? Pressure certainly makes Xe more reactive [9], and valence orbital energies of Xe and C are quite similar. We did simulations at 200 GPa, within the GGA [61] and taking cells with up to 14 atoms/cell. At this pressure all Xe carbides are extremely unstable (Fig. 20), but XeC_2 has a small negative volume of formation and might become stable at much higher pressures. All structures (Fig. 21) are made of close-packed Xe layers (i.e.

fragments of the elemental Xe structure) and 3,4-connected carbon layers (intermediate between graphite and diamond), except the 3D-clathrate structure of XeC_8 . The observed layering is, most likely, system size-dependent: increasing the number of atoms, we expect to see thicker elemental layers, to the point of complete phase separation. The presence of three-coordinate carbon and a clathrate structure at such high pressure can be explained by an effective negative pressure, which large Xe atoms exert on the much smaller C atoms. Some of the carbon layers are shown in Fig. 22; they are reminiscent of the low-pressure chemistry of carbon. Recently, we succeeded in predicting new stable oxides and silicates of xenon at much lower pressures (Jung *et al.*, in prep.).

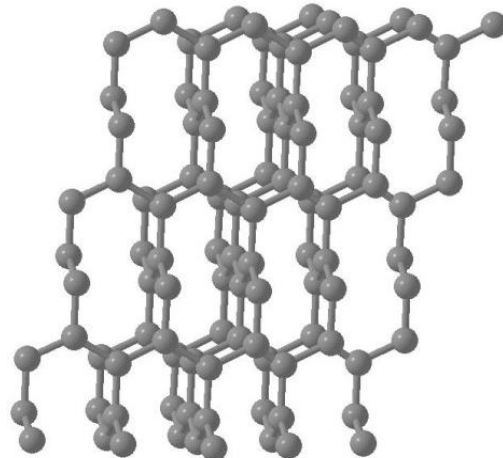


Fig. 19. Metastable structure of carbon from USPEX simulations at 1 atm [36].

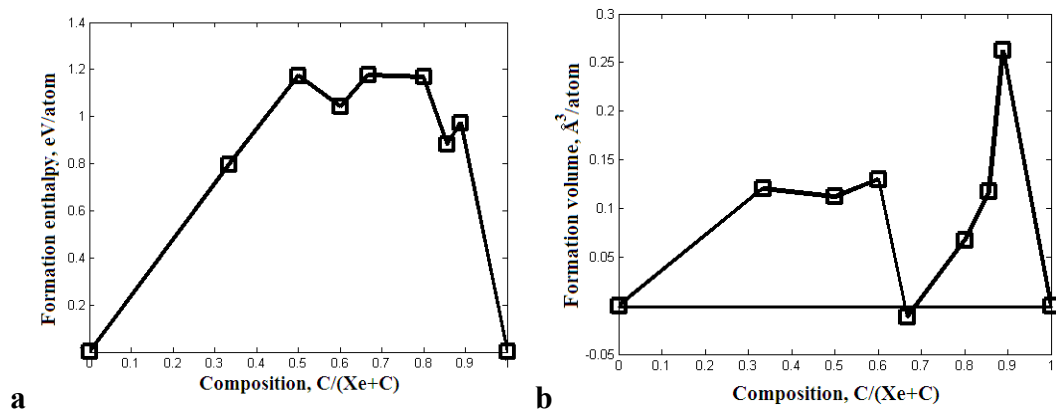


Fig. 20. Predicted enthalpy (a) and volume (b) of formation of Xe-C compounds at 200 GPa. The compounds shown are Xe (hcp), Xe_2C , XeC , Xe_2C_3 , XeC_2 , XeC_4 , XeC_6 , XeC_8 , C(diamond).

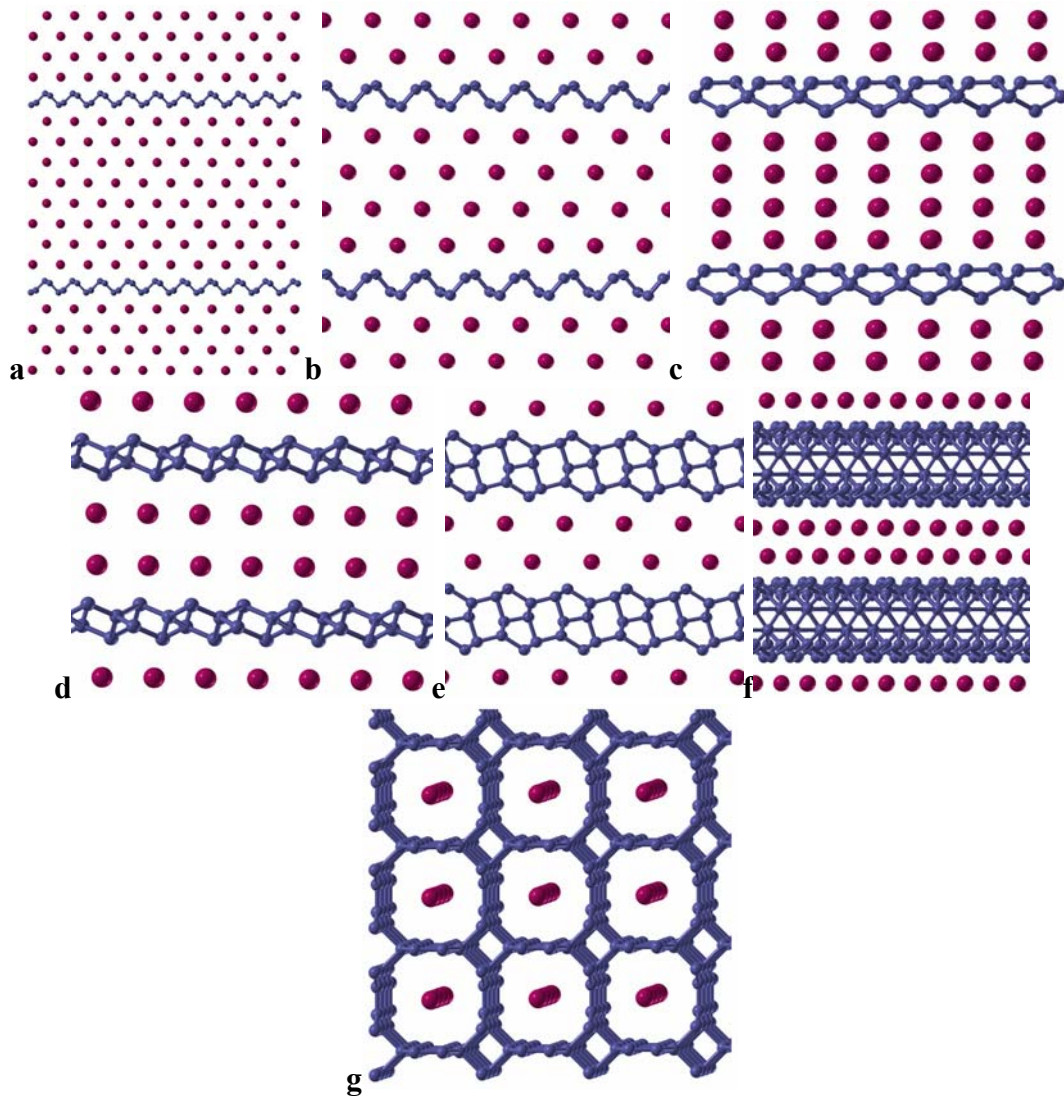


Fig. 21. Predicted structures of a) Xe_2C , b) XeC , c) Xe_2C_3 , d) XeC_2 , e) XeC_4 , f) XeC_6 , g) XeC_8 at 200 GPa.

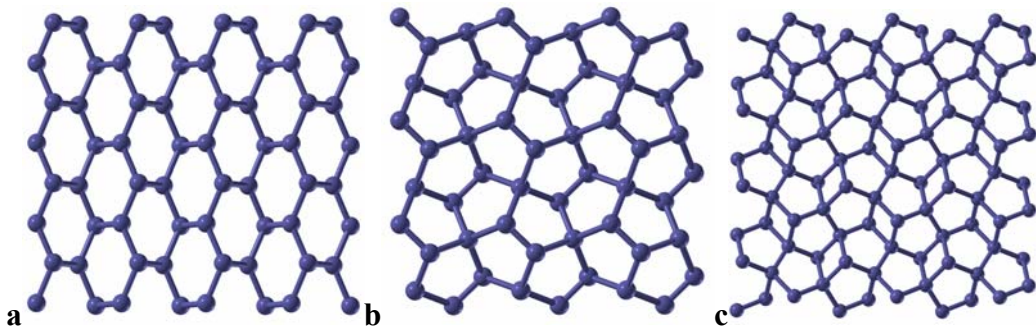


Fig. 22. Structures of carbon layers in a) Xe_2C and XeC , b) Xe_2C_3 , c) XeC_2 .

Among the future developments of USPEX, some of which are already underway, are:

- 1) Extension of the method to very large systems (currently, 100-200 atoms/cell seems to be the limit). In particular, an extension of the method to molecular crystals (handling whole molecules) has been recently achieved.

- 2) Extension of the method to yield simultaneously stable stoichiometries and the corresponding structures. Instead of a fixed composition (as is now), a set of constituent elements will be in the input. For a fixed structure, it is already possible to find optimal stoichiometries [151].
- 3) Crystal structure prediction with USPEX at the quantum Monte Carlo level. This can be important for systems, which are not well described by the existing approximations of DFT.

5. New phenomena at high pressure.

A number of excellent reviews exist in the field of high-pressure crystallography and physics (e.g., [2,4,5,13,17,152-157]), where we refer the reader for a more complete exposition of this field. One thought, coming across all these reviews, is that phenomena observed under high pressure very often do not follow simple trends and very often go against expectations. Rules of classical chemistry and crystal chemistry are very often violated under pressure.

Pressure significantly alters chemical bonding: e.g., normally inert elements Pt, Ir, Xe become chemically highly reactive, K and Rb become d-elements [158], most elements become superconductors under pressure (e.g., B, O, S) and many (e.g., Rb, Ba, Bi) develop unique and very complex structures under pressure. Many of these phenomena are poorly understood and reflect hitherto unsuspected aspects of chemical bonding. Changes of chemical bonding under pressure induce changes in the geochemical behaviour of the elements. For instance, Xe becomes chemically reactive may be retained in the mantle (explaining the “missing xenon” paradox in the atmospheric composition) [9], whereas K becomes a d-element and may alloy with Fe in the core [5] – enabling radiogenic heat production within the core.

Part of the reason behind these complexities is that under high pressure (unlike at $P=0$), the stable state is determined not just by the internal energy, but by the competition between the E (or F) and the PV terms in the free energy (1). Therefore, the rules of chemistry (which have been formulated at $P = 1 \text{ atm} \approx 0$) are dictated solely by the energy factor and can become invalid under very high pressures, where the PV term becomes dominant. Furthermore, competing factors are a well-known cause of complexity in physical systems – therefore, the competition between E and PV is likely to create complex behaviour. Some of these complex phenomena will be discussed below. We also consider several new high-pressure mineral phases, which extend our understanding of planetary interiors.

5.1. Quantum melting and pressure-induced amorphisation.

The relationship between structural order and stability plays a fundamental role in crystallography. Minimisation of the Gibbs free energy (1) at high temperatures enables stability of high-entropy (i.e. disordered) phases. At low temperatures, the state with the lowest internal energy E (or, at finite pressure, the enthalpy $H=E+PV$) is stable. There is no guarantee, however, that this will be an ordered, periodic (or

even solid) state. In fact, quantum nuclear motion makes it possible for quantum liquids to be stable at $T = 0$ K. This can happen when the mean-square displacements $\langle x^2 \rangle$ of the atoms at $T = 0$ K become comparable to the nearest-neighbour distance a ; according to the Lindemann criterion melting occurs when $\langle x^2 \rangle > 0.1a$. Combining this with a simple Einstein model, where all atoms vibrate independently with the frequency ω , we derive a simple criterion of quantum melting at $T = 0$ K:

$$\frac{\hbar}{2M\omega} > 0.1a , \quad (39)$$

where M is the atomic mass. From (39), it is obvious that weak interatomic potentials and low atomic masses are the necessary prerequisites of quantum melting. Under pressure, the right-hand side of (39) decreases, and if the left-hand side increases enough, quantum melting may be observed. For He, the left-hand side of (39) increases with pressure, and He (which is a quantum liquid at 1 atm) crystallises under pressure. Hydrogen is a good candidate for quantum melting under pressure: it is believed to transform to a non-molecular phase at around 500 GPa [152,159], which corresponds to softening of H-H potentials and the possibility of quantum melting. This quantum fluid would be an unusual two-component quantum fluid made of electrons and protons [160]. Indeed, it was predicted [161] using *ab initio* molecular dynamics that the melting curve of hydrogen has a negative slope at >100 GPa, and may reach zero Kelvin at sufficiently high pressures (Fig. 23). Of course, once a non-molecular quantum liquid is formed, its vibrational frequencies ω will increase with pressure, making the quantum liquid eventually crystallize at some higher pressure.

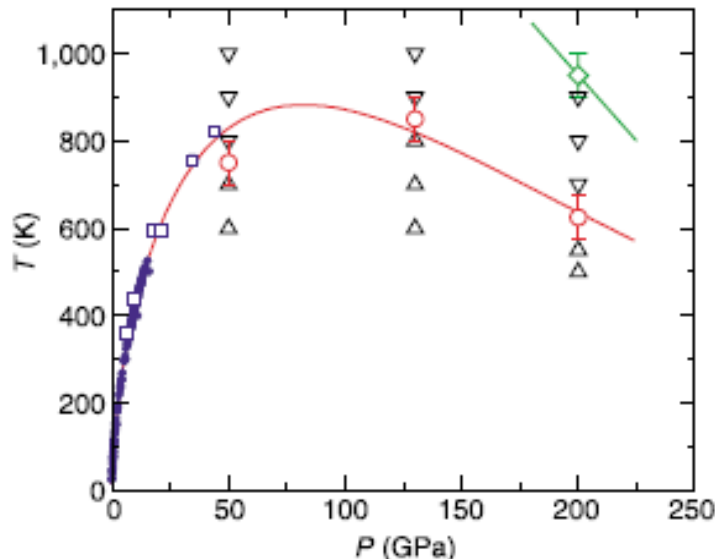


Fig. 23. Melting curve of hydrogen. From [161].

It is not known whether disordered solids can be stable at $T = 0$ K, but they certainly can be metastable. Pressure-induced amorphisation gives an interesting example of a (non-quantum) breakdown of order under pressure; however, in all known cases it is metastable. This phenomenon was discovered in experiments on compression of ice which, compressed to 1 GPa at 77 K, did not transform to the modification stable at these conditions (ice VI), but was found to amorphise [162]. Later it was observed in many systems – see detailed reviews [163,164].

Pressure-induced amorphisation is a first order transition. Structural relationships between melting-and-cooling-produced amorphous phases and pressure-induced ones have been widely discussed, but in general the similarity is not required.

Mechanisms driving pressure-induced amorphisation are still not quite clear. The necessary conditions are: 1) Higher density of the amorphous phase compared to the crystalline one. This implies that crystals with open structures are more prone to amorphisation than close-packed ones and that usually coordination numbers will increase upon amorphisation; 2) Presence of soft modes in the crystalline phase. Softening of a vibrational mode at a single point of the Brillouin zone should drive a transition to a periodic (if the soft wavevector is rational) or incommensurate (if the wavevector is irrational) phase. Only simultaneous or nearly simultaneous softening of a phonon branch at a range of \mathbf{k} -vectors (e.g., along a certain direction of the Brillouin zone) can produce an amorphous phase [165-167]. Using lattice dynamics calculations, we have predicted pressure-induced amorphisation in Al_2SiO_5 andalusite [168]. This implies weak dispersion of this branch, which is most naturally achieved when the unit cell is large. Indeed, crystals with complicated structures and large unit cells are more prone to pressure-induced amorphisation.

5.2. Breakdown of close packing under pressure.

Close-packed structures (fcc, hcp,...) possess the highest mathematically possible density of packing of identical spheres: 74%. This is why it was (and still is) believed that close-packed structures will be commonly attained by all materials under high compression. However, experimental facts often contradict this expectation. Ironically, while at moderate pressures close packings do appear often, upon further compression they often disappear. This betrays the inadequacy of the assumptions made, namely:

1. Spherical atoms: the actual shape of the electron density around nuclei in crystals deviates from spherical. For non-spherical objects, there are more efficient

ways of packing than fcc or hcp. The shape of the oxygen atom in oxides and silicates is strongly aspherical (Fig. 24), which leads to the breakdown of close packing in many of such compounds. E.g., the low-pressure phase of MgSiO_3 (enstatite) has a distorted close packing of the O^{2-} ions, which becomes nearly perfect in the ilmenite-structured akimotoite (stable at 20-30 GPa). On further compression, MgSiO_3 perovskite becomes stable, its structure contains a distorted cubic close packing of the O^{2-} and Mg^{2+} ions. Above 100 GPa, the post-perovskite phase is stable, and its structure does not contain any close packing. Similar breakdown of close packing under pressure occurs in SiO_2 [3] and Al_2O_3 [115]. For SiO_2 , the sequence of phases quartz \rightarrow coesite \rightarrow stishovite \rightarrow CaCl_2 -type \rightarrow α - PbO_2 -type does involve the tendency to anionic close packing (as well as increase of the coordination number from 4 to 6), but the pyrite structure stable above 200 GPa does not have anionic close packing (Fig. 25). Above 750 GPa, a non-close-packed cotunnite-type phase is formed [3].

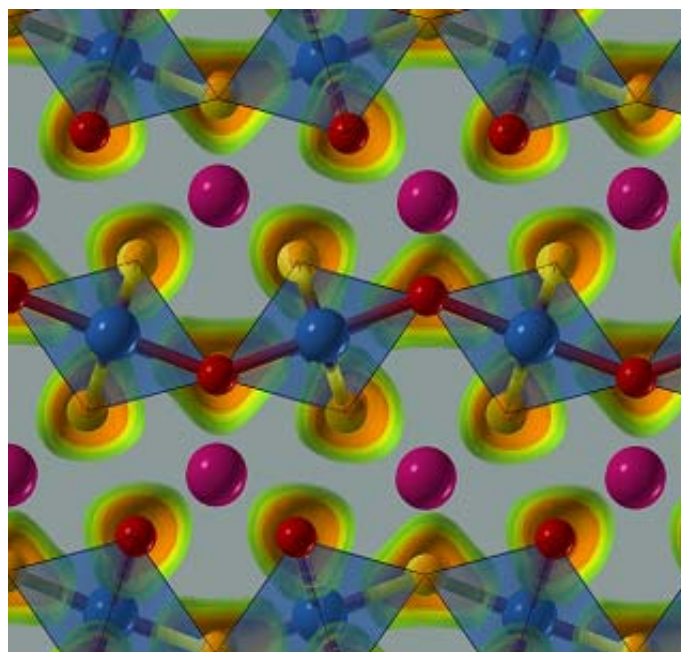


Fig. 24. Localised orbital locator (LOL) [169] in the structure of MgSiO_3 post-perovskite. Notice the clear asphericity of the distribution around the oxygen atoms, where LOL maxima are situated.

2. Equivalence of the spheres: this assumption is correct for the elements (though not always even there!), but is severe for compounds. While often one focuses on the largest atom and its close packing in a compound structure, under pressure the ratios of atomic sizes change and multicomponent packings will have to be considered. For packings of spheres of different sizes, fcc- and hcp-based

structures may not be the densest. E.g., in SiO_2 large O^{2-} anions are more compressible than small Si^{4+} cations, and at ultrahigh pressures Si^{4+} will become comparable in size with the anions and require high coordination incompatible with close packing; at this point (at 750 GPa – [3]) the cotunnite structure (with 9-fold coordination of Si) is formed. An analogous situation occurs in Al_2O_3 at 130 GPa, when it transforms into an CaIrO_3 -type phase [115,125] with half of the Al atoms in the 8-fold coordination. This coordination is also incompatible with close packing.

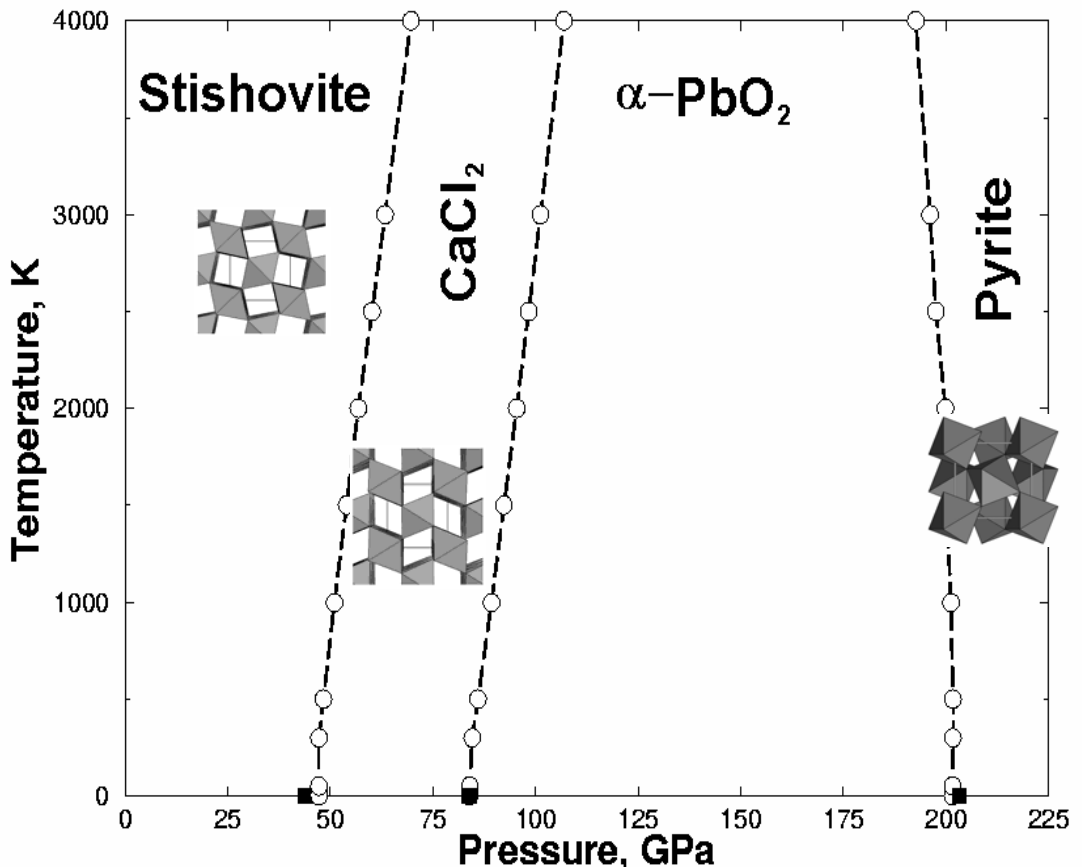


Fig. 25. High-pressure phase diagram of SiO_2 [3]: anion close packing disappears at > 200 GPa. Phases stable below 10 GPa and the poorly known melting curve are omitted for clarity.

3. Constancy of atomic sizes: first, atomic radii are known to depend strongly on the electronic structure of the atom. Spin transitions or $s \rightarrow d$ electronic transitions can greatly change the size of the atom. For example, for Rb, non-close-packed structures with $4d^1$ valence configuration of the atom may be denser than close-packed structures with the $5s^2$ valence configuration and exotic complex structures are actually formed in all alkali metals under pressure [121], see Fig. 26.

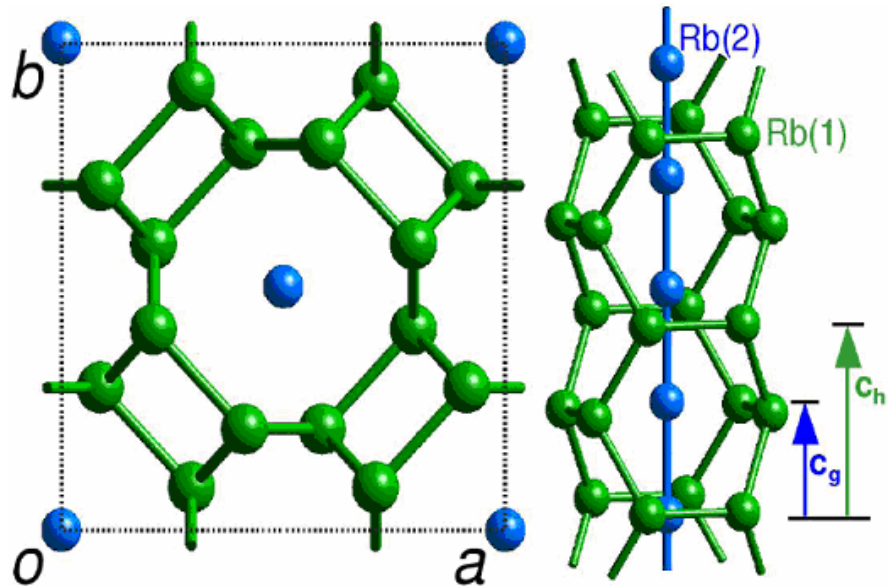


Fig. 26. Two views of the Rb-IV structure at 17.2 GPa. This structure [170] consists of two sublattices (“guest” and “host”), the figure is from [157].

Furthermore, even in the absence of electronic transitions, atomic sizes and bond lengths R are very well known to depend on the coordination number [171]:

$$R = R_0 + b \ln \nu , \quad (40)$$

where R and R_0 are expressed in Å, R_0 is a bond-specific parameter, $b=0.37$ Å, and ν is the coordination number. Thus, atoms in the bcc structure are smaller than in the fcc structure, which often renders the bcc structure denser. Using (40), the ratio of specific volumes in the fcc and bcc structures at 1 atm is:

$$\frac{V_{bcc}}{V_{fcc}} = \frac{f_{bcc}}{f_{fcc}} \left(\frac{R_{bcc} + b \ln(8/12)}{R_{fcc}} \right)^3 , \quad (41)$$

where f are packing densities (0.74 for fcc and 0.68 for bcc), and R_{fcc} is bond length in the fcc structure. This expression does indeed show that in very many cases the bcc structure will be denser than fcc or hcp at 1 atm, and therefore can become more stable under pressure. Indeed, Mg undergoes an hcp-bcc transition at ~50 GPa [2], and Ca has an fcc-bcc transition at 20 GPa [4]. Eq. (41) is valid only at 1 atm, and can only be used for extrapolations in moderate pressure ranges.

5.3. Metallisation and demetallisation.

While all materials must metallise at sufficiently high pressure, two issues are of interest – 1) the actual pressure of metallisation and its mechanism, 2) the evolution of the atomic and electronic structure prior to metallisation.

The highest known metallisation pressure was predicted for solid Ne – 158 TPa [173] or 134 TPa [174]. MgO, which is isoelectronic with Ne, was predicted [113] to metallise (by band overlap) above 21 TPa. The valence electron density distributions (Fig. 27) show that even in the metallic phase most valence electrons reside on the O atom. The main difference is that the electron densities of the neighbouring O atoms overlap, enabling electron transport. We note that, in spite of the clear localisation of valence electrons on the O atoms (Fig. 27), screening of ionic potentials is very effective in metals, and the notion of atomic charges in metals becomes meaningless.

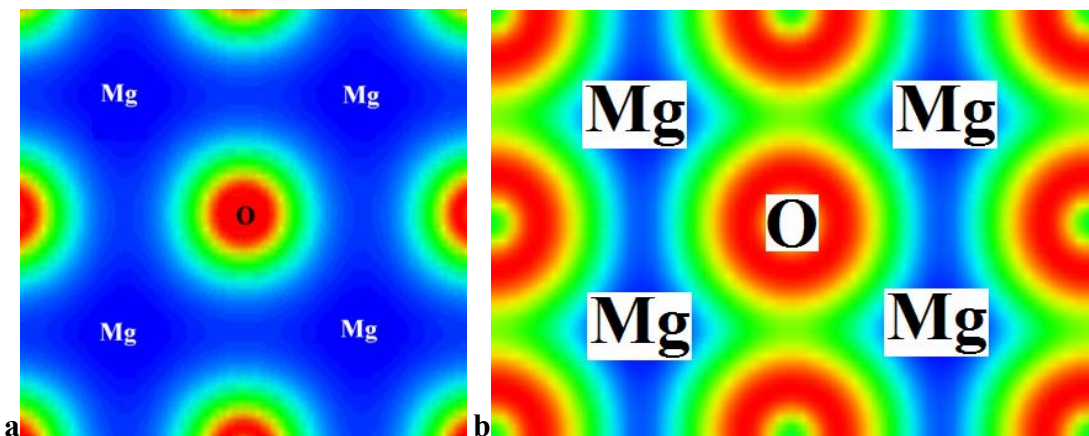


Fig. 27. Valence electron density in MgO: a) ionic NaCl-type structure at 1 atm, b) metallic CsCl-type structure at > 21 TPa.

The ultimate state of compressed matter (ignoring, for now, the processes of electron capture by the nuclei – ultimately leading to the formation of neutron stars) is the free-electron metal. However, to reach this state one needs to „crush“ the atomic orbitals, which requires pressures well above 1 a.u. (29.4 TPa). *En route* to this state, a number of interesting phenomena occur. Often, newly metallised materials exhibit superconductivity (which is not possible in the free-electron gas), but at some pressure superconductivity will be suppressed. In some cases pressure may induce an opposite phenomenon – demetallisation, where an initially metallic phase becomes insulating in a limited pressure range.

Oxygen gives an interesting case of metallisation by band overlap [120]. Low-pressure α - β - γ - δ - phases are magnetic, but magnetism collapses at 8 GPa when the ϵ -phase is formed. The structure of the ϵ -phase was mysterious for a long time, and was solved only recently [176,177] and shown to contain O_8 clusters made of four O_2 molecules (Fig. 28). The formation of this structure is closely related to the magnetic collapse: before magnetic collapse, each O_2 molecule had two unpaired electrons. After collapse, in the ϵ -phase, both are paired with the electrons of the neighbouring

molecules – hence, each molecule has two neighbouring molecules. Metallisation occurs at 96 GPa with the formation of the ζ -phase [178], which is known to be superconducting [179], but structure of which was solved only recently [120] using the USPEX method. The structure of the ζ -phase is similar to that of the ϵ -phase, but the transition is weakly first-order and in the new structure the distances d_2 (Fig. 28) between the O_8 groups become shorter than the d_1 distances within the O_8 groups. This is in line with expectations, because structures containing clusters or molecules cannot be dense. Nevertheless, USPEX calculations show that the ζ -phase (not containing the O_8 clusters, but still molecular with distinct O_2 molecules) has a very wide stability field and O_2 molecules are present in oxygen at least up to 500 GPa. Fig. 29 shows the band structure of the ϵ - and ζ -phases.

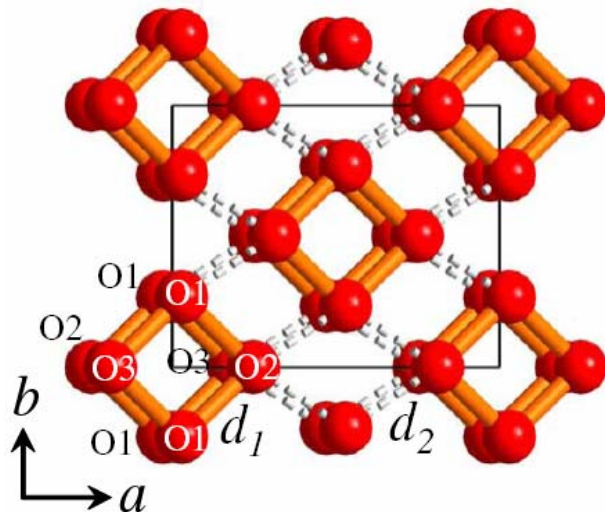


Fig. 28. Crystal structure of ϵ -O₈. From [177].

Demetallisation under pressure has been predicted for Ca in a limited pressure range [13]. Even though both valence and conduction bands broaden under pressure (as is generally expected), the band gap opens. In this case this occurs, because the gap is indirect (W-L points in the Brillouin zone), and the occupied-unoccupied level splitting at the L-point increases with pressure to avoid level crossing (Fig. 31). At higher compressions Ca was predicted to metallise again (Fig. 30) [13], and a non-monotonic pressure dependence of electrical resistivity is indeed known for this metal (see [13] and references therein). Ca exhibits a very interesting sequence of phase transitions under pressure, which is discussed in the next section.

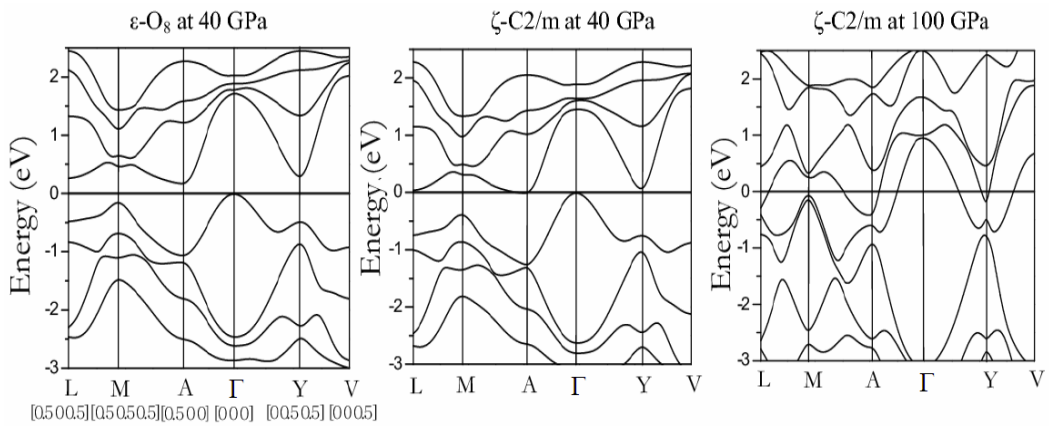


Fig. 29. Band structure of the ϵ - and ζ - phases of oxygen. From [120].

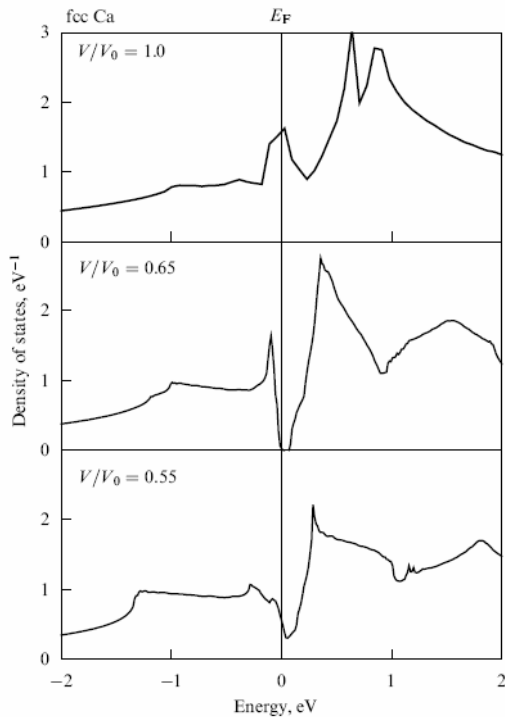


Fig. 30. Calculated electronic densities of state of the fcc phase of Ca at a series of volumes. From [13].

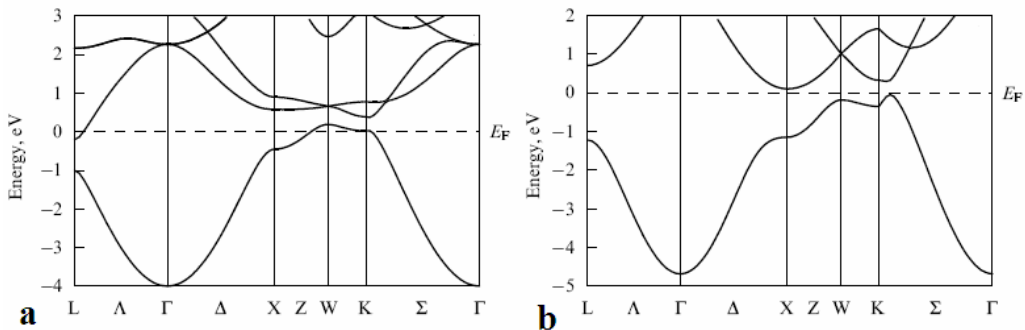


Fig. 31. Calculated band structure of fcc-Ca a) at normal volume V_0 , b) at $0.6V_0$.
From [13].

5.4. Unusual behaviour of the elements under pressure.

Using the USPEX method, my group is actively exploring the behaviour of the elements under pressure. Several results have been published already [36]. Referring the reader to excellent reviews of this field [4,13,154-157], here we focus on two issues – 1) occupation of orbitals with higher angular momentum in elements under pressure (e.g., $s \rightarrow p$ or $s \rightarrow d$ transitions), 2) the possibility of existence of ionic phases of the elements. These phenomena will be illustrated on a few examples.

It is well known that, generally, normally unoccupied higher- l orbitals become populated under pressure. This effect reflects the modification of the orbital energies under pressure [13]. Among the examples are the $s \rightarrow p$ transition in Li, and $s \rightarrow d$ transitions in K, Rb, Cs, Ca, Sr, Ba. Fig. 32 illustrates this process and how it affects the topology of electron density distribution. Surprisingly, d-orbitals are significantly populated in many of these metals already at $P=0$ – Fig. 33, which this is shown for Ca. Fig. 34 shows an unusual distribution of the valence electron localisation function (ELF) in fcc-Ca at 1 atm: it has maxima not only at atomic positions, but also in the octahedral voids between them (thus, ELF maxima form a NaCl-type structure).

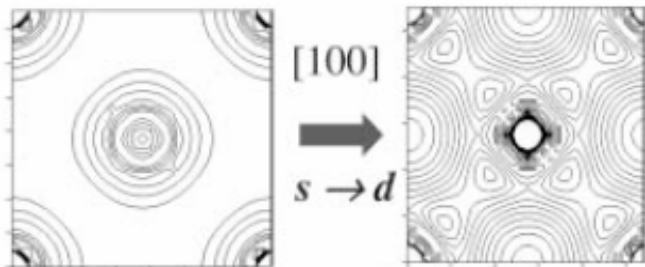


Fig. 32. Modification of valence electron density distribution in fcc-Cs as a result of $s \rightarrow d$ transition From [154].

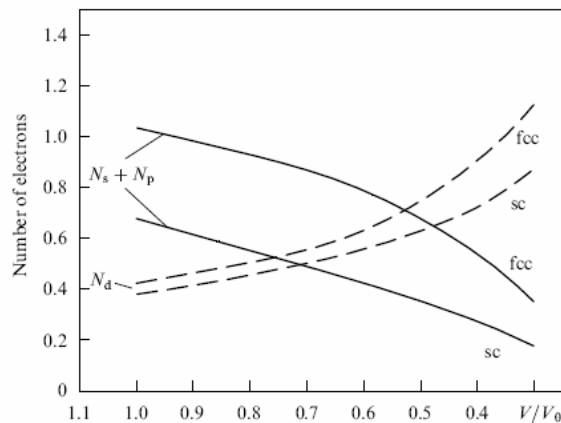


Fig. 33. Orbital populations in fcc and simple cubic (sc) phases of Ca as a function of compression. From [13]. See [121] for similar graphs on alkali metals.

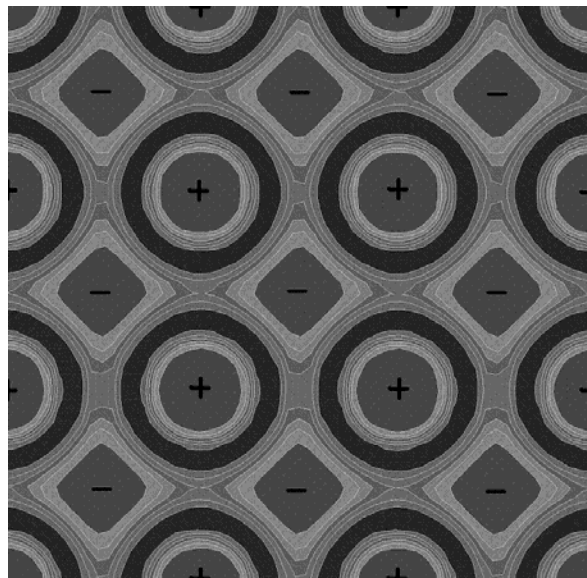


Fig. 34. Valence electron localization function (ELF: [180]) in face-centred cubic (fcc) structure of Ca at 1 atm. Signs “+” denote positions of Ca atoms, “-“ indicate interstitial maxima of ELF. Contour levels from 0.05 to 0.73.

High-pressure behaviour of Ca is extremely interesting. According to experimental studies [181,182], the fcc phase transforms into the bcc structure at 20 GPa; at 32 GPa, a simple cubic (sc) structure is formed and remains stable up to 113 GPa, above which two phases with unknown structures have been found (at 113-139 GPa and at >139 GPa, respectively) [182]. All phases above 32 GPa are superconducting, with T_C increasing with pressure and reaching 25 K at the pressure of 161 GPa [183]; this is the highest T_C detected in an element so far. The structures of the two phases found above 119 GPa are unknown and likely to be complicated [4], we are currently investigating these structures. Surprisingly, even the sc-phase turned out to be not so simple. In fact, Olijnyk and Holzapfel [181] observed some reflections additional to what should be expected for a sc-structure, but this was not confirmed by later studies [182]. Y.-M. Ma and colleagues, trying to explore electron-phonon coupling in the sc-phase, found that it is dynamically unstable. We have explored the possibility of other structures using USPEX (Oganov *et al.*, in prep.) and found another structure to be stable, with space group $I4_1/amd$; it can be described as a distorted sc-structure (Fig. 35). Latest experiments (Q. Gu, pers. comm.) confirm this prediction. At 40 GPa, our GGA-PAW calculations show that the $I4_1/amd$ phase is slightly (0.9%) less dense than the sc-structure, but is significantly (52 meV/atom) more favourable. The coordination of Ca atoms is octahedral (as in sc-phase), but distorted - with 4 nearest neighbours are at the

distance of 2.68 Å, and 2 neighbours at 2.77 Å (Fig. 35); this distortion can be ascribed to the Jahn-Teller mechanism.

Note that this structure appears when the d-population is close to 1; d¹ configuration is known to produce the Jahn-Teller distortion. In fact, the Jahn-Teller distortion to a large extent explains the observed structural complexities in the elements undergoing s→d transition under pressure. This concept can be used not only to rationalise, but also to predict such new complex structures and conditions of their appearance. To our knowledge, however, the concept of the Jahn-Teller distortion has never been applied in this field.

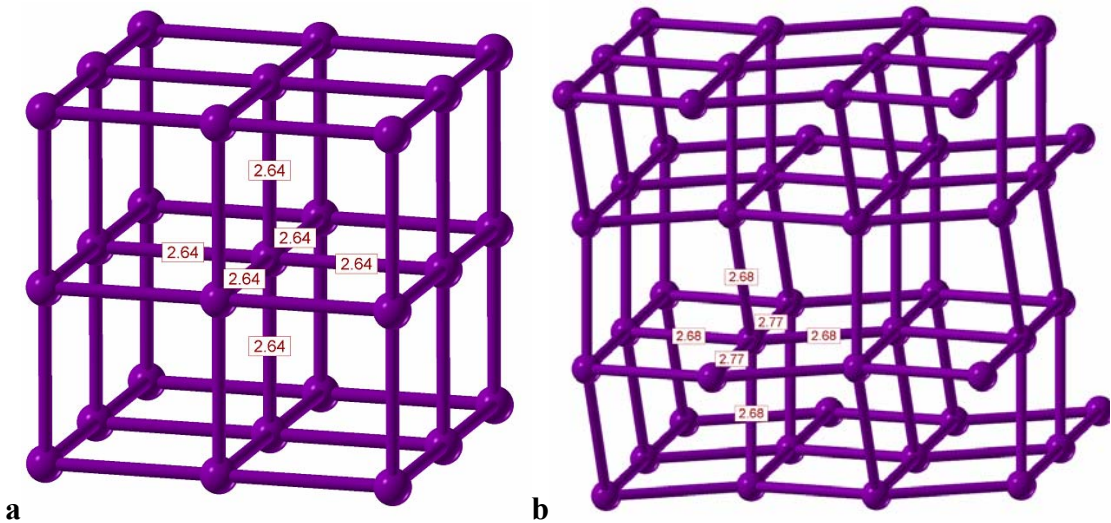


Fig. 35. Structures of a) simple cubic, b) tetragonal distortion (*I*4₁/amd) of the simple cubic structure for Ca at 40 GPa. The *I*4₁/amd structure is significantly more favourable (Oganov *et al.*, work in progress). Bond lengths are indicated.

A peculiar phenomenon of autoionization was found in boron under pressure [119]. Using *ab initio* calculations, Edwards and Ashcroft predicted that autoionization (with H⁺H⁻ molecules) is possible in hydrogen under pressure [186] – but this still has not been verified. For boron we have both experimental and theoretical data supporting autoionisation.

A new phase of boron was synthesised by J. Chen and Y.-Z. Ma at 10 GPa at 2280 K, it was found to be quenchable to ambient conditions. The diffraction pattern of the recovered sample could be indexed with an orthorhombic cell with parameters $a=5.0544$ Å, $b=5.6199$ Å, $c=6.9873$ Å, but the structure could not be solved purely from experimental data. We estimated that the number of atoms in the cell should be between 24-32 and should be even (to remain non-metallic). Thus, we performed USPEX simulations with the experimental cell and 24, 26, 28, 30 and 32 atoms/cell.

The predicted optimal structures for these numbers of atoms are shown in Fig. 36 and 37a, the optimal solution corresponds to 28 atoms/cell and is depicted in Fig 37a. As can be seen in Fig. 37b, its diffraction pattern is in good agreement with experiment. The relaxed cell parameters are $a=5.043 \text{ \AA}$, $b=5.612 \text{ \AA}$, $c=6.921 \text{ \AA}$ – an excellent match with experiment. We have shown that this structure possesses the lowest enthalpy among all known or hypothetical structures of boron in the pressure range 19-89 GPa and 0 K [119], which is a strong indication of its thermodynamic stability. We have named this phase γ -B [119].

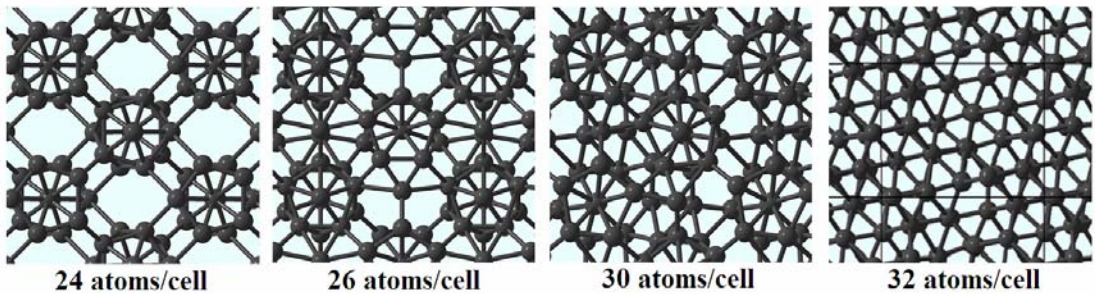


Fig. 36. Structures of boron obtained with USPEX at experimental cell parameters and 24-32 atoms/cell.

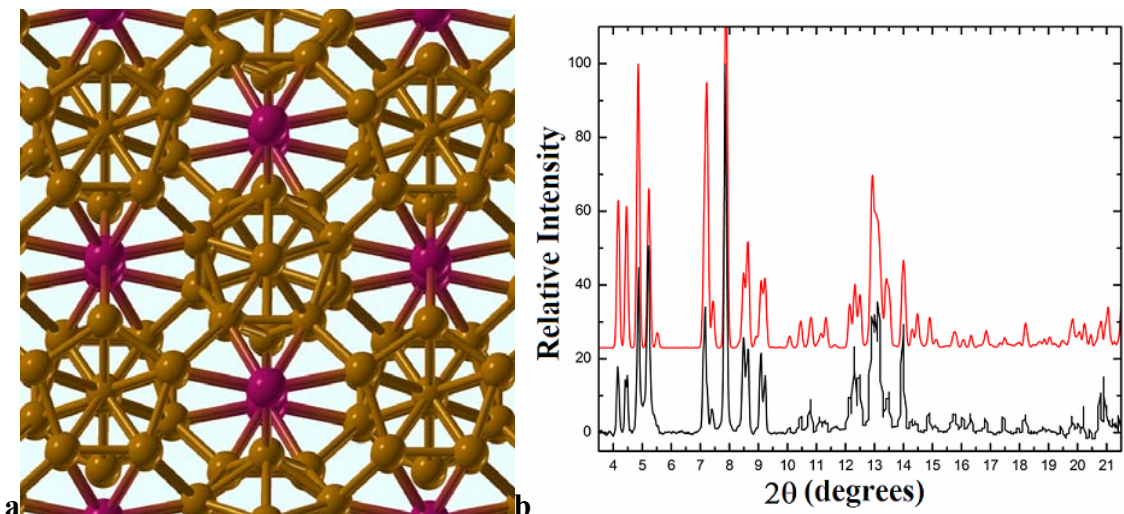


Fig. 37. γ -B: a) crystal structure (space group $Pnnm$), b) theoretical powder diffraction pattern (top) versus experimental one (bottom). From [119].

The structure of γ -B consists of B_{12} icosahedra and B_2 pairs alternating in a NaCl-type arrangement. This peculiar structure suggested to us the possibility of charge transfer between the B_{12} and B_2 groups, leading to the formation of ionic boron boride $(B_2)^{\delta+}(B_{12})^{\delta-}$. The exact values of the atomic charges are definition-dependent, but all definitions that we used give a qualitatively consistent picture: $\delta=+2.2$ from

spherically-averaged Born dynamical charges; $\delta \sim +0.2$ from differences in the numbers of electrons within atom-centred spheres (sphere radii 0.7-1.0 Å), or $\delta = +0.54$ (our preferred estimate) using Bader theory [184]. Such autoionization should leave an experimentally detectable fingerprint - strong infrared absorption at frequencies 335 cm^{-1} , 473 cm^{-1} , 757 cm^{-1} , 776 cm^{-1} , 796 cm^{-1} , 865 cm^{-1} ; its experimental investigation is currently underway.

While broken-symmetry structures, with two sublattices of the same element in different chemical roles, are known for some metals (e.g. self-hosting structures of Rb – Fig. 26), γ -B is quite different. It is non-metallic (and therefore can be ionic) and its two sublattices are occupied not by single atoms but by clusters (B_{12} and B_2). The B_{12} icosahedra are typical of boron chemistry and are the basis of all known structures of boron polymorphs, B_2 pairs are also quite frequent in boron compounds [185]. The presence of the B_2 pairs in the structure of γ -B increases the density: without these pairs, the structure will be similar to the less dense α -B. It is the difference in the properties of the B_{12} and B_2 units, which makes the structure ionic).

Ionicity affects the properties of γ -B: high-frequency and static dielectric constants are very different (11.4 and 13.2, respectively), as in all ionic crystals. Despite a structural relationship with α -B, the electronic structure of ionic γ -B is quite different: it shows little pressure dependence of the band gap and even at 200 GPa remains an insulator with a relatively wide (1.25 eV) gap, whereas for the covalent α -B the calculated band gap rapidly decreases on compression and closes at 130 GPa.

Three conditions are necessary for an ionic elemental structure: (i) insulating character (in metals, conduction electrons efficiently screen any ionic charges), (ii) broken symmetry, (iii) “intermediate” chemical properties of the atom: amphotermism and/or ability to form clusters with different electronic structure. From these criteria, H and elements close to the Zintl line (B-Si-As-Te-At) in the Periodic Table are the prime candidates for producing new ionic forms of the elements.

5.5. New mineral phases in planetary interiors.

A schematic representation of major minerals and their proportion in different parts of the Earth’s mantle is shown in Fig. 38. For a review of mantle mineralogy, see [187]. Our focus here will be on the Earth’s lower mantle, which makes ~53 vol.% of the planet. The scheme depicted in Fig. 38 shows that, except spin

transitions of $\text{Fe}^{2+}/\text{Fe}^{3+}$ ions in $(\text{Mg},\text{Fe})\text{SiO}_3$ and $(\text{Mg},\text{Fe})\text{O}$ (which are continuous at mantle temperatures and thus invisible) and the post-perovskite transition in $(\text{Mg},\text{Fe})\text{SiO}_3$, no phase transformations in major mantle-forming minerals are known in the pressure range of the lower mantle. All the more interesting therefore is that a number of (rather weak) seismic discontinuities have been detected within the lower mantle [189,190]. There is a possibility of hitherto undetected phase transitions or chemical reactions in the mantle, which would explain these discontinuities. Recently, a phase transition of MgSiO_3 perovskite to another perovskite-type phase was suggested on the basis of an extra X-ray reflection appearing under pressure [190]; however, this was later [10,11] shown to be due to the high-pressure formation of PtC as a product of reaction between Pt (laser absorber in experiments) and diamond anvils.

Nevertheless, a real phase transition of MgSiO_3 perovskite to a post-perovskite phase was found at P - T conditions corresponding to those of the D'' discontinuity (2650-2890 km depths)— see Fig. 39. This phase was independently discovered in [11,126] and confirmed by numerous studies. The post-perovskite phase of MgSiO_3 and its unusual properties explain the numerous anomalies observed by geophysicists in the D'' layer. Its positive Clapeyron slope implies that 1) the D'' layer grows with time, as the Earth cools down, 2) that if the D'' layer is chemically similar to the rest of the mantle, it should participate in whole-mantle convection and increase heat flow from the core into the mantle. Stability conditions of post-perovskite imply that the D'' layer is absent on smaller planets (Mercury, Mars, possibly Venus).

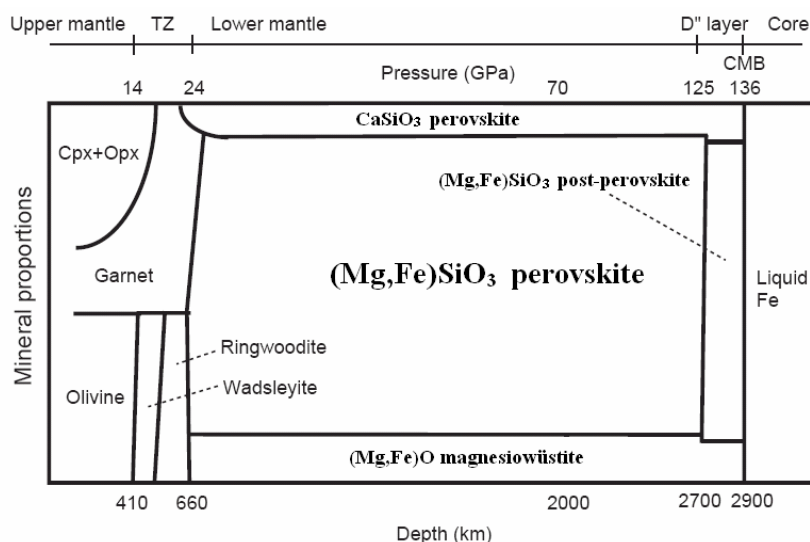


Fig. 38. Schematic phase relations in pyrolite mantle (adapted from [18]). “Cpx” and “Opx” denote ortho- and clinopyroxene, respectively.

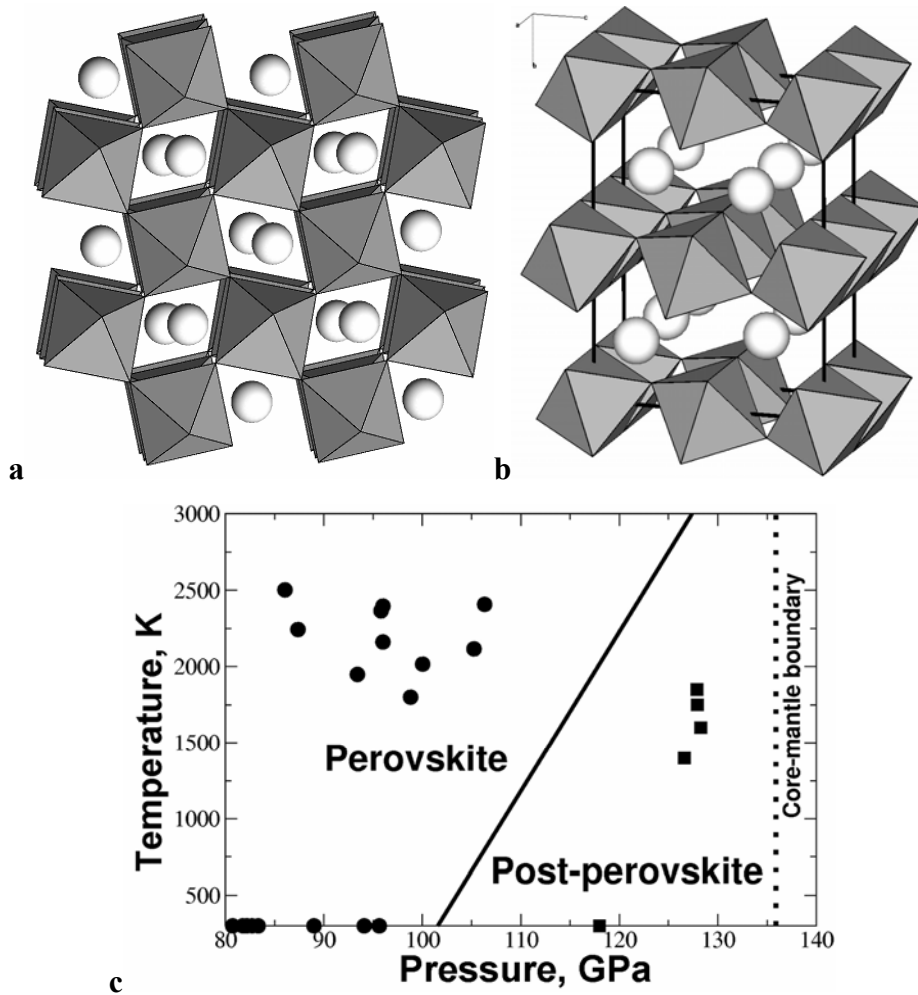


Fig. 39. High-pressure MgSiO_3 polymorphs: a) perovskite, b) post-perovskite, c) phase diagram, showing the perovskite-post-perovskite boundary. Line – theoretical phase boundary, circles and squares – experimental points where perovskite and post-perovskite, respectively, are stable. From [11].

Similar phase was found to be stable for Al_2O_3 above 130 GPa [115,125], i.e. at conditions where shock-wave experiments [191] observed a decrease of electrical resistivity. This likely implies that Al_2O_3 “post-perovskite” is a relatively good ionic conductor. If MgSiO_3 post-perovskite has a high electrical conductivity, it would explain the geophysically inferred high conductivity values in deep mantle [192], and (through coupling between the magnetic field and electrically conducting base of the mantle) the observed decadal variations of the length of day (for details see [192]).

In [144] we found that perovskite and post-perovskite structures are end members of a polytypic series of structures (see Fig. 16). As Fig. 40 shows, the intermediate polytypes are only marginally metastable at $T=0$ K and can be stabilized by impurities and temperature in the mantle. Indeed, such structures have been detected

experimentally for alumina-bearing MgSiO₃ (O. Tschauner, pers. comm.) and can be present as individual mantle-forming mineral phases.

Umemoto *et al.* [193] proposed that MgSiO₃ post-perovskite decomposes into MgO + SiO₂ at pressures above ~1 TPa. This implies a seismic discontinuity inside rocky cores of some giant planets.

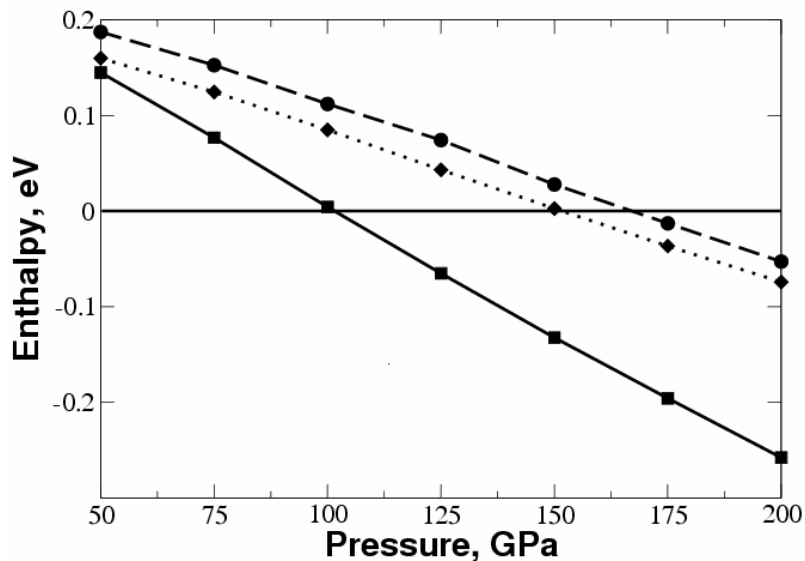


Fig. 40. Enthalpies of MgSiO₃ polytypes, per formula unit and relative to perovskite. Lines: solid – post-perovskite, dotted – 3x1 structure, dashed – 2x2 structure. These structures are shown in Fig. 16 of this thesis. From [144].

One of other most unexpected additions to the inventory of lower-mantle minerals is iron. Frost *et al.* [194] found that, while iron impurities are mainly Fe²⁺ in upper-mantle minerals, in the lower mantle valence disproportionation occurs, leading to the coexistence of metallic Fe and Fe³⁺ impurities in alumina-bearing MgSiO₃ perovskite:



Frost *et al.* [194] estimated ~1 wt% of metallic iron to be present in the lower mantle. Similar reaction was proposed also with post-perovskite [195], and for both MgSiO₃ phases the process (42) was confirmed in our theoretical study [196]. Iron is likely to be in the hcp-structure at conditions of the lower mantle. The presence of free Fe in the mantle is geochemically very important and has implications for the oxygen fugacity, extraction of siderophile elements, and growth of the Earth's core. Reaction (42) is strongly enhanced when alumina is present in MgSiO₃ perovskite, whereas in case of post-perovskite alumina makes no difference [196].

An interesting V_3O_5 -like phase of Al_2SiO_5 (Fig. 41) was suggested [197] to be stable at conditions of the lower mantle and be the main host of aluminium there. However, more controlled experiments [7] and *ab initio* calculations [8] showed that the mixture of Al_2O_3 and SiO_2 is more stable at all lower mantle conditions. However, according to numerous experiments, at mantle pressures and temperatures Al_2O_3 is known to easily dissolve into $MgSiO_3$ phases, which therefore should be the main hosts of alumina in the lower mantle.

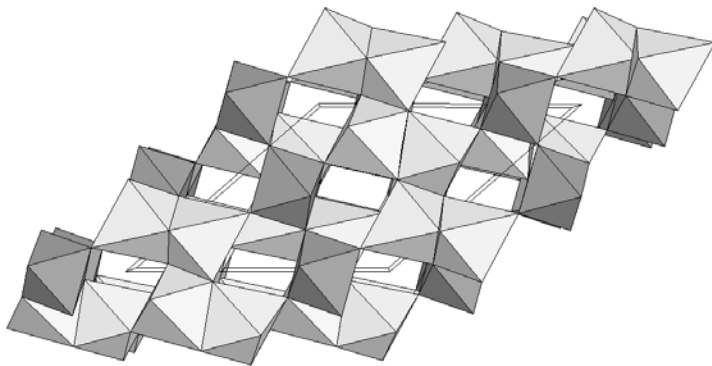


Fig. 41. Structure of a hypothetical V_3O_5 -type phase of Al_2SiO_5 . Si-octahedra are displayed as darker polyhedra. From [8].

Mineralogy of carbon in the Earth's interior is another interesting topic. Experiments [198] show extremely small solubility of CO_2 in mantle minerals, implying that most of the Earth's carbon should be located in the form of carbonates of Mg and Ca in the mantle, or perhaps in the form of diamond or CO_2 . The presence of volatile CO_2 in the mantle can enhance processes of chemical equilibration, strongly affect the rheological properties of mantle rocks and cause their partial melting. To assess the possibility of decomposition of the carbonates leading to the formation of free CO_2 , one first has to find crystal structures of the carbonates. It is well known that dolomite $CaMg(CO_3)_2$ decomposes into $CaCO_3 + MgCO_3$ at >5 GPa, and that above ~ 1 GPa $CaCO_3$ undergoes a calcite-aragonite transition.

For $CaCO_3$, Ono *et al.* [199] found a post-aragonite phase transition at ~ 40 GPa using laser-heated diamond anvil cells, and the structure of the new phase could not be solved. For $MgCO_3$, using the same technique, Isshiki *et al.* [200] found that magnesite undergoes a phase transition at ~ 100 GPa, and also could not solve the structure of the post-magnesite phase from experimental data.

Using USPEX, we solved the structure of $CaCO_3$ post-aragonite [35], obtaining close agreement with the experimental diffraction pattern and reproducing stability

above ~ 40 GPa. This structure (Fig. 42a) can be represented as a hexagonal close packing of Ca and O atoms, in which C atoms occupy centres of oxygen triangles. This explains the high density and enormous stability range of this phase, 42–137 GPa. Above 137 GPa we predicted [35] yet another phase, which contains tetrahedral carbonate groups (Fig. 42b); this unusual carbonate was recently synthesized at pressures given by theory (S. Ono, pers. comm.). Both of these structures belong to new structure types, not previously known for any compounds.

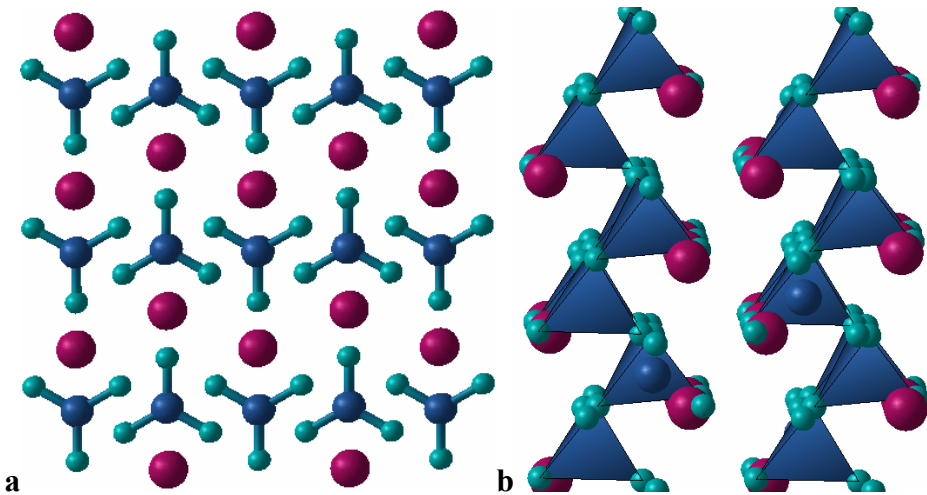


Fig. 42. New high-pressure forms of CaCO_3 stable at conditions of the Earth's lower mantle: a) post-aragonite (space group $Pmmn$), b) $C222_1$ post-postaragonite. Adapted from [35].

The behaviour of MgCO_3 is much less understood. A pyroxene structure with the space group $C2/c$ was found to become more favourable than magnesite above ~ 100 GPa [201]; however, this does not exclude the possibility of even more favourable structures. To find the structure of post-magnesite, we performed USPEX simulations at 150 GPa for systems containing 5, 10, 15, 20 and 30 atoms/cell. As a result, we identified two most stable structures: a $P2_1$ structure stable between 88–122 GPa, and a $Pna2_1$ structure with tetrahedral carbonate ions (which form chains), stable above 122 GPa. The structures are shown in Fig. 43 and Table 6. Four points issues are worth noting:

1. The first transition is predicted at only 88 GPa, much below the reported experimental pressure of 110 GPa [200]. This is an extraordinarily large difference at this level of theory (GGA-PAW), which suggests an experimental re-investigation.

2. The diffraction patterns of both new structures bear much similarity with experimental results ([200] and unpublished data of S. Ono and A. Kubo), but the agreement is not as convincing as for CaCO_3 [35].

3. While C-O bond lengths in CO_3 -triangles are nearly equal in the $P2_1$ phase, CO_4 -tetrahedra in the $Pna2_1$ structure are strongly distorted (C-O distances of ~ 1.40 Å and ~ 1.30 Å to bridging and non-bridging oxygens, respectively).

4. As Fig. 43c shows, there are several metastable structures, which are energetically very competitive in a wide pressure range. This hints on possibly severe metastability problems in experimental studies – e.g. possible coexistence of several phases in experiments.

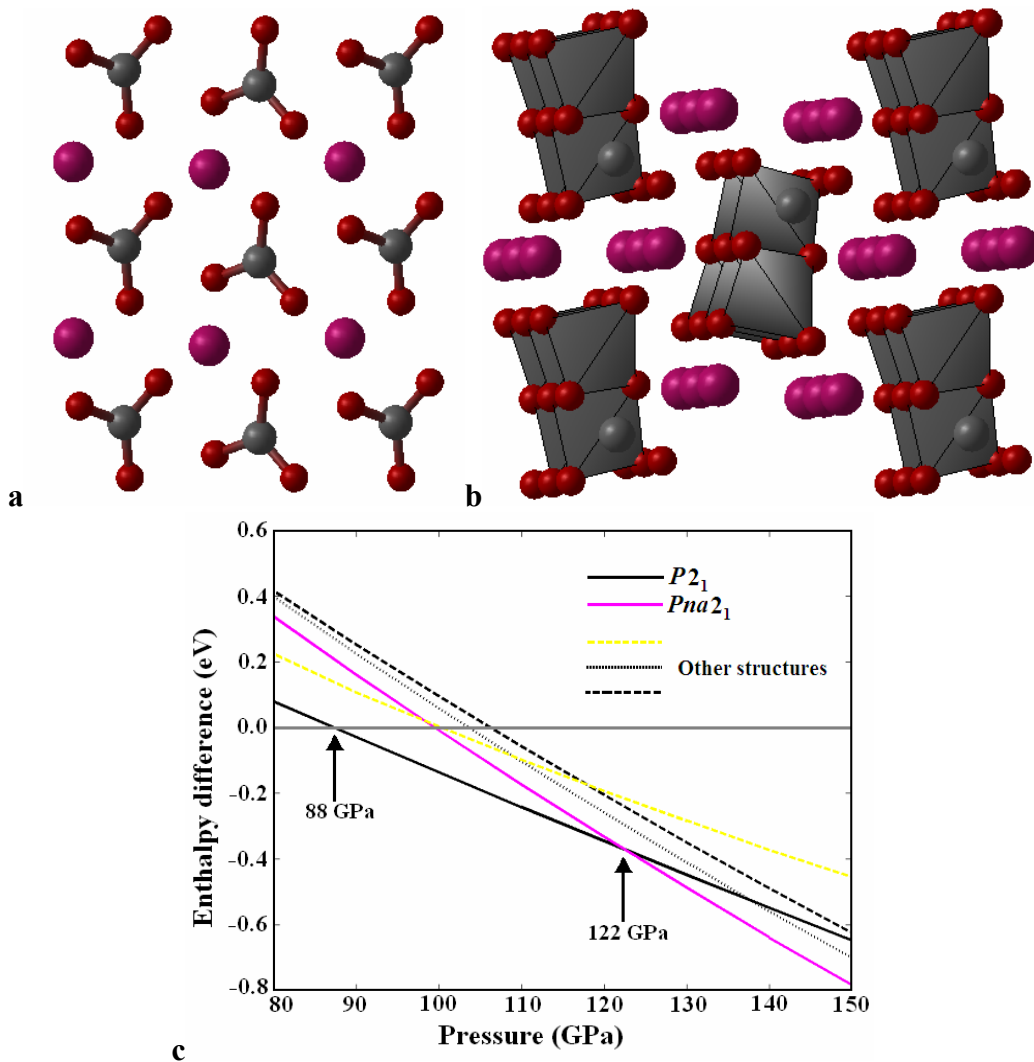


Fig. 43. High-pressure structural stability of MgCO_3 : a) $P2_1$ structure, b) $Pna2_1$ structure, c) enthalpies of several structures relative to magnesite (per formula unit). Pyroxene structure of [201] is metastable at all pressures (shown among “other” structures).

Keeping in mind the preliminary nature of our results for MgCO_3 , in Table 7 we compare the high-pressure behaviour of MgCO_3 , CaCO_3 and SrCO_3 . From our results it is already clear that MgCO_3 behaves differently from CaCO_3 and SrCO_3 , which can be tracked back to the smaller size of Mg^{2+} compared to Ca^{2+} and Sr^{2+} . This determines lower coordination of Mg in carbonates, compared with Ca and Sr (see Table 7).

TABLE 6. Crystal structures of high-pressure MgCO_3 polymorphs at 120 GPa.

$P2_1$ phase. $a=2.6054$, $b=5.8921$, $c=3.9971$ Å, $\beta=106.26^\circ$.			
	X	Y	z
Mg	0.7802	0.0795	0.5221
C	0.6544	0.3934	-0.0417
O1	0.6676	0.3724	0.2704
O2	0.3811	0.2668	-0.2725
O3	0.8870	0.5581	-0.1360

Bond lengths: Mg-O1=1.892, 1.977, 2.020 Å; Mg-O2=1.858, 1.903, 2.081 Å; Mg-O3=1.975, 1.979, 2.366 Å. C-O1=1.245 Å; C-O2=1.244 Å; C-O3=1.257 Å.
--

$Pna2_1$ phase. $a=7.1952$, $b=5.5687$, $c=2.8069$ Å.			
	X	Y	z
Mg	0.1868	0.4841	0.0517
C	0.0145	0.1642	0.7970
O1	-0.0784	0.3270	0.0267
O2	0.1528	0.2580	0.5699
O3	0.1067	-0.0210	0.0459

Bond lengths: Mg-O1=1.869, 1.972, 2.100, 2.421 Å; Mg-O2=1.864, 1.913, 1.939 Å; Mg-O3=2.033, 2.055 Å. C-O1=1.298 Å; C-O2=1.292 Å; C-O3=1.376, 1.411 Å.
--

TABLE 7. Summary of high-pressure phases of MgCO_3 , CaCO_3 and SrCO_3 .
“CN” denotes coordination numbers of cations in structure types.

	Pressure increases →					
	Structure types					
Compound	Calcite CN(C)=3 CN(M)=6	Aragonite CN(C)=3 CN(M)=9	$P2_1$ CN(C)=3 CN(M)=9	Post-aragonite CN(C)=3 CN(M)=12	$Pna2_1$ CN(C)=4 CN(M)=9	$C222_1$ CN(C)=4 CN(M)=10
MgCO_3	0-88 GPa	-	88-122 GPa	-	>122 GPa	-
CaCO_3	0-4 GPa	4-42 GPa	-	42-137 GPa	-	>137 GPa
SrCO_3	-	0-10 GPa	-	> 10 GPa	-	(stable?)

6. Concluding remarks.

Our understanding of high-pressure phenomena is still, at best, sketchy. Since the close-packing principle was found to fail in many cases, we are left without a simple general principle determining crystal density. Standard chemical experience and rules of bonding also fail very often, reflecting the importance of density (rather than energy) and changing electronic structure of atoms under pressure. We have no doubt that new general rules, applicable to high-pressure crystallography, will appear after a sufficient amount of experimental and theoretical information is accumulated.

Along this direction, our knowledge about high-pressure phenomena has evolved a great deal over the last 10-15 years, and some of these advances are described in this thesis. Reliable methods for pressure measurement have been developed (see [27]). A new major Earth-forming mineral, $MgSiO_3$ post-perovskite, has been discovered [11,126] – this has provided detailed understanding of the Earth's core-mantle boundary region and sheds new light on the structure, dynamics and evolution of our planet. A number of new mineral phases and high-pressure phases of the elements have been found [35,36,115,119,120,144]. It appears that the Jahn-Teller distortion plays an important role in high-pressure behaviour of many elements. We have seen that even pure elements can exhibit significantly ionic bonding. New methodologies, such as USPEX and metadynamics, have allowed, for the first time, a new range of problems to be addressed theoretically. In particular, the USPEX method enables purely *ab initio* prediction of the stable crystal structure on the basis of only the chemical composition. What comes next?

Concerning crystal structure prediction, a theoretician's dream would be to predict not only the stable structures, but also the stable stoichiometries – starting just from the given set of atoms and finding all their favourable combinations. Time- and length- scale problems in simulations have to be addressed to enable realistic simulation of many phenomena (e.g., crystal nucleation and growth, dislocations in crystals and plastic deformation).

Among the most interesting case studies, we would mention the following:

- 1) Understanding possible chemical reactions between liquid Fe-based alloys of the Earth's core and mantle minerals. Such reactions can produce new interesting mineral phases [202].
- 2) Understanding the high- P,T phase diagram of Fe-based alloys and their plastic deformation at conditions of the Earth's inner core. This should clarify the nature of seismic anisotropy of the inner core and its observed stratification [203-205].

- 3) Determination of high-pressure structures of hydrogen, conditions of its metallization and assessment of the possibility of quantum melting.
- 4) High- P, T chemistry of the $\text{H}_2\text{O}-\text{CH}_4-\text{NH}_3$ system, important for understanding planets Neptune and Uranus, their internal structure and mechanisms of heat production.
- 5) Exploration of high-pressure chemistry of noble gases, in particular, the conditions necessary for stable compound formation and nature of chemical bonding in those compounds.

There are also many general questions. For instance, why is superconductivity so ubiquitous in elements under pressure? Why elements under pressure emulate their heavier analogues from the same group of the Periodic Table? What is the stable structure of an element in the limit of infinite compression – hcp, fcc, bcc, or something else? And what is the structure of matter inside neutron stars?

7. References

1. Dziewonski A.M. & Anderson D.L. (1981). Preliminary Reference Earth Model. *Phys. Earth Planet. Inter.* **25**, 297-356.
2. Liu L.-G. & Bassett W.A. (1986). *Elements, Oxides, and Silicates. High-Pressure Phases with Implications for the Earth's Interior.* Oxford University Press: N.Y., 250 pp.
3. Oganov A.R., Gillan M.J., Price G.D. (2005). Structural stability of silica at high pressures and temperatures. *Phys. Rev.* **B71**, art. 064104.
4. McMahon M.I., Nelmes R.J. (2006). High-pressure structures and phase transformations in elemental metals. *Chem. Soc. Rev.* **35**, 943-963.
5. Bukowinski M.S.T. (1994). Quantum geophysics. *Ann. Rev. Earth Planet. Sci.* **22**, 167-205.
6. Burdett J.K. (1995). *Chemical Bonding in Solids.* Oxford University Press: N.Y., 319 pp.
7. Schmidt M.W., Poli S., Comodi P., & Zanazzi P.F. (1997). High-pressure behavior of kyanite: Decomposition of kyanite into stishovite and corundum. *Am. Mineral.* **82**, 460-466.
8. Oganov A.R. & Brodholt J.P. (2000). High-pressure phases in the Al_2SiO_5 system and the problem of Al-phase in Earth's lower mantle: ab initio pseudopotential calculations. *Phys. Chem. Minerals* **27**, 430-439.
9. Sanloup C., Schmidt B.C., Perez E.M.C., Jambon A., Gregoryanz E., Mezouar M. (2005). Retention of xenon in quartz and Earth's missing xenon. *Science* **310**, 1174-1177.
10. Ono S., Kikegawa T., Ohishi Y. (2005). A high-pressure and high-temperature synthesis of platinum carbide. *Solid State Comm.* **133**, 55-59.
11. Oganov A.R., Ono S. (2004). Theoretical and experimental evidence for a post-perovskite phase of MgSiO_3 in Earth's D'' layer. *Nature* **430**, 445-448.
12. Neaton J.B., Ashcroft N.W. (1999). Pairing in dense lithium. *Nature* **400**, 141-144.
13. Maksimov E.G., Magnitskaya M.V., Fortov V.E. (2005). Non-simple behavior of simple metals at high pressure. *Physics Uspekhi* **48**, 761-780.
14. Pisani C. (1996). Ab initio approaches to the quantum-mechanical treatment of periodic systems. In: *Quantum-mechanical ab initio calculation of the properties of crystalline materials.* Pisani C. (ed.). Lecture Notes in Chemistry, v. 67, p.47-75. Springer-Verlag: Berlin.
15. Zharkov V.N. & Kalinin V.A. (1968). *Equations of State of Solids at High Pressures and Temperatures.* Nauka: Moscow, 312 pp. (in Russian).
16. Poirier J.-P. (2000). *Introduction to the Physics of the Earth's Interior.* 2nd edition. Cambridge University Press: Cambridge, 326 pp.
17. Hemley R.J., Mao H.K., Gramsch S.A. (2000). Pressure-induced transformations in deep mantle and core minerals. *Mineral. Mag.* **64**, 157-184.
18. Ono S., Oganov A.R. (2005). *In situ* observations of phase transition between perovskite and CaIrO_3 -type phase in MgSiO_3 and pyrolytic mantle composition. *Earth Planet. Sci. Lett.* **236**, 914-932.
19. Landau L.D. & Lifshitz E.M. (1980). *Statistical Physics.* Part I. (Theoretical Physics, v. 5). Third edition. Moscow: Nauka, 584 pp. (in Russian).
20. Piermarini G.J. (1975). Calibration of pressure dependence of R1 ruby fluorescence line to 195 kbar. *J. Appl. Phys.* **46**, 2774-2780.

21. Mao H.K. (1978). Specific volume measurements of Cu, Mo, Pd, and Ag and calibration of ruby R1 fluorescence pressure gauge from 0.06 to 1 Mbar. *J. Appl. Phys.* **49**, 3276-3283.
22. Mao H.K. (1986). Calibration of the ruby pressure gauge to 800 kbar under quasi-hydrostatic conditions. *J. Geoph. Res.* **91**, 4673-4676.
23. Aleksandrov I.V. (1987). Diamond at high pressures – Raman scattering, equation of state and high-pressure scale. *Zh. Eksp. Teor. Fiz.* **93**, 680-691.
24. Dewaele A., Loubeire P., Mezouar M. (2004). Equations of state of six metals above 94 GPa. *Phys. Rev.* **B70**, art. 094112.
25. Oganov A.R. & Dorogokupets P.I. (2003). All-electron and pseudopotential study of MgO: Equation of state, anharmonicity, and stability. *Phys. Rev.* **B67**, art. 224110.
26. Dorogokupets P.I. & Oganov A.R. (2003). Equations of state of Cu and Ag and the revised ruby pressure scale. *Doklady Earth Sciences* **391A**, 854-857.
27. Dorogokupets P.I., Oganov A.R. (2007). Ruby, metals, and MgO as alternative pressure scales: A semiempirical description of shock-wave, ultrasonic, x-ray, and thermochemical data at high temperatures and pressures. *Phys. Rev.* **B75**, art. 024115.
28. Oganov A.R. & Dorogokupets P.I. (2004). Intrinsic anharmonicity in thermodynamics and equations of state of solids. *J. Phys.: Cond. Matter.* **16**, 1351-1360.
29. Holzapfel W.B. (2003). Refinement of the ruby luminescence pressure scale. *J. Appl. Phys.* **93**, 1813-1818.
30. Kunc K., Loa I., Syassen K. (2003). Equation of state and phonon frequency calculations of diamond at high pressures. *Phys. Rev.* **B68**, art. 094107.
31. Chijoike A.D., Nellis W.J., Soldatov A., Silvera I.F. (2005). The ruby pressure standard to 150 GPa. *J. Appl. Phys.* **98**, art. 114905.
32. Holzapfel W.B. (2005). Progress in the realization of a practical pressure scale for the range 1-300 GPa. *High-Pressure Research* **25**, 87-96.
33. Maddox J. (1988). Crystals from first principles. *Nature* **335**, 201.
34. Martoňák R., Laio A., Parrinello M. (2003). Predicting crystal structures: The Parrinello-Rahman method revisited. *Phys. Rev. Lett.* **90**, art. 075503.
35. Oganov A.R., Glass C.W., Ono S. (2006). High-pressure phases of CaCO₃: crystal structure prediction and experiment. *Earth Planet. Sci. Lett.* **241**, 95-103.
36. Oganov A.R., Glass C.W. (2006). Crystal structure prediction using evolutionary techniques: principles and applications. *J. Chem. Phys.* **124**, art. 244704.
37. Glass C.W., Oganov A.R., Hansen N. (2006). USPEX – evolutionary crystal structure prediction. *Comp. Phys. Comm.* **175**, 713-720.
38. Born M. & Huang K. (1954). *Dynamical Theory of Crystal Lattices*. Oxford University Press: Oxford, 420 pp.
39. Dove M.T. (1993). *Introduction to Lattice Dynamics*. Cambridge University Press, 1993, 258 pp.
40. Thijssen J.M. (1999). *Computational Physics*. Cambridge University Press: Cambridge, 546 pp.
41. Cohen R.E. (1999). Bonding and electronic structure of minerals. In: *Micrsoscopic Properties and Processes in Minerals*, NATO Science Series, v. C543. K. Wright and R. Catlow (eds.), Kluwer: Dordrecht, pp. 201-264.

42. Kohn W. (1999). Nobel Lecture: Electronic structure of matter – wave functions and density functionals. *Rev. Mod. Phys.* **71**, 1253-1266.
43. Oganov A.R., Brodholt J.P., Price G.D. (2002). Ab initio theory of thermoelasticity and phase transitions in minerals. *EMU Notes in Mineralogy* v.4 ('Energy Modelling in Minerals', edited by C.M. Gramaccioli), pp.83-170.
44. Oganov A.R. (2003). Theory of Minerals at High and Ultrahigh Pressures: Structure, Properties, Dynamics, and Phase Transitions. In: *High-Pressure Crystallography*, NATO Science Series: II: Mathematics, Physics and Chemistry, vol. 140, p.199-215 (edited by A.Katrusiak, P.F.McMillan). Kluwer Academic Publishers, Dordrecht.
45. Jung D.Y., Oganov A.R. (2005). Basics of first-principles simulation of matter under extreme conditions. *EMU Notes in Mineralogy* v.7 ("High-Pressure Behaviour of Minerals", edited by R. Miletich), 117-138.
46. Adams D.J., Oganov A.R. (2005). Theory of minerals at extreme conditions: predictability of structures and properties. *EMU Notes in Mineralogy* v.7 ("High-Pressure Behaviour of Minerals", edited by R. Miletich), 441-457.
47. Gillan M.J., Alfe D., Brodholt J., Vočadlo L., Price G.D. (2006). First-principles modelling of Earth and planetary materials at high pressures and temperatures. *Rep. Progr. Phys.* **69**, 2365-2441.
48. Martin R.M. (2006). *Electronic Structure. Basic Theory and Practical Methods*. Cambridge University Press.
49. Foulkes W.M.C., Mitas L., Needs R.J., & Rajagopal G. (2001). Quantum Monte Carlo simulations of solids. *Rev. Mod. Phys.* **73**, 33-83.
50. Becke A.D. (1993). Density-functional thermochemistry. 3. The role of exact exchange. *J. Chem. Phys.* **98**, 5648-5652.
51. Hohenberg P. & Kohn W. (1964). Inhomogeneous electron gas. *Phys. Rev.* **136**, B864-B871.
52. Kohn W. & Sham L.J. (1965). Self-consistent equations including exchange and correlation effects. *Phys. Rev.* **140**, A1133-A1138.
53. Mermin N.D. (1965). Thermal properties of inhomogeneous electron gas. *Phys. Rev.* **A137**, 1441-1443.
54. Parr R.G. & Yang W. (1989). *Density-Functional Theory of Atoms and Molecules*. Oxford University Press: Oxford, 333 pp.
55. Perdew J.P., Kurth S. (1998). Density functionals for non-relativistic Coulomb systems. In: Joubert D.P. (ed.) *Density Functionals: Theory and Applications*. Lecture Notes in Physics, v. 500, p.8-59. Springer Verlag: Berlin.
56. Perdew J.P. & Burke K. (1996). Comparison shopping for a gradient-corrected density functional. *Int. J. Quant. Chem.* **57**, 309-319.
57. Ceperley D.M. & Alder B.J. (1980). Ground state of the electron gas by a stochastic method. *Phys. Rev. Lett.* **45**, 566-569.
58. Ortiz G. & Ballone P. (1994). Correlation energy, structure factor, radial distribution function, and momentum distribution of the spin-polarised uniform electron gas. *Phys. Rev.* **B50**, 1391-1405.
59. Perdew J.P., Wang Y. (1992). Accurate and simple analytic representation of the electron-gas correlation energy. *Phys. Rev.* **B45**, 13244-13249.

60. Vosko S.H., Wilk L., Nusair M. (1980). Accurate spin-dependent electron liquid correlation energies for local spin density calculations: a critical analysis. *Can J. Phys.* **58**, 1200-1211.
61. Perdew J.P., Burke K., Ernzerhof M. (1996). Generalized gradient approximation made simple. *Phys. Rev. Lett.* **77**, 3865-3868.
62. Winter J.K. & Ghose S. (1979). Thermal expansion and high-temperature crystal chemistry of the Al_2SiO_5 Polymorphs. *Am. Mineral.* **64**, 573-586.
63. Jung D.Y., Oganov A.R. (2005). *Ab initio* study of the high-pressure behaviour of CaSiO_3 perovskite. *Phys. Chem. Minerals* **32**, 146-153.
64. Tao J.M., Perdew J.P., Staroverov V.N., Scuseria G.E. (2003). Climbing the density functional ladder: Nonempirical meta-generalized gradient approximation designed for molecules and solids. *Phys. Rev. Lett.* **91**, art. 146401.
65. Becke A.D. (2000). Simulation of delocalised exchange by local density functionals. *J. Chem. Phys.* **112**, 4020-4026.
66. Staroverov V.N., Scuseria G., Tao J., Perdew J.P. (2004). Tests of a ladder of density functionals for bulk solids and surfaces. *Phys. Rev.* **B69**, 075102.
67. Perdew J.P., Tao J.M., Staroverov V.N., Scuseria G.E. (2004). Meta-generalized gradient approximation: Explanation of a realistic nonempirical density functional. *J. Chem. Phys.* **120**, 6898-6911.
68. Kohn W., Meir Y., Makarov D.E. (1998). Van der Waals energies in density functional theory. *Phys. Rev. Lett.* **80**, 4153-4156.
69. Fuchs M., Gonze X. (2002). Accurate density functionals: Approaches using the adiabatic-connection fluctuation-dissipation theorem. *Phys. Rev.* **B65**, art. 235109.
70. Aryasetiawan F., Gunnarsson O. (1998). The GW method. *Rep. Prog. Phys.* **61**, 237-312.
71. Liechtenstein A.I., Anisimov V.I., Zaanen J. (1995). Density functional theory and strong interactions – orbital ordering in Mott-Hubbard insulators. *Phys. Rev.* **B52**, R5467-R5470.
72. Szotek Z., Temmerman W.M. (1993). Application of self-interaction correction to transition-metal oxides. *Phys. Rev.* **B47**, 4029-4032.
73. Georges A., Kotliar G., Krauth W., Rozenberg M.J. (1996). Dynamical mean-field theory of strongly correlated fermion systems and the limit of infinite dimensions. *Rev. Mod. Phys.* **68**, 13-125.
74. Attaccalite C. (2005). RVB phase of hydrogen at high pressure: towards the first ab-initio molecular dynamics by quantum Monte Carlo. *PhD thesis*, SISSA, Trieste, Italy.
75. Troullier N. & Martins J.L. (1991). Efficient pseudopotentials for plane-wave calculations. *Phys. Rev.* **B43**, 1993-2006.
76. Rappe A.M., Rabe K.M., Kaxiras E., & Joannopoulos J.D. (1990). Optimized pseudopotentials. *Phys. Rev.* **B41**, 1227-1230.
77. Vanderbilt D. (1990). Soft self-consistent pseudopotentials in a generalized eigenvalue problem. *Phys. Rev.* **B41**, 7892-7895.
78. Louie S.G., Froyen S., & Cohen M.L. (1982). Nonlinear ionic pseudopotentials in spin-density functional calculations. *Phys. Rev.* **B26**, 1738-1742.
79. Singh D.J. (1994). *Planewaves, Pseudopotentials and the LAPW Method*. Kluwer: Boston, 115 pp.
80. Blöchl P.E. (1994). Projector augmented-wave method. *Phys. Rev.* **B50**, 17953-17979.

81. Kresse G., Joubert D. (1999). From ultrasoft pseudopotentials to the projector augmented-wave method. *Phys. Rev.* **B59**, 1758-1775.
82. Holzwarth N.A.W., Matthews G.E., Dunning R.B., Tackett A.R., Zeng Y. (1997). Comparison of the projector augmented-wave, pseudopotential, and linearized augmented-plane-wave formalisms for density-functional calculations of solids. *Phys. Rev.* **B55**, 2005-2017.
83. Payne M.C., Teter M.P., Allan D.C., Arias T.A., Joannopoulos J.D. (1992). Iterative minimization techniques for *ab initio* total energy calculations: molecular dynamics and conjugate gradients. *Rev. Mod. Phys.* **64**, 1045-1097.
84. Kresse G. & Furthmuller J. (1996). Efficiency of ab initio total-energy calculations for metals and semiconductors using a plane-wave basis set. *Comp. Mater. Sci.* **6**, 15-50.
85. Gonze X., Beuken J.-M., Caracas R., Detraux F., Fuchs M., Rignanese G.-M., Sindic L., Verstraete M., Zerah G., Jollet F., Torrent M., Roy A., Mikami M., Ghosez Ph., Raty J.-Y., Allan D.C. (2002). First-principles computation of materials properties: the ABINIT software project. *Comp. Mater. Sci.* **25**, 478-492.
86. Gonze X., Rignanese G.M., Verstraete M., Beuken J.M., Pouillon Y., Caracas R., Jollet F., Torrent M., Zerah G., Mikami M., Ghosez P., Veithen M., Raty J.Y., Olevano V., Bruneval F., Reining L., Godby R., Onida G., Hamann D.R., Allan D.C. (2005). A brief introduction to the ABINIT software package. *Z. Krist.* **220**, 558-562.
87. Oganov A.R., Brodholt J.P., & Price G.D. (2000). Comparative study of quasiharmonic lattice dynamics, molecular dynamics and Debye model in application to MgSiO₃ perovskite. *Phys. Earth Planet. Inter.* **122**, 277-288.
88. Allen M.P. & Tildesley D.J. (1987). *Computer Simulation of Liquids*. Clarendon Press: Oxford, 385 pp.
89. Frenkel, D. & Smit, B. (2002): *Understanding molecular simulation*. San Diego: Academic Press, 638 pp.
90. Remler D.K. & Madden P.A. (1990). Molecular dynamics without effective potentials via the Carr-Parrinello approach. *Mol. Phys.* **70**, 921-966.
91. Venkataraman G., Feldkamp L.A., & Sahni V.C. (1975). *Dynamics of Perfect Crystals*. The MIT Press: Cambridge, 517 pp.
92. Baroni S., de Gironcoli S., Dal Corso A., Gianozzi P. (2001). Phonons and related crystal properties from density-functional perturbation theory. *Rev. Mod. Phys.* **73**, 515-562.
93. Gonze X., Rignanese G.M., Caracas R. (2005). First-principle studies of the lattice dynamics of crystals, and related properties. *Z. Krist.* **220**, 458-472.
94. Nosé S. (1984). A molecular dynamics method for simulations in the canonical ensemble. *Mol. Phys.* **52**, 255-268.
95. Parrinello M. & Rahman A. (1981). Polymorphic transitions in single crystals: A new molecular dynamics method. *J. App. Phys.* **52**, 7182-7190.
96. Car R. & Parrinello M. (1985). Unified approach for molecular dynamics and density-functional theory. *Phys. Rev. Lett.* **55**, 2471-2474.
97. Alf   D., Gillan M.J., & Price G.D. (1999). The melting curve of iron at the pressures of the Earth's core from ab initio calculations. *Nature* **401**, 462-464.

98. Alf   D., Gillan M.J., & Price G.D. (2000). Constraints on the composition of the Earth's core from ab initio calculations. *Nature* **405**, 172-175.
99. Oganov A.R., Brodholt J.P., & Price G.D. (2001). High-*P/T* elastic constants of MgSiO₃ perovskite: towards interpreting seismic tomography. *Nature* **411**, 934-937.
100. Ancilotto F., Chiarotti G.L., Scandolo S., & Tosatti E. (1997). Dissociation of methane into hydrocarbons at extreme (planetary) pressure and temperature. *Science* **275**, 1288-1290.
101. Cavazzoni C., Chiarotti G.L., Scandolo S., Tosatti E., Bernasconi M., & Parrinello M. (1999). Superionic and metallic states of water and ammonia at giant planet conditions. *Science* **283**, 44-46.
102. Belonoshko A.B., Ahuja R., Johansson B. (2003). Stability of the body-centred-cubic phase of iron in the Earth's inner core. *Nature* **424**, 1032-1034.
103. Vo  adlo L., Alfe D., Gillan M.J., Wood I.G., Brodholt J.P., Price G.D. (2003). Possible thermal and chemical stabilization of body-centred-cubic iron in the Earth's core. *Nature* **424**, 536-539.
104. Matsui M. (1989). Molecular dynamics study of the structural and thermodynamic properties of MgO crystal with quantum correction. *J. Chem. Phys.* **91**, 489-494.
105. Oganov A.R., Brodholt J.P., & Price G.D. (2001). *Ab initio* elasticity and thermal equation of state of MgSiO₃ perovskite, *Earth Planet. Sci. Lett.* **184**, 555-560.
106. Stixrude L., Hemley R.J., Fei Y., Mao H.K. (1992). Thermoelasticity of silicate perovskite and magnesiow  stite and stratification of the Earth's mantle, *Science* **257**, 1099-1101.
107. Adams D.J., Oganov A.R. (2006). *Ab initio* molecular dynamics study of CaSiO₃ perovskite at *P-T* conditions of Earth's lower mantle. *Phys. Rev.* **B73**, 184106.
108. Baroni S., Gianozzi P., & Testa A. (1987). Green-function approach to linear response in solids. *Phys. Rev. Lett.* **58**, 1861-1864.
109. Gonze X. & Lee C. (1997). Dynamical matrices, Born effective charges, dielectric permittivity tensors, and interatomic force constants from density-functional perturbation theory. *Phys. Rev.* **B55**, 10355-10368.
110. Ghose S., Krisch M., Oganov A.R., Beraud A., Bossak A., Gulve R., Seelaboyina R., Yang H., Saxena S.K. (2006). Lattice dynamics of MgO at high pressure: theory and experiment. *Phys. Rev. Lett.* **96**, art. 035507.
111. Strachan A.,   a  in T., Goddard W.A. III (1999). Phase diagram of MgO from density-functional theory and molecular-dynamics simulations. *Phys. Rev.* **B60**, 15084-15093.
112. Karki B.B., Wentzcovitch R.M., de Gironcoli S., & Baroni S. (1999). First-principles determination of elastic anisotropy and wave velocities of MgO at lower mantle conditions. *Science* **286**, 1705-1707.
113. Oganov A.R., Gillan M.J., Price G.D. (2003). Ab initio lattice dynamics and structural stability of MgO. *J. Chem. Phys.* **118**, 10174-10182.
114. Oganov A.R., Price G.D. (2005). *Ab initio* thermodynamics of MgSiO₃ perovskite at high pressures and temperatures. *J. Chem. Phys.* **122**, art. 124501.
115. Oganov A.R., S. Ono (2005). The high-pressure phase of alumina and implications for Earth's D" layer. *Proc. Natl. Acad. Sci.* **102**, 10828-10831.
116. Tsuchiya T., Tsuchiya J., Umemoto K., Wentzcovitch R.M. (2004). Phase transition in MgSiO₃ perovskite in the earth's lower mantle. *Earth Planet. Sci. Lett.* **224**, 241-248.

117. Meade C., Mao H.K., Hu J.Z. (1995). High-temperature phase transition and dissociation of $(\text{Mg},\text{Fe})\text{SiO}_3$ perovskite at lower mantle pressures. *Science* **268**, 1743-1745.
118. Saxena S.K., Dubrovinsky L.S., Lazor P., Cerenius Y., Häggkvist P., Hanfland M., Hu J. (1996). Stability of perovskite (MgSiO_3) in the Earth's mantle. *Science* **274**, 1357-1359.
119. Oganov A.R., Glass C.W., Ma Y.-Z., Ma Y.-M., Chen J. (2007). Ionic high-pressure form of elemental boron. *Nature*, under review.
120. Ma Y.-M., Oganov A.R., Glass C.W. (2007). Structure of metallic ζ -phase of oxygen and isosymmetric nature of ε - ζ transition. *Phys. Rev. Lett.*, under review.
121. Xie Y., Tse J.S., Cui T., Oganov A.R., He Z., Ma Y., Zou G. (2007). Electronic and phonon instabilities in face-centered cubic alkali metals under pressure. *Phys. Rev. B* **75**, art. 064102.
122. Cynn H., Isaak D.G., Cohen R.E., Nicol M.F., Anderson O.L. (1990). A high-pressure phase transition of corundum predicted by the potential induced breathing model. *Am. Mineral.* **75**, 439-442.
123. Funamori N. & Jeanloz R. (1997). High-pressure transformation of Al_2O_3 . *Science* **278**, 1109-1111.
124. Ono S., Kikegawa T., Ohishi Y. (2004). High-pressure phase transition of hematite, Fe_2O_3 . *J. Phys. Chem. Solids* **65**, 1527-1530.
125. Caracas R., Cohen R.E. (2005). Prediction of a new phase transition in Al_2O_3 at high pressures. *Geophys. Res. Lett.* **32**, art. L06303.
126. Murakami, M., Hirose, K., Kawamura, K., Sata, N. & Ohishi, Y. (2004). Post-perovskite phase transition in MgSiO_3 . *Science* **307**, 855-858 (2004).
127. Thomson K.T., Wentzcovitch R.M., Bukowinski M.S.T. (1996). Polymorphs of alumina predicted by first principles: Putting pressure on the ruby pressure scale. *Science* **274**, 1880-1882.
128. Maddox J. (1988). Crystals from first principles. *Nature* **335**, 201.
129. Gavezzotti A. (1994). Are crystal structures predictable? *Acc. Chem. Res.* **27**, 309-314.
130. Ball P. (1996). Materials chemistry - Scandal of crystal design... *Nature* **381**, 648-650.
131. Day G.M., Motherwell W.D.S., Ammon H.L., Boerrigter S.X.M., Della Valle R.G., Venuti E., Dzyabchenko A., Dunitz J.D., Schweizer B., van Eijck B.P., Erk P., Facelli J.C., Bazterra V.E., Ferraro M.B., Hofmann D.W.M., Leusen F.J.J., Liang C., Pantelides C.C., Karamertzanis P.G., Price S.L., Lewis T.C., Nowell H., Torrisi A., Scheraga H.A., Arnautova Y.A., Schmidt M.U. & Verwer P. (2005). A third blind test of crystal structure prediction. *Acta Cryst. B* **61**, 511-527.
132. Martoňák R., Laio A., Bernasconi M., Ceriani C., Raiteri P., Zipoli F., Parrinello M. (2005). Simulation of structural phase transitions by metadynamics. *Z. Krist.* **220**, 489-498.
133. Martoňák R., Donadio D., Oganov A.R., Parrinello M. (2006). Crystal structure transformations in SiO_2 from classical and *ab initio* metadynamics. *Nature Materials* **5**, 623-626.
134. Pannetier J., Bassasalsina J., Rodriguez-Carvajal J., Caignaert V. (1990). Prediction of crystal structures from crystal chemistry rules by simulated annealing. *Nature* **346**, 343-345.
135. Schön J.C., Jansen M. (1996). First step towards planning of syntheses in solid-state chemistry: Determination of promising structure candidates by global optimization. *Angew. Chem. – Int. Ed.* **35**, 1287-1304.
136. Wales D.J., Doye J.P.K. (1997). Global optimization by basin-hopping and the lowest energy structures of Lennard-Jones clusters containing up to 110 atoms. *J. Phys. Chem. A* **101**, 5111-5116.

137. Gödecker S. (2004). Minima hopping: An efficient search method for the global minimum of the potential energy surface of complex molecular systems. *J. Chem. Phys.* **120**, 9911-9917.
138. Bush T.S., Catlow C.R.A. & Battle P.D. (1995). Evolutionary programming techniques for predicting inorganic crystal structures. *J. Mater. Chem.* **5**, 1269-1272.
139. Woodley S.M., Battle P.D., Gale J.D., Catlow C.R.A. (1999). The prediction of inorganic crystal structures using a genetic algorithm and energy minimization. *Phys. Chem. Chem. Phys.* **1**, 2535-2542.
140. Woodley S.M. (2004). Prediction of crystal structures using evolutionary algorithms and related techniques. *Structure and Bonding* **110**, 95-132.
141. Deaven D.M., Ho K.M. (1995). Molecular geometry optimization with a genetic algorithm. *Phys. Rev. Lett.* **75**, 288-291.
142. Michalewicz Z., Fogel D.B. (2004) *How to Solve It: Modern Heuristics*. Berlin, Springer.
143. Laio A., Parrinello M. (2002). Escaping free-energy minima. *Proc. Natl. Acad. Sci.* **99**, 12562-12566.
144. Oganov A.R., Martoňák R., Laio A., Raíteri P., Parrinello M. (2005). Anisotropy of Earth's D'' layer and stacking faults in the MgSiO₃ post-perovskite phase. *Nature* **438**, 1142-1144.
145. Legrand B. (1984). Relations entre la structure électronique et la facilité de glissement dans les métaux hexagonaux compacts. *Philos. Mag.* **49**, 171-184.
146. Panning, M., Romanowicz, B. (2004). Inferences on flow at the base of Earth's mantle based on seismic anisotropy. *Science* **303**, 351-353.
147. Garnero E.J., Maupin V., Lay T., Fouch M.J. (2004). Variable azimuthal anisotropy in Earth's lowermost mantle. *Science* **306**, 259-261.
148. Wookey J., Kendall J.-M., Rümpker G. (2005). Lowermost mantle anisotropy beneath the north Pacific from differential S-ScS splitting. *Geophys. J. Int.* **161**, 829-838.
149. Merkel S., Kubo A., Miyagi L., Speziale S., Duffy T.S., Mao H.K., Wenk H.R. (2006). Plastic deformation of MgGeO₃ post-perovskite at lower mantle pressures. *Science* **311**, 644-646.
150. Martoňák R., Oganov A.R., Glass C.W. (2007). Crystal structure prediction and simulations of structural transformations: metadynamics and evolutionary algorithms. *Phase Transitions*, in press.
151. Jóhannesson G.H., Bligaard T., Ruban A.V., Skriver H.L., Jacobsen K.W., and Nørskov J.K. (2002). Combined Electronic Structure and Evolutionary Search Approach to Materials Design. *Phys. Rev. Lett.* **88**, art. 255506.
152. Holzapfel W.B. (1996). Physics of solids under strong compression. *Rep. Prog. Phys.* **59**, 29-90.
153. Hemley R.J., Dera P. (2000). Molecular crystals. In: *Reviews in Mineralogy and Geochemistry* **41** "High-Temperature and High-Pressure Crystal Chemistry" (Eds. R.M. Hazen, R.T. Downs), pp. 335-419.
154. Tse J.S. (2005). Crystallography of selected high pressure elemental solids. *Z. Krist.* **220**, 521-530.
155. Bushman A.V., Fortov V.E. (1983). Models of equation of the matter state. *Uspekhi Fiz. Nauk* **140**, 177-232.
156. Degtyareva V.F. (2006). Simple metals at high pressures: the Fermi sphere-Brillouin zone interaction model. *Physics-Uspekhi* **49**, 369-388.
157. Grochala W., Hoffmann R., Feng J., Ashcroft N.W. (2007). The chemical imagination at work in very tight places. *Angew. Chem. Int. Ed.*, in press.
158. McMahan A.K. (1984). Alkali-metal structures above the s-d transition. *Phys. Rev.* **B29**, 5982-5985.

159. Goncharov A.F., Gregoryanz E., Hemley R.J., Mao H.K. (2001). Spectroscopic studies of the vibrational and electronic properties of solid hydrogen to 285 GPa. *Proc. Natl. Acad. Sci.* **98**, 14234-14237.
160. Babaev E., Sudbo A., Ashcroft N.W. (2004). A superconductor to superfluid phase transition in liquid metallic hydrogen. *Nature* **431**, 666-668.
161. Bonev S.A., Schwegler E., Ogitsu T., Galli G. (2004). A quantum fluid of metallic hydrogen suggested by first-principles calculations. *Nature* **431**, 669-672.
162. Mishima O., Calvert L.D., & Whalley E. (1984). Melting of ice I at 77 K and 10 kbar: a new method for making amorphous solids. *Nature* **310**, 393-394.
163. Richet P. & Gillet P. (1997). Pressure-induced amorphisation of minerals: a review. *Eur. J. Miner.* **9**, 907-933.
164. Sharma S.M. & Sikka S.K. (1996). Pressure-induced amorphization of materials. *Progr. Materials Sci.* **40**, 1-77.
165. Binggeli N., Keskar N.R., & Chelikowsky J.R. (1994b). Pressure-induced amorphisation, elastic instability, and soft modes in α -quartz. *Phys. Rev.* **B49**, 3075-3081.
166. Keskar N.R., Chelikowsky J.R., & Wentzcovitch R.M. (1994). Mechanical instabilities in AlPO₄. *Phys. Rev.* **B50**, 9072-9078.
167. Hemmati M., Czizmeshya A., Wolf G.H., Poole P.H., Shao J., & Angell C.A. (1995). Crystalline-amorphous transition in silicate perovskites. *Phys. Rev.* **B51**, 14841-14848.
168. Oganov A.R., Price G.D., Brodholt J.P. (2001). Theoretical investigation of metastable Al₂SiO₅ polymorphs. *Acta Crystallogr.* **A57**, 548-557.
169. Schmider H.L., Becke A.D. (2000). Chemical content of the kinetic energy density. *J. Mol. Struct. – Theochem* **527**, 51-61.
170. Schwarz U., Grzechnik A., Syassen K., Loa I., Hanfland M. (1999). Rubidium-IV: A high pressure phase with complex crystal structure. *Phys. Rev. Lett.* **83**, 4085-4088.
171. Brown I.D. (1992). Chemical and steric constraints in inorganic solids. *Acta Cryst.* **B48**, 553-572.
172. Kuwayama Y., Hirose K., Sata N., Ohishi Y. (2005). The pyrite-type high-pressure form of silica. *Science* **309**, 923-925.
173. Hama J. (1984). Anomalously high metallisation pressure of solid neon. *Phys. Lett.* **A105**, 303-306.
174. Boettger J.C. (1986). Equation of state and metallisation of neon. *Phys. Rev.* **B33**, 6788-6791.
175. Goncharenko I.N. (2005). Evidence for a magnetic collapse in the epsilon phase of solid oxygen. *Phys. Rev. Lett.* **94**, art. 205701.
176. Lundgaard L.F., Weck G., McMahon M.I., Desgreniers S., Loubeyre P. (2006). Observation of an O₈ molecular lattice in the epsilon phase of solid oxygen. *Nature* **443**, 201-204.
177. Fujihisa H., Akahama Y., Kawamura H., Ohishi Y., Shimomura O., Yamawaki H., Sakashita M., Gotoh Y., Takeya S., Honda K. (2006). O₈ cluster structure of the epsilon phase of solid oxygen. *Phys. Rev. Lett.* **97**, art. 085503.
178. Akahama Y., Kawamura H., Hausermann D., Hanfland M., Shimomura O. (1995). New high-pressure structural transition of oxygen at 96 GPa associated with metallization in a molecular solid. *Phys. Rev. Lett.* **74**, 4690-4693.

179. Shimizu K., Suhara K., Ikumo M., Eremets M.I., Amaya K. (1998). Superconductivity in oxygen. *Nature* **393**, 767-769.
180. Becke A.D., Edgecombe K.E. (1990). A simple measure of electron localization in atomic and molecular systems. *J. Chem. Phys.* **92**, 5397-5403.
181. Olijnyk H., Holzapfel W.B. (1984). Phase transitions in alkaline earth metals under pressure. *Physics Lett.* **A100**, 191-194.
182. Yabuuchi T., Nakamoto Y., Shimizu K., Kikegawa T. (2005). New high-pressure phase of calcium. *J. Phys. Soc. Japan* **74**, 2391-2392.
183. Yabuuchi T., Matsuoka T., Nakamoto Y., Shimizu K. (2006). Superconductivity of Ca exceeding 25 K at megabar pressures. *J. Phys. Soc. Japan* **75**, art. 083703.
184. Bader R.F.W. (1990). *Atoms in Molecules. A Quantum Theory*. Oxford University Press: Oxford.
185. Wells A.F. (1986). *Structural Inorganic Chemistry*. Clarendon Press: Oxford.
186. Edwards B., Ashcroft N.W. (1997). Spontaneous polarization in dense hydrogen. *Nature* **388**, 652-655.
187. Fiquet G. (2001). Mineral phases of the Earth's mantle. *Z. Krist.* **216**, 248-271.
188. Le Stunff Y., Wicks C.W. Jr., Romanowicz B. (1995). P'P' precursors under Africa: evidence for mid-mantle reflectors. *Science* **270**, 74-77.
189. Vinnik L., Niu F., Kawakatsu H. (1998). Broadband converted phases from midmantle discontinuities. *Earth Planets Space* **50**, 987-997.
190. Shim S.H., Duffy T.S., Shen G.Y. (2001). Stability and structure of MgSiO₃ perovskite to 2300-kilometer depth in Earth's mantle. *Science* **293**, 2437-2440.
191. Weir S.T., Mitchell A.C., Nellis W.J. (1996). Electrical resistivity of single-crystal Al₂O₃ shock-compressed in the pressure range 91-220 GPa (0.91-2.20 Mbar). *J. Appl. Phys.* **80**, 1522-1525.
192. Ono S., Oganov A.R., Koyama T., Shimizu H. (2006). Stability and compressibility of high-pressure phase of Al₂O₃ up to 200 GPa: implications for electrical conductivity at the base of the lower mantle. *Earth Planet. Sci. Lett.* **246**, 326-335.
193. Umemoto K., Wentzcovitch R.M., Allen P.B. (2006). Dissociation of MgSiO₃ in the cores of gas giants and terrestrial exoplanets. *Science* **311**, 983-986.
194. Frost D.J., Liebske C., Langenhorst F., McCammon C.A., Tronnes R.G., Rubie D.C. (2004). Experimental evidence for the existence of iron-rich metal in the Earth's lower mantle. *Nature* **428**, 409-412.
195. Sinmyo R., Hirose K., O'Neil HS, Okunishi E. (2006). Ferric iron in Al-bearing post-perovskite. *Geophys. Res. Lett.* **33**, art. L12S13.
196. Zhang F., Oganov A.R. (2006). Valence and spin states of iron impurities in mantle-forming silicates. *Earth Planet. Sci. Lett.* **249**, 436-443.
197. Ahmed-Zaid I. & Madon M. (1991). A high-pressure form of Al₂SiO₅ as a possible host of aluminium in the lower mantle. *Nature* **353**, 426-428.
198. Shcheka S.S., Wiedenbeck M., Frost D.J., Keppler H. (2006). Carbon solubility in mantle minerals. *Earth Planet. Sci. Lett.* **245**, 730-742.
199. Ono S., Kikegawa T., Ohishi Y., Tsuchiya J. (2005). Post-aragonite phase transformation in CaCO₃ at 40 GPa. *Am. Mineral.* **90**, 667-671.

200. Isshiki M., Irifune T., Hirose K., Ono S., Ohishi Y., Watanuki T., Nishibori E., Takadda M., and Sakata M. (2004). Stability of Magnesite and its high-pressure form in the lowermost mantle. *Nature* **427**, 60-63.
201. Skorodumova N.V., Belonoshko A.B., Huang L., Ahuja R., Johansson B. (2005) Stability of the MgCO₃ structures under lower mantle conditions. *Am. Mineral.* **90**, 1008-1011.
202. Knittle E. & Jeanloz R. (1991). Earth's core-mantle boundary: results of experiments at high pressures and temperatures. *Science* **251**, 1438-1443.
203. Woodhouse J.H., Giardini D., Li X.D. (1986). Evidence for inner core anisotropy from free oscillations. *Geophys. Res. Lett.* **13**, 1549-1552.
204. Ishii M., Dziewonski A.M. (2002). The innermost inner core of the earth: Evidence for a change in anisotropic behavior at the radius of about 300 km. *Proc. Natl. Acad. USA* **99**, 14026-14030.
205. Beghein C., Trampert J. (2003). Robust normal mode constraints on inner-core anisotropy from model space search. *Science* **299**, 552-555.

APPENDIX I.

Curriculum Vitae of Artem R. Oganov.

1) Senior Research Scientist and Lecturer, Group Leader, Laboratory of Crystallography, Department of Materials, ETH Zurich, Wolfgang-Pauli-Strasse 10, CH-8093 Zurich, Switzerland.

Tel.: +41-(0)44-632-3752; Fax: +41-(0)44-632-1133. Web-page: <http://olivine.ethz.ch/~artem>

2) Adjunct Professor, Geology Department, Moscow State University, Moscow 119992, Russia.

EDUCATION

- **2002:** PhD in Crystallography, University College London. Thesis 'Computer Simulation Studies of Minerals'.
- **1997:** MSc in Crystallography (Moscow State University) with top honours.

RESEARCH INTERESTS

- High-pressure chemistry and physics: studies of planetary materials, chemical bonding and structural transformations at high pressures and temperatures.
- Crystal structure prediction and computational materials design.
- Development and application of *ab initio* simulation methods: crystal structure prediction, thermodynamics and phase diagrams.

RESEARCH OUTPUT

117 publications (50 papers and book chapters, 65 abstracts, and 2 scientific highlights), including top-impact journals (Nature, PNAS, Nature Materials, PRL). 11 keynote/plenary, 55 invited, 11 contributed talks.

POSITIONS HELD

- **2006-now :** Adjunct Professor, Moscow State University
- **2003-now :** Senior Research Scientist and Lecturer, ETH Zurich. Group leader.
- **2006-2007:** Invited Professor, University of Marne-la-Vallée (France).
- **2005:** Invited Professor, University of Milan (Italy).
- **2002-2003:** Post-Doctoral Research Fellow, University College London
- **1999-2002:** British Government PhD scholar (by competition), University College London
- **1998-1999:** Russian President's Research Scholar (by competition), University College London
- **1993-1995:** External scientific collaborator, Russian Chemical Abstracts (VINITI)

HONOURS AND AWARDS

- **2006:** University Latsis Prize (25'000 CHF).
- **2005:** Offered Assistant Professorship at Princeton University (USA), declined.
- **2004:** European High-Pressure Research Group Award
- **2003:** Young Scientist Award of the European Union of Geosciences
- **2002:** President's Award of the Geological Society of London
- Scholarships:
 - **1999-2002:** British Government Scholarship
 - **1999-2002:** University College London Graduate School Scholarship
 - **1998-1999:** Russian President Scholarship
 - **1993-1999:** 5 consecutive Soros Foundation scholarships. Also – Lomonosov, Vinogradov and twice Shubnikov scholar.

TEACHING

- **2004-now:** lecturer, 2nd year undergraduate course “Mineralogical Crystallography”, ETH Zurich (Winter Semester, 2 hours/week lectures, 1 hour/week seminars).
- **2006-now:** lecturer, 4th year short undergraduate course “High-pressure structural chemistry”, Moscow State University (10 hours within 1 week).
- **2005:** lecturer, special graduate course “High-pressure mineral physics”, University of Milano (10 hours within 1 week).
- Lecturer at Summer Schools in Budapest (2002), Gargnano (2003), Erice (2003), Heidelberg (2005), Nancy (2005) - organized by the International Union of Crystallography and European Mineralogical Union.

Postdoc supervision: Y.-M. Ma (2006-2008), C. Attaccalite (2007-2009).

Current PhD students: D.J. Adams (2004-2007), D.Y. Jung (2004-2007), F. Zhang (2005-2008), C.W. Glass (2006-2009), H. Orsini-Rosenberg (2007-2010).

Former PhD student: K. Hassdenteufel (2003-2006).

Former diploma students: C.W. Glass (2005-2006), D.Y. Jung (2003-2004), A.V. Gutina (1997-1998).

PhD examiner: D. Sihachakr (2005, University of Paris XI, France), S. Greux (2006, University of Marne-la-Vallée, France).

GRANTS (total 1'254'782 CHF)

Applicants	Project title	Source	Amount	Duration
A.R. Oganov	“Crystal Structure Prediction at the Quantum Monte Carlo Level”	Swiss National Science Foundation	141'119	2007-2009
A.R. Oganov	“Computing Facilities for Evolutionary Crystal Structure Prediction”	ETH Zurich Research Commission	200'000	2006-2011
A.R. Oganov	“Development and Application of Evolutionary Algorithms for Crystal Structure Prediction”	Swiss National Science Foundation	309'355	2006-2009
W. Steurer, A.R.Oganov	“Design of Pentagonal and Heptagonal Boron-based Quasicrystals”	ETH Zurich Research Commission	153'000	2006-2009
F.Deschamps, P.J. Tackley, A.R. Oganov	“The Role of Post-perovskite Phase Transition in the Mantle Dynamics”	Swiss National Science Foundation	139'172	2006-2009
A.R. Oganov, W. Steurer	“Mineral Physics of Earth’s D” layer”	ETH Zurich Research Commission	138'000	2005-2008
A.R. Oganov, W. Steurer	“High-Pressure Physics of Mantle-Forming Minerals”	ETH Zurich Research Commission	143'336	2004-2007
A.R.Oganov, M.C.Warren, B.Winkler	Workshop “First-Principles Simulations: Perspectives and Challenges in Mineral Sciences”	Psi-k, CECAM, DGK	31'000	2004

SELECTED ACTIVITIES

2006

- Executive Committee member, User Group of Swiss National Supercomputing Centre.
- Chairman, symposium “Computational Mineral Physics” (American Geophysical Union (AGU) 2006 Fall Meeting, San Francisco, USA).

2005

- 2005-2008: elected vice-chairman of the Special Interest Group “Mineralogical Crystallography” of the European Crystallographic Association.
- Chairman, symposium “Crystallography at conditions of Earth and planetary interiors” (XX International Union of Crystallography (IUCr) meeting, Florence, Italy).
- Chairman, session "Theory of minerals at extreme conditions: state of the art" (3rd Studies of Matter at Extreme Conditions (SMEC) meeting, Florida, USA)

2004

- Organiser of the CECAM/Psi-k workshop “First-Principles Simulations: Perspectives and Challenges in Mineral Sciences” (Lyon, France)
- Chairman of the symposium “Crystallography of Planetary Interiors”, European Crystallographic Meeting (ECM-22, Budapest, Hungary)

2000

- Chairman of the symposium “Theoretical Studies of Mineral Structures and Properties”, European Crystallographic Meeting (ECM-19, Nancy, France)

1999

- Chairman of the symposium “Crystal Chemistry of Minerals”, European Union of Geosciences meeting (EUG-10, Strasbourg, France).

EDITORIAL ACTIVITIES AND REFEREEING

- Associate Editor: American Mineralogist.
- Guest Editor: Zeitschrift für Kristallographie (special issue “Computational Crystallography”, May/June 2005).
- Book Editor: “First-principles simulations: perspectives and challenges in mineral sciences” [German Crystallographic Society, 2004].
- Book referee for Oxford University Press
- Referee for 23 journals (including *Nature*, *Science*; *Physical Review Letters*; *Reports on Progress in Physics*; *Journal of Chemical Physics*; *Physical Review B*; *Applied Physics Letters*; *High-Pressure Research*; *Inorganic Chemistry*).
- External expert for the German Research Foundation (DFG).

MEMBERSHIP OF SCIENTIFIC SOCIETIES

- ETH Zurich representative, COMPRES (Consortium for Materials Properties Research in Earth Sciences).
- Member, Swiss Crystallographic Society and International Union of Crystallography.
- Founding member, Mineralogical Crystallography Group of the European Crystallographic Association.

PATENT APPLICATION

Glass C.W., Oganov A.R. (2005-2006). “Method for crystal structure determination”. International patent application PCT/CH06/000720 (22 December 2005).

POPULAR MEDIA

- *Physics Today* (September 2006), *Physics News Update* (7 July 2006), *La Recherche* (January 2005).
- 3 Articles in *ETH Life* (August 2004; July 2005; December 2005).
- *Spektrum der Wissenschaft* (January 2007), *Neue Zürcher Zeitung* (05.07.2006), *Tages Anzeiger* (22.07.2004), *20 Minuten Zürich* (23.12.2005), *St. Galler Tagblatt* (24.12.2005), *Der Zürcher Oberländer* (27.12.2005), *Der Landbote* (2 articles on 28.12.2005), *Zürcher Unterländer* (06.01.2006), *Schweizer Machinenmark* (24.01.2006), *Computerworld* (27.01.2006), *Kommersant* (07.02.2007, in Russian).
- SWR Radio Interviews (24 July 2004; 14 January 2006), Deutschland Radio Interview (27 January 2006).
- My research findings were discussed in over 100 web-sources, in English, German, Italian, French, Spanish, Portuguese, Russian, Ukrainian, Korean, Hebrew and Hungarian languages (see <http://olivine.ethz.ch/~artem/Highlights.html>).

SELECTED INVITED TALKS (past 3 years; *- invited, ** - plenary)
--

- *21. "Matter at Extreme Conditions: Exploring New Chemistry and Interiors of Planets". (ETH Latsis Prize Lecture, Geneva, Switzerland, 8.11.2006).
- **20. "Matter at Extreme Conditions: New Simulation Methodologies and Results" (Italian Crystallographic Association meeting, Ferrara, Italy, 19.09.2006).
- **19. "Crystal Structure Prediction: from Materials Design to Mineralogy of Planets" (Italian Crystallographic Association meeting, Ferrara, Italy, 19.09.2006).
- **18. "Predicting New High-Pressure Crystal Structures with an *Ab Initio* Evolutionary Algorithm" (EHPRG-2005 meeting, Prague, 4.09.2006).
- *17. "Prediction of Unknown Crystal Structures with Evolutionary Algorithms" (ECM-23 meeting, Leuven, Belgium, 6-11.08.2006,).
- *16. "Crystal Structure Prediction: New Methodology and Geologically Important Results" (19th General Meeting of the International Mineralogical Association, Kobe, Japan, 23-28.07.2006)
- *15. "Crystal Structure Prediction with *Ab Initio* Evolutionary Algorithms" (Electronic Structure 2006 conference, Columbus, Ohio, 25.06.2006).
- *14. "USPEX – an Evolutionary Algorithm for Crystal Structure Prediction" (IDC HPC Conference, Zurich, 1-2.06.2006)
- *13. "Mineralogy of the Earth's deep Interior: Latest Crystallographic Discoveries and New Geophysical Models" (Geology Department, Moscow State University, Russia, 16.03.2006).
- **12. "Recent Developments in Computational Mineral Physics" (William Smith Meeting - The Deep Earth: The Structure and Evolution of the Interior of our Planet, London, 23-24.11.2005).
- *11. "Theory of Materials at Extreme Conditions: Predicting New Phases, their Stability Fields, and Reactions" (International Workshop on the Post-perovskite Phase Transition in the Earth's Deep Mantle, Tokyo, Japan, 3-4.10.2005).
- *10. "Post-perovskite Phase of MgSiO₃: the Discovery, its Geophysical Implications and Current State of Knowledge" (2005 Psi-k conference, Schwaebisch Gmuend, Germany, 20.09.2005).
- **9. "Rediscovering Nature with Supercomputers: from Microscopic Scale to Planetary Structures" (CRAY XT3 Inauguration Keynote Lecture, CSCS, Manno, Switzerland, 15.09.2005).
- *8. "Novel High-Pressure Phases of Earth's Mantle Minerals" (IUCr-2005 congress, Florence, 26.08.2005).
- **7. "New High-Pressure Phase of Al₂O₃ and Implications for Earth's D" Layer" (joint AIRAPT-EHPRG conference, Karlsruhe, Germany, 27.06.2005).
- **6. "High-Pressure Mineralogy" (joint AIRAPT-EHPRG conference, Karlsruhe, Germany, 27.06.2005).
- *5. "Ab Initio Phase Diagrams of Minerals" (3rd meeting on Study of Matter at Extreme Conditions, Miami Beach, USA, 17-22.04.2005).
- *4. "Theoretical and Experimental Evidence for a Post-perovskite Phase of MgSiO₃ in Earth's D" Layer" (APS March meeting, Los Angeles, USA, 21.03.2005).
- *3. "Ab Initio Phase Diagrams of Minerals" (CECAM/Psi-k workshop "First-Principles Simulations: Perspectives and Challenges in Mineral Sciences", Lyon, 28.09.2004).
- **2. "High-Pressure Mineralogy, or Looking Inside Planets" (Award Lecture, EHPRG-42 meeting, Lausanne, 2.09.2004).
- *1. 'Phase Diagrams of Minerals from Density-Functional Perturbation Theory' (ECM-22 meeting, Budapest, Hungary, 29.08.2004)

APPENDIX II.

List of patents and publications of Artem R. Oganov.

PATENT APPLICATION:

Glass C.W., Oganov A.R. (2005-2006). "Method for crystal structure determination". International patent application PCT/CH06/000720 (22 December 2005).

CHAPTERS IN BOOKS:

6. Oganov A.R. (2007). Thermodynamics, phase transitions, equations of state and elasticity of minerals at high pressures and temperatures. *Treatise in Geophysics*, vol. 2 (Mineral Physics, edited by G.D. Price), *in press*.
5. Jung D.Y., Oganov A.R. (2005). Basics of first-principles simulation of matter under extreme conditions. *EMU Notes in Mineralogy* v.7 ("High-Pressure Behaviour of Minerals", edited by R. Miletich), 117-138.
4. Adams D.J., Oganov A.R. (2005). Theory of minerals at extreme conditions: predictability of structures and properties. *EMU Notes in Mineralogy* v.7 ("High-Pressure Behaviour of Minerals", edited by R. Miletich), 441-457.
3. Oganov A.R. (2004). Phase diagrams of minerals from first principles. *Proceedings of the CECAM Workshop «First-Principles Simulations: Perspectives and Challenges in Mineral Sciences»* (Berichte aus Arbeitskreisen der DGK, Nr. 14, German Crystallographic Society), pp. 53-62.
2. Oganov A.R. (2003). Theory of Minerals at High and Ultrahigh Pressures: Structure, Properties, Dynamics, and Phase Transitions. In: *High-Pressure Crystallography*, NATO Science Series: II: Mathematics, Physics and Chemistry, vol. 140, p.199-215 (edited by A.Katrusiak, P.F.McMillan). Kluwer Academic Publishers, Dordrecht.
1. Oganov A.R., Brodholt J.P., Price G.D. (2002). Ab initio theory of thermoelasticity and phase transitions in minerals. *EMU Notes in Mineralogy* v.4 ('Energy Modelling in Minerals', edited by C.M. Gramaccioli), pp.83-170.

PAPERS IN REFEREED JOURNALS:

44. Oganov A.R., Glass C.W., Ma Y.-Z., Ma Y.-M., Chen J. (2007). Ionic high-pressure form of elemental boron. *Nature*, submitted.
43. Martoňák R., Donadio D., Oganov A.R., Parrinello M. (2007). 4- to 6- coordinated silica: transformation pathways from metadynamics. *Phys. Rev. B.*, under review.
42. Ma Y.-M., Oganov A.R., Glass C.W. (2007). Structure of metallic ζ -phase of oxygen and isosymmetric nature of ϵ - ζ transition. *Phys. Rev. Lett.*, submitted.

41. Hassdenteufel K.H., Oganov A.R., Steurer W., Katrich S. (2007). *Ab initio* study of the W-phase of Al-Co-Ni, an approximant of the decagonal Al-Co-Ni quasicrystal. *Phys. Rev. B.*, submitted.
40. Martoňák R., Oganov A.R., Glass C.W. (2007). Crystal structure prediction and simulations of structural transformations: metadynamics and evolutionary algorithms. *Phase Transitions*, in press.
39. Xie Y., Tse J.S., Cui T., Oganov A.R., He Z., Ma Y., Zou G. (2007). Electronic and phonon instabilities in face-centered cubic alkali metals under pressure. *Phys. Rev. B***75**, art. 064102.
38. Dorogokupets P.I., Oganov A.R. (2007). Ruby, metals, and MgO as alternative pressure scales: A semiempirical description of shock-wave, ultrasonic, x-ray, and thermochemical data at high temperatures and pressures. *Phys. Rev. B***75**, art. 024115.
37. Glass C.W., Oganov A.R., Hansen N. (2006). USPEX – evolutionary crystal structure prediction. *Comp. Phys. Comm.* **175**, 713-720.
36. Zhang F., Oganov A.R. (2006). Valence and spin states of iron impurities in mantle-forming silicates. *Earth Planet. Sci. Lett.* **249**, 436-443.
35. Pushcharovsky D.Yu., Oganov A.R. (2006). Structural transformations of minerals in deep geospheres: a review. *Crystallography Reports* **51**, 767-777.
34. Dorogokupets P.I., Oganov A.R. (2006). Equations of state of Al, Au, Cu, Pt, Ta and W and the revised ruby pressure scale. *Doklady Earth Sciences* **410**, 1091-1095.
33. Martoňák R., Donadio D., Oganov A.R., Parrinello M. (2006). Crystal structure transformations in SiO₂ from classical and *ab initio* metadynamics. *Nature Materials* **5**, 623-626.
32. Oganov A.R., Glass C.W. (2006). Crystal structure prediction using evolutionary techniques: principles and applications. *J. Chem. Phys.* **124**, art. 244704.
31. Zhang F., Oganov A.R. (2006). Mechanisms of Al³⁺ incorporation in MgSiO₃ post-perovskite at high pressures. *Earth Planet. Sci. Lett.* **248**, 54-61.
30. Ono S., Oganov A.R., Koyama T., Shimizu H. (2006). Stability and compressibility of high-pressure phase of Al₂O₃ up to 200 GPa: implications for electrical conductivity at the base of the lower mantle. *Earth Planet. Sci. Lett.* **246**, 326-335.
29. Adams D.J., Oganov A.R. (2006). *Ab initio* molecular dynamics study of CaSiO₃ perovskite at *P-T* conditions of Earth's lower mantle. *Phys. Rev. B***73**, 184106.
28. Boldyreva E.V., Ahsbahs H., Chernyshev V.V., Ivashevskaya S.N., Oganov A.R. (2006). Effect of hydrostatic pressure on the crystal structure of sodium oxalate: X-ray diffraction study and *ab initio* simulations. *Z. Krist.* **221**, 186-197.
27. Ghose S., Krisch M., Oganov A.R., Beraud A., Bossak A., Gulve R., Seelaboyina R., Yang H., Saxena S.K. (2006). Lattice dynamics of MgO at high pressure: theory and experiment. *Phys. Rev. Lett.* **96**, art. 035507.

26. Oganov A.R., Glass C.W., Ono S. (2006). High-pressure phases of CaCO₃: crystal structure prediction and experiment. *Earth Planet. Sci. Lett.* **241**, 95-103.
25. Oganov A.R., Martoňák R., Laio A., Raiteri P., Parrinello M. (2005). Anisotropy of Earth's D" layer and stacking faults in the MgSiO₃ post-perovskite phase. *Nature* **438**, 1142-1144.
24. Oganov A.R., S. Ono (2005). The high-pressure phase of alumina and implications for Earth's D" layer. *Proc. Natl. Acad. Sci.* **102**, 10828-10831.
23. Ono S., Oganov A.R. (2005). *In situ* observations of phase transition between perovskite and CaIrO₃-type phase in MgSiO₃ and pyrolytic mantle composition. *Earth Planet. Sci. Lett.* **236**, 914-932.
22. Jung D.Y., Oganov A.R. (2005). *Ab initio* study of the high-pressure behaviour of CaSiO₃ perovskite. *Phys. Chem. Minerals* **32**, 146-153.
21. Oganov A.R., Price G.D., Scandolo S. (2005). *Ab initio* theory of planetary materials. *Z. Krist.* **220**, 531-548.
20. Oganov A.R., Price G.D. (2005). *Ab initio* thermodynamics of MgSiO₃ perovskite at high pressures and temperatures. *J. Chem. Phys* **122**, art. 124501.
19. Alfredsson M., Dobson D.P., Oganov A.R., Catlow C.R.A., Brodholt J.P., Parker S.C., Price G.D. (2005). Crystal morphology and surface structures of the orthorhombic MgSiO₃ perovskite. *Phys. Chem. Minerals* **31**, 671-682.
18. Oganov A.R., Gillan M.J., Price G.D. (2005). Structural stability of silica at high pressures and temperatures. *Phys. Rev.* **B71**, art. 064104.
17. Oganov A.R., Ono S. (2004). Theoretical and experimental evidence for a post-perovskite phase of MgSiO₃ in Earth's D" layer. *Nature* **430**, 445-448.
16. Oganov A.R. & Dorogokupets P.I. (2004). Intrinsic anharmonicity in thermodynamics and equations of state of solids. *J. Phys.: Cond. Matter.* **16**, 1351-1360.
15. Dorogokupets P.I. & Oganov A.R. (2004). Intrinsic anharmonicity in equations of state of solids and minerals. *Doklady Earth Sciences* **395**, 238-241.
14. Senyshyn A., Oganov A.R., Vasylechko L., Ehrenberg H., Bismayer U., Berkowski M., Matkovskii A. (2004). Crystal structure and thermal expansion of the perovskite – type Nd_{0.75}Sm_{0.25}GaO₃ – powder diffraction and lattice dynamical studies. *J. Phys.: Cond. Matter* **16**, 253-265.
13. Dorogokupets P.I. & Oganov A.R. (2003). Equations of state of Cu and Ag and the revised ruby pressure scale. *Doklady Earth Sciences* **391A**, 854-857.
12. Oganov A.R. & Dorogokupets P.I. (2003). All-electron and pseudopotential study of MgO: Equation of state, anharmonicity, and stability. *Phys. Rev.* **B67**, art. 224110.
11. Oganov A.R., Gillan M.J., Price G.D. (2003). Ab initio lattice dynamics and structural stability of MgO. *J. Chem. Phys.* **118**, 10174-10182.

10. Brodholt J.P., Oganov A.R., Price G.D. (2002). Computational mineral physics and physical properties of perovskite. *Phil. Trans. Royal Soc. London A***360**, 2507-2520.
9. Oganov A.R., Price G.D., Brodholt J.P. (2001). Theoretical investigation of metastable Al_2SiO_5 polymorphs. *Acta Crystallogr. A***57**, 548-557.
8. Oganov A.R., Brodholt J.P., Price G.D. (2001). The elastic constants of MgSiO_3 perovskite at pressures and temperatures of the Earth's mantle. *Nature* **411**, 934-937.
7. Oganov A.R., Brodholt J.P., Price G.D. (2001). *Ab initio* elasticity and thermal equation of state of MgSiO_3 perovskite. *Earth and Planetary Science Letters* **184**, 555-560.
6. Oganov A.R., Organova N.I., Urusov V.S. (2001). Nature of Al-Si anti-ordering in a two-phase feldspar from the Pektusan volcano. *Geochem. Int.* **39**, 1160-1171.
5. Oganov A.R., Brodholt J.P., Price G.D. (2000). Comparative study of quasiharmonic lattice dynamics, molecular dynamics and Debye model in application to MgSiO_3 perovskite. *Phys. Earth Planet. Int.* **122**, 277-288.
4. Oganov A.R., and Brodholt J.P. (2000). High-pressure phases in the Al_2SiO_5 system and the problem of Al-phase in Earth's lower mantle: *ab initio* calculations. *Phys. Chem. Minerals* **27**, 430-439.
3. Urusov V.S., Eremin N.N., Oganov A.R. (1999). Modeling of structures and properties of oxide crystals by minimization of the atomization energy. *Crystallography. Rep.* **44**, 356-365.
2. Urusov V.S., Oganov A.R., Eremin N.N. (1998). Computer simulation of structure, properties and stability of Al_2SiO_5 polymorphs. I. Ionic approximation. *Geochem. Int.* **36**, 397-414.
1. Oganov A.R. (1996). A finding of rhombohedral pyrite crystals. *Proc. Russ. Min. Soc.*, No.1, 65-69.